Mangrove Biomass from Space:

A South Australian case study using optical, RADAR and LiDAR datasets.

By

Bassam Waheed

Thesis
Submitted to Flinders University
for partial fulfilment of the degree of

Master of Geospatial Information Science

College of Science and Engineering
25 November 2025

Table of Contents

ii

ABSTRACT

Mapping and quantitative assessment of above ground biomass (AGB) of mangroves may be possible using multiple remote sensing datasets such as optical, RADAR and LiDAR supported by fieldwork. This study assessed South Australian (SA) mangroves (*Avicennia marina*) in the St Kilda area near Salisbury. Literature asserts that mangroves absorb four times more carbon than normal forest; thus estimation of AGB is important for planning and decision making in coastal zones. The main objective of this research was to assess the capacity of satellite data to study mangrove extent and AGB in St Kilda and to build a technical framework to integrate multiple remote sensing datasets. A specific research question was what are the optimum methods to study AGB using optical, RADAR and LiDAR? Additionally, does a data fusion approach assist quantise AGB? This comprehensive study of mangroves was undertaken using optical satellites (Pléiades Neo, and Sentinel-2) and RADAR (ALOS-1 PALSAR, ALOS-2 PALSAR, and Sentinel-1) and demonstrated that AGB estimation is possible by identifying correlation between remote sensing variables and biomass determined from field observations using statistical regression. Linear regression for $LiDAR_{CHM-mean}$ and mean heights from field work, showed a high correlation between these two variables with a R^2 value of 0.87. The average value for AGB estimation from field data was 59.7 tons h^{-1}. An optimum regression model from $LiDAR_{CHM}$, with a R^2 value of 0.74, yielded a total biomass of 96,149 tons. Regression models from optical satellite data, Pléiades Neo, provided the R^2 value of 0.48 using NDVI and 0.27 using principal component analysis (PC-2). In contrast, Sentinel-2 gave R^2 value of 0.40 using red-edge NDVI (NDVIre) and 0.48 using the mangrove vegetation index (MVI). The final AGB estimation from optical imagery yielded a value of 69,024 tons with an optimum model. In assessing mangrove extent, two classification approaches were used for Pléiades Neo; random tree (RT) and ISO cluster. RT, a variant of Random Forests, application resulted in the extent of mangroves (13.09 km^2 & 15.78 km^2) for pan-sharpened and multispectral respectively and similarly, ISO cluster computed (14.35 km^2 & 14.99 km^2) for both sets of imagery. The RT model achieved a user accuracy of 0.98 with Kappa value of 0.86 for Pléiades Neo, using a combination of six spectral bands, vegetation index (NDVI) and a CHM. Three RADAR datasets were used to calculate AGB estimation using backscatter coefficients, RADAR indices, GLCM matrix, PCA techniques and $field_{mean}$ biomass by applying statistical regression. The regression results showed R^2 values for $field_{mean}$ biomass against backscatter (HV=0.18, VH=0.14, VH=0.12), PCA (0.27, 0.09, 0.16), GLCM (0.23, 0.15, 0.17) and RVI (0.29, 0.09, 0.12) for ALOS-1 PALSAR, ALOS-2 PALSAR, and Sentinel-1 satellites respectively. Additionally, a pixel based fusion approach for ALOS-2 PALSAR and Sentinel-1 resulted in R^2 between PC-2 and $field_{mean}$ biomass values of 0.27 at 4m. The satellite remote sensing approach made this study non-intrusive, potentially repeatable and regular, and showed excellent capability to map mangrove extent, especially when multiple datasets were used.

DECLARATION

I certify that this thesis does not incorporate without acknowledgment any material previously submitted for a degree or diploma in any university; and that to the best of my knowledge and belief it does not contain any material previously published or written by another person except where due reference is made in the text.

Signed...

Date : 24 Oct 2025

ACKNOWLEDGEMENTS

LIST OF FIGURES

LIST OF TABLES

LIST OF EQUATIONS

LIST OF ACRONYMS

AGB	Above Ground Biomass
ANN	Artificial Neural Network
ARA	Airborne Research Australia
ASF	Alaska Satellite Facility
ASM	Angular Second Moment
C3	Covariance Matrix (3x3)
CEOS	Committee on Earth Observation Satellites
CF	Calibration Factor
CFI	Carbon Farming Initiative
CHM	Canopy Height Model
CMRI	Combined Mangrove Recognition Index
CS	Component Substitution
CSI	Canopy Structure Index
dB	Decibel
DBH	Diameter at Breast Height
DEM	Digital Elevation Model
DN	Digital Number
DSM	Digital Surface Model
DTM	Digital Terrain Model
DVI	Difference Vegetation Index
EM	Electromagnetic
ENVI	Environment for Visualizing Images
ESRI	Environmental Systems Research Institute
EVI	Enhanced Vegetation Index
FAO	Food and Agriculture Organization of the United Nations
GCP	Ground Control Point
GDM	Global Distribution of Mangroves
GEDI	Global Ecosystem Dynamics Investigation Lidar
GEMI	Global Environmental Management Initiative
GLCM	Gray-Level Co-Occurrence Matrix
GMW	Global Mangrove Watch
GPS	Global Positioning System
ha	Hectare
HPF	High-pass Filter
HSI	Hue Saturation Intensity
ICESat	Ice Cloud and Land Elevation Satellite
InSAR	Interferometric Synthetic Aperture Radar
IPCC	Intergovernmental Panel on Climate Change
ISODATA	Iterative Self-organizing Data Analysis Technique Algorithm
IUCN	International Union for Conservation of Nature
JAXA	Japan Aerospace Exploration Agency
km	Kilometer
KP	Kyoto Protocol
LAI	Leaf Area Index
LiDAR	Light Detection and Ranging
M	Meter
MAX	Maximum
MIN	Minimum

MRT	Multi-resolution Transformation
MVI	Mangrove Vegetation Index
NASA	National Aeronautics and Space Administration
NDMI	Normalized Difference Moisture Index
NDVI	Normalized Difference Vegetation Index
NDVIre	Red-Edge Normalized Difference Vegetation Index
NDWI	Normalized Difference Water Index
NDWI2	Normalized difference water index 2
NED	Near-infrared Red edge and Deep-blue
NISAR	NASA-ISRO Synthetic Aperture Radar
PALSAR	Phased Array type L-band Synthetic Aperture Radar
PCA	Principal Component Analysis
PolInSAR	Polarimetric Interferometric Synthetic Aperture Radar
RADAR	Radio Detection And Ranging
REDD	Reducing Emissions from Deforestation and Degradation
RF	Random Forest
RFDI	Radar Forest Degradation Index
RM-ALOS1	Regression Model ALOS-1
RM-ALOS2	Regression Model ALOS-2
RM-F1	Regression Model Fusion-1
RM-F2	Regression Model Fusion-2
RM-Field	Regression Model Field
RM-LiDAR	Regression Model LiDAR
RM-PLNeo	Regression Model Pléiades Neo
RM-S1	Regression Model Sentinel-1
RM-S2	Regression Model Sentinel-2
ROI	Area of Interest
RT	Random Trees
RVI	Radar Vegetation Index
SA	South Australia
SAR	Synthetic Aperture Radar
SAVI	Soil Adjusted Vegetation Index
SNAP	Sentinel Application Platform
SRTM	Shuttle Radar Topography Mission
SVM	Support Vector Machine
SWIR	Short-Wave Infrared
T3	Coherency Matrix (3 x3)
TanDEM-X	TerraSAR-X add-on for Digital Elevation Measurement
UFCCC	United Nations Framework Convention on Climate Change
USGS	United States Geological Survey
UTM	Universal Transverse Mercator
VI	Vegetation Indices
WAM	World Atlas of Mangroves
WCMC	World Conservation Monitoring Centre
WGS	World Geodetic System

CHAPTER ONE : INTRODUCTION

1.1 Background

Mangroves are a group of delicate plants, shrubs and trees, most likely to grow in a salty shallow water in intertidal zones (Duke 2006). They provide many ecological services and are rich in coastal biodiversity (Fatoyinbo *et al.* 2008). Mangrove forest cover is thought to be most productive ecosystem of the world (Bagot *et al.* 2024) and its carbon storing capacity is remarkably high which is four times greater than a normal forest (Huong *et al.* 2023; Hamdan *et al.* 2013; Suardana *et al.* 2022). Based on nomenclature, mangroves means *mangal* that originates from Greek. In Australia, most of the mangrove plants are along the tropical and sub-tropical regions in coastal zones and estuaries. There are many varieties of mangroves worldwide and some of the popular varieties are found in tropical regions of Australia. This study is focused on a South Australian region where only *Avicennia marina* is under consideration.

This research aims to provide above ground biomass (AGB) estimation using optical and RADAR satellites datasets supported by airborne LiDAR and field based allometric equations. A specific objective of this research is AGB estimation using significant remote sensing variables and to develop regression models with $field_{Biomass}$. Investigating AGB estimation is a continuing concern of researchers and ultimately, after exploring these remote sensing datasets, mangrove ecosystem conditions, biomass and carbon stocks can be monitored well. Recent evidence (Lucas *et al.* 2020) suggested that mangrove forest provides extensive range of commercial benefits to the community and ecological services. The commercial benefits of mangrove habitats include wood, fish, honey and tourism. In terms of ecological services, it provides carbon sequestration, natural habitats, micro-nutrient supply and coastal stabilisation (Hirata *et al.* 2014). In certain circumstances, mangroves prevent coastal erosion, decrease flood intensity and filter pollutants. In a comprehensive study of mangroves, Vaghela *et al.* (2021) reported that mangrove distribution depends upon various factors such as tidal variations, wind velocity, temperature, soil and the availability of nutrients.

A commonly held belief is that, mangrove forest ecosystems store high amount of carbon and abundant in nutrients availability (Hamdan *et al.* 2013) and thought to be custodian of seagrass and salt marsh. Moreover, it is a very prolific ecosystem which provides domain of ecological services as mentioned earlier. Despite being an important ecosystem, it is estimated that (Wong *et al.* 2020) global mangroves are decreasing between 0.16% and 0.39% per annum. Due to this fact, it is under serious global scale consideration by international bodies such as United States Geological Survey – USGS, Food and Agriculture Organization of the United Nations – FAO, International Union for Conservation of Nature – IUCN, Intergovernmental Panel on Climate Change – IPCC, and also being monitored under carbon agreements and protocols such as

Reducing Emissions from Deforestation and Degradation – REDD+, Kyoto protocol. For example, the UFCCC initiative (REDD+) promotes emission reduction from deforestation and forest degradation (Friess *et al.* 2019). The IUCN presented the first report on "The global status of mangrove ecosystem" and later World Mangrove Atlas was published in 1997 and some of the mangroves are also on red list of IUCN. Bunting *et al.* (2018) reported that, the first baseline for global mangrove maps was produced under Kyoto protocol in 2010 by Japan Aerospace Exploration Agency – JAXA. The main purpose of this protocol was to reduce green house gasses. Likewise, IPCC has also taken a few initiatives on carbon control as it links to forests. At regional level, particularly in Australia, CFI is a local carbon initiative for Australian farmers which gives carbon credit to the farmers to reduce carbon.

Quantitative assessment of AGB is very much important for planning and decision making of coastal zones. Zhu *et al.* (2020) explained that, AGB assessment is an important tool for blue carbon assessment and mangrove restoration and Pham *et al.* (2020a; 2020b) described that AGB estimation is desirable to monitor mangrove sustainability in terms of its preservation and protection. Moreover, extensive research from (Fatoyinbo & Simard 2013; Aseran *et al.* 2021) described that, the quantification of AGB is a significant element to study climate change and the carbon cycle. AGB is also a good indicator of deforestation and afforestation as well. It has been previously observed that AGB measurement also offer us a good quantitative assessment of carbon (Feliciano *et al.* 2017; Ghosh & Behera 2021). To estimate AGB, conventional methods are very much dependent on in-situ measurements and archived versions of inventory data.

In a research, Xu *et al.* (2022) reported that biomass measurements from conventional methods are destructive and limited to small-dimeter trees. Komiyama *et al.* (2008) demonstrated that; the allometric method is being used extensively and easy to use to calculate AGB. However, Chave *et al.* (2005) is cautious against field data collection in a complex environment because this might be challenging and very labour-intensive. However, in a recent times, AGB estimation using remote sensing approaches is found to be very useful and an alternative way to study. For example, in particular, airborne LiDAR is more effective to measure heights, which are normally obtained from field data. In some cases, RADAR approaches have been used along with InSAR, PolInSAR and tomography methods. In some studies, multispectral data is used along with SAR data in a fusion of data.

Sensors developed in a recent era are highly effective and able to identify, quantify and enumerate spatial signatures of mangrove forest. Moreover, Kamal *et al.* (2022), highlights that this technique is non-destructive as no plants are uprooted. There have been numerous remote sensing techniques that have been used to study mangroves but each of them has its own advantages. As this study is being carried out using multiple remote sensing datasets, which can open various doors to study mangroves. Lucas *et al.* (2020) did a similar to monitor structural characteristics of

mangroves. Likewise, this study also being conducted using multi-source satellites. At first, airborne LiDAR will be use to extract canopy heights to monitor vertical structure of mangroves. In this study LiDAR data was collected by ARA. Some researchers (Hu *et al.* 2020; Lagomasino *et al.* 2016) believed that LiDAR thought to be best tool to measure the canopy height, as this parameter is required to measure above ground biomass (AGB). Through LiDAR data, mangrove canopy height can easily be measured by subtracting DEM from DSM. The resultant layer is canopy height model (CHM) that is the height at each pixel. For passive remote sensing, two of the satellites Pléiades Neo and Sentinel-2 are included in this study. Fatoyinbo *et al.* (2013) reported that optical remote sensing is very good to study mangrove extent and estimation at global scale. However, researchers reported that, optical sensors ability to estimate AGB is very limited and assessment is not very reliable.

Furthermore, this research will also use active remote sensing approach, as this will allow us to study RADAR backscatter coefficients and analysis in more detail such RVI, PCA and GLCM. It is now very well established by many researchers (Lucas *et al.* 2006; Vaghela *et al.* 2021; Nandy *et al.* 2021; Santoro *et al.* 2020; Ningthoujam *et al.* 2017), that SAR backscatter has many advantages over optical imagery as it has many polarization levels such as dual (HH, HV) and quad (HH, HV, VV, VH). Moreover, it has additional properties to be studied such as dielectric constant, penetration levels and surface roughness in different microwave regions P, L, C, X & S bands. It has been noted that, for this type of study of mangrove C, L and P are thought to be ideal (Pham *et al.* 2019). As, L-band can penetrate more into canopy and can bring more information. Comparatively, C-band can only provide surface canopy information. For this study, ALOS-1 PALSAR, ALOS-2 PALSAR and Sentinel-1 are selected. The revisit capability of ALOS-2 PALSAR is 14 days and of Sentinel-1 is 6-12 days. Moreover, ALOS-1 PALSAR data is in archive mode and no longer available after 2011. But, ALOS-2 PALSAR and Sentinel-1 data is still currently available. Through RADAR, scattering and decomposition properties of the mangroves will also be taken into account. While using RADAR data, there might be some challenges such as calibration, speckle "noise" and geometrical issues and C-band has its' own limitations. To enhance the ability of optical and RADAR this research will also explore fusion approaches of the remote sensing data.

1.2 Problem Statement and Justification

Most of the mangrove forest maps are at a global scale such as Global Mangrove Watch (GMW), Global Distribution of Mangroves (GDM) and Global Forest Watch (GFW) and not very much consistent at regional scale. Based on that, some of the datasets used in these global maps are outdated now and need to be updated. Moreover, no previous study has addressed South Australian mangroves using multiple remote sensing datasets and not been processed well enough to provide reliable AGB estimation. Ultimately, AGB estimation can play a crucial role in

monitoring mangroves, which can lead to monitor carbon in mangrove ecosystems. Several attempts (Li *et al.* 2024; Oehmcke *et al.* 2024; Feliciano *et al.* 2017; Wang *et al.* 2023; Fatoyinbo *et al.* 2018; Zhou *et al.* 2023; Lagomasino *et al.* 2016; Akay *et al.* 2009; Li *et al.* 2014; Ovejero *et al.* 2023; Silva *et al.* 2018) have been made using airborne LiDAR and field based allometric equations to study AGB. In a previous studies of AGB, different variables have been found to be related to AGB from optical satellites such as Worldview 2, Sentinel-2 and Landsat-8. In contrast, RADAR based derivations of AGB are very limited for this area and not thoroughly investigated. In addition to that, SA mangroves are exposed to threat because of anthropogenic activities, extreme dry conditions and high salinity levels. Despite the importance of mangrove forest, they seem to be under threat and need to be monitored using better resolution. Besides providing mangrove AGB estimation, this research is also going to explore RADAR based decomposition analysis which might lead to better quantization and spatial distribution of mangroves potentially leading better planning and decision-making.

1.3 Research Aims and Objectives

The main aim of this research is to assess the capacity of satellite data to study mangrove aboveground biomass – AGB in South Australia. However, there are some specific research questions.

1. What are optimum methods to study AGB using LiDAR, optical and RADAR datasets?
2. How can optical and RADAR be combined to study mangroves using fusion approaches?
3. In what way does RADAR scattering and decomposition analysis assess the properties of mangroves?
4. How could field based methods compare with satellite-based techniques?

1.4 Project Scope and Significance

The main scope of this research to study mangroves using multiple remote sensing datasets such as LiDAR, optical and RADAR. The main benefits of using remote sensing based approach are; it is non-intrusive, repetitive and regular. Additionally, it is applicable everywhere and potentially cheaper as compared to the fieldwork. In contrast, field work is expensive, labour intensive and difficult to acquire in remote or inaccessible environments. Ultimately, this research will also be helpful to government departments and private entities who are directly and indirectly related to coastal planning and involved in carbon sequestration mapping. Currently, the St Kilda mangroves are in focus in this study and outcome of this study will develop the understanding of various remote sensing variables and field based estimations. Therefore, these techniques can also be applied to other areas of South Australia such as Eyrie Peninsula and all over the Australia where the species is the same.

1.5 Research Challenges

Due to tough environment along the coastal line, it is not easy to collect in-situ measurements such as tree diameter and height values of sample trees. On top of that, some of the challenges include marshy areas, cloudy weather and inaccessibility to the remote areas. Moreover, detailed LiDAR survey is not possible due to larger spatial extent. The only possibility is to collect data along the salt-water creeks and nearby mangroves.

1.6 Study Area

This study area (Figure 1-2) selected for this research is located at lat 34° 47' 7" S, 138° 32' 39" E in the North part of Adelaide and is known as St Kilda mangroves. The climate of this area is considered to be hot, humid and dry in summer and cold in winter season. This site mainly holds mangrove type (Figure 1-1) *Avicennia marina (*DEWNR 2007) that is surrounded by saltpans, sewage plants, industry and urban infrastructure. Moreover, some tourist destinations are also near mangrove sites such as an amusement park and Dolphin sanctuary. The main popular creeks are Barque creek, Garnets creek, Post creek, Burrows creek, Swan creek and Broad creek. Most of the field data collection points were sited along these creeks as other areas were not accessible. Moreover, western side of this study area includes Torren Island, which comprises of mangrove forest, salt marsh, power station and a conservation park. The main biodiversity of this region includes various ecosystems (*mangrove and saltmarsh*, *salt fields* and *seagrass beds*), native birds (*Australian pelican, Royal spoonbill*) and marine life (*George whiting, Juvenile king & Dolphins*). The Study area is given in Figure 1-2.

Figure 1-1: Mangrove Study Area

Study Area

Pléiades Neo
RGB : 1 2 3
Resolution : 1.3m

Date : 02-11-2023

ALOS-2 PALSAR
Polarization: L$_{HV}$

Backscatter
12
-33 dB

Azimuth

Range

INDONESIA

Coral Sea

AUSTRALIA

Esri, TomTom, FAO, NOAA, USGS,
Esri, USGS

Mangrove Biomass from Space

Description

The main aim of this research was to assess the capacity of satellite data to study mangrove aboveground biomass – AGB in South Australia. Mapping and quantitative assessment of above ground biomass (AGB) of mangroves may be possible using multiple remote sensing datasets such as optical, RADAR and LiDAR data supported by fieldwork. This study assessed South Australian (SA) mangroves (Avicennia marina) in the St Kilda area near Salisbury.

Spatial Reference
Projection : WGS 1984 UTM Zone 54S
WKID : 32754
Linear Unit : Meters

N

Author : Bassam Waheed
Date :   10 September 2025
Credits : ESRI, University of Flinders.

1   0.5   0   1   2   3
KM

Figure 1-2: Study Area

1.7 Thesis Structure

This overall structure of this thesis is organised in seven chapters. The structure is:

Chapter 1 presents mangrove introduction, benefits and problem statement. It also covers research aims and research questions.

Chapter 2 deals with literature review for this research, which includes a global review of above ground biomass – AGB and Australian mangroves in brief. Next, it is focused on mangrove studies which used LiDAR and field based methods. This is followed by a section discussing optical and RADAR satellites, machine learning methods, fusion approaches, PCA, GLCM matrix, statistical analysis and research gaps.

Chapter 3 lays out the methods and techniques that were used in this study. In addition, data sources for each satellite are given. Procedures and techniques are explained for each process used and illustration given in a workflow style. The general flow chart is also included in this section.

Chapter 4 discusses the significant findings of AGB estimations using multi-source satellites and that derived to address the research questions and aligned with the research scope.

Chapter 5 is focused on discussion about main findings which were set in research questions in chapter one.

Chapter 6 identifies the areas for future research and dedicated to recommendation and research conclusion.

References This section includes all of the references included to support this research.

Appendices This includes maps, graphs and charts, field report, photographs and relevant documentation, which were not added in the result section.

CHAPTER TWO : LITERATURE REVIEW

2.1 Introduction

This literature review introduces global mangrove distribution and mapping. It then reviews Australian and SA mangroves, mangrove ecosystems and above ground biomass – AGB mapping. LiDAR and field based methods are also explored as well as satellite based studies using optical & RADAR satellites. This chapter continuous to explore image classification techniques for mangrove extent and vegetation indices (VI) and statistical regression for AGB estimations. Lastly, pixel based fusion methods and finally, research gaps are addressed.

2.2 Global Mangrove Mapping

At global scale, mangroves were first studied between the period of 1960-1996 (Jia *et al.* 2023; Friess *et al.* 2019) and published in 1997 as World Atlas of Mangroves (WAM-1). Subsequently, FAO and UNEP continued to monitoring mangroves and published those maps as (WAM-2) in 2009 (Ximenes *et al.* 2023). Later, USGS provided mangroves maps based on Landsat classification, which was called Global Distribution of Mangroves (GDM) and published in 2011 (Giri *et al.* 2010). The latest, version was established with the name of Global Mangrove Watch (GMW) and published maps were available in 2018 (Bunting *et al.* 2018). Recent research on mangroves, (Islam *et al.* 2024) verified that, worldwide mangroves are distributed in 19 families and 70 species in 113 countries and their distribution covers an area about 15 million hectors. Table 2-1 presents the summary of worldwide mangroves extracted from Ximenes *et al.* (2023).

There are some discrepancies found as reported by researchers (Giri *et al.* 2010; Bunting *et al.* 2018). For example, according to WAM-1 in 1997 the total mangroves areas was 181,077 km^2. However, by WAM-2 it was 152,000 km^2. In 2011 by GDM it was reported 137,760 km^2. In 2018, it was reported 137,600 km^2 but mostly authors agreed that the total area seems to be reducing as compared with earlier comparisons. In current situations, mangroves are being observed by multiple organisations such as IUCN, JAXA, Aberystwyth University, UNEP and WCMC. In addition, every five year the data is updated and spatial extents are available.

Table 2-1: Global mangrove mapping statistics

Program	Published	Resolutions	Organizations	Area (km^2)
World Atlas of Mangroves (WAM-1)	1997	Multiple	-	181,077
World Atlas of Mangroves (WAM-2)	2009	30m	FAO, UNEP	152,000
Global Distribution of Mangroves (GDM)	2011	30m	USGS, NASA	137,760
Global Mangrove Watch (GMW)	2018	25m	JAXA, Aber uni, UNEP, WCMC	137,600

Some researchers, (Pham *et al.* 2018; Friess *et al.* 2019; Thomas *et al.* 2018) identified that mangroves are continued to be threatened by urban development, aquaculture and agriculture practices, local livelihood processes and coastal development. Most researchers (Goldberg *et al.* 2020; Contessa *et al.* 2023; Bunting *et al.* 2022; Brown *et al.* 2020) believe that, major drivers for mangrove loss are natural and anthropogenic. Thomas *et al.* (2018) proposed that 3.6 million hectare of mangroves were lost between 1980 to 2005.

2.3   Australian and SA Mangroves

Australia is amongst one of the few countries having 44 unique species of mangrove varieties in tropical and sub-tropical regions (Hutchings *et al.* 2019). In addition to that, Australia contains 6.4% of the world's mangroves area which is distributed over 11,000 km^2 along the coastal areas (DCCEEW 2017). This thesis will mainly focus on South Australian mangroves near the Salisbury region known as St Kilda region. In South Australia the most common mangrove type is *Avicennia marina* (Grey mangroves), which extends from South to East and normally appears to be two to five meter in height (DEWNR 2007). In Figure 2-1, Australian and SA mangrove distribution is shown.

(TERN 2025)
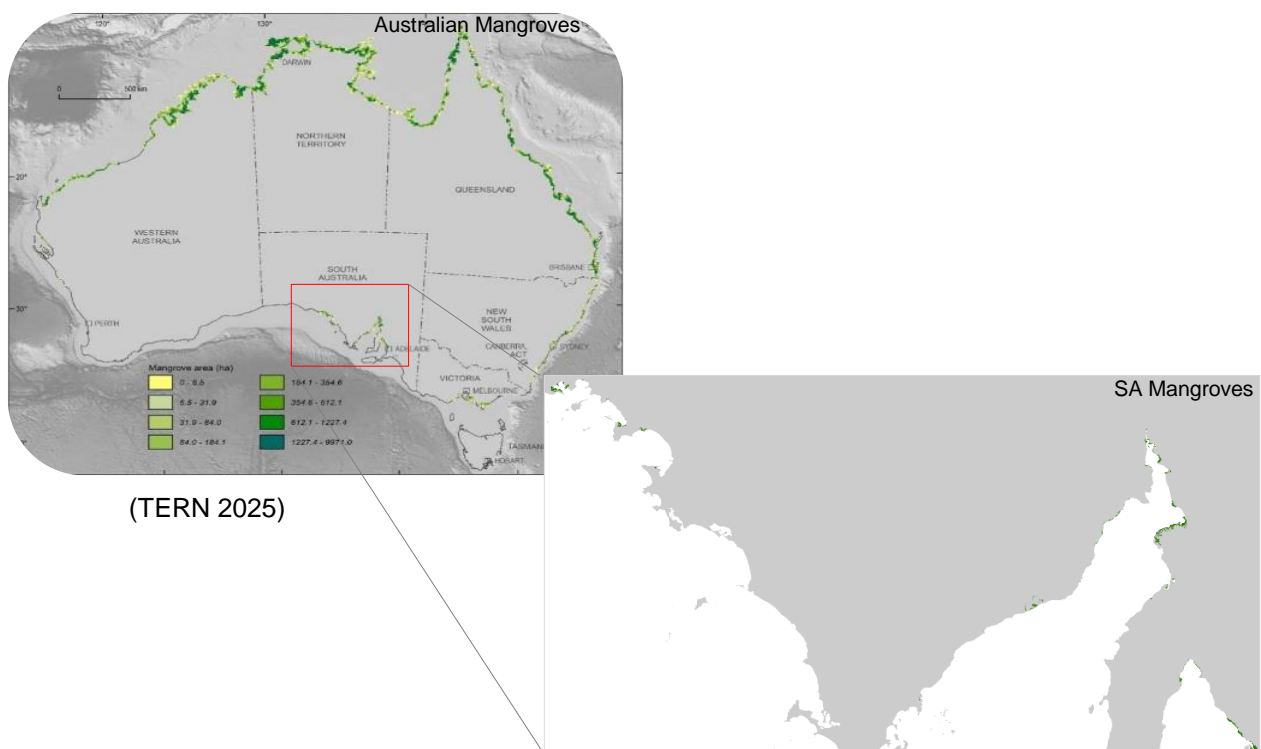
Figure 2-1: Mangrove distribution; Left: Australian mangroves; Right: SA mangroves

2.4 Blue Carbon

Blue carbon is a term, which is defined as the carbon storage in coastal environments. In contrast, green carbon referred as terrestrial forest carbon. In this research, the focus is on blue carbon stored in mangroves only. Roy *et al.* (2024) reported that, the carbon stored in a mangrove ecosystem can be defined as mangrove blue carbon. It has been observed by Choudhary *et al.* (2024), mangroves, sea grass and salt marshes are mainly responsible for carbon storage in a coastal ecosystem. To support this view, (Stankovic *et al.* 2023; Friess *et al.* 2019; Campbell *et al.* 2022) emphasized that the blue carbon ecosystem can play an important role in climate change mitigation if they are well monitored and managed. Jones *et al.* (2020) described that mangrove ecosystems are highly capable of storing carbon in above ground biomass and in its' sediments. Therefore, monitoring, modelling and estimation is so important to monitor blue carbon in coastal ecosystem and mangroves are a part of this. In an analysis of carbon, Malik *et al.* (2023) reported that, mangroves blue carbon stock depends upon its above ground biomass, below ground biomass, dead material and its related sediments.

2.5 Mangrove Ecosystems

Mangrove ecosystems are thought to be one of the most dynamic intertidal ecosystem that comprises of salty water, mud, sediments and complex root system, which appears to be partially above the water. They contain crustaceans, fish, animals, birds, other forest and shrubs (Friess *et al.* 2019; Alwis *et al.* 2025). All these species live in this system and rely on available resources in them. A couple of authors (Thomas *et al.* 2018; Maurya *et al.* 2021; Goldberg *et al.* 2020; Pham *et al.* 2019; Babiy *et al.* 2022; Goldberg *et al.* 2020; Jia *et al.* 2023) emphasised that, this system as a whole provides a significant ecological services as shown in Figure 2-2.
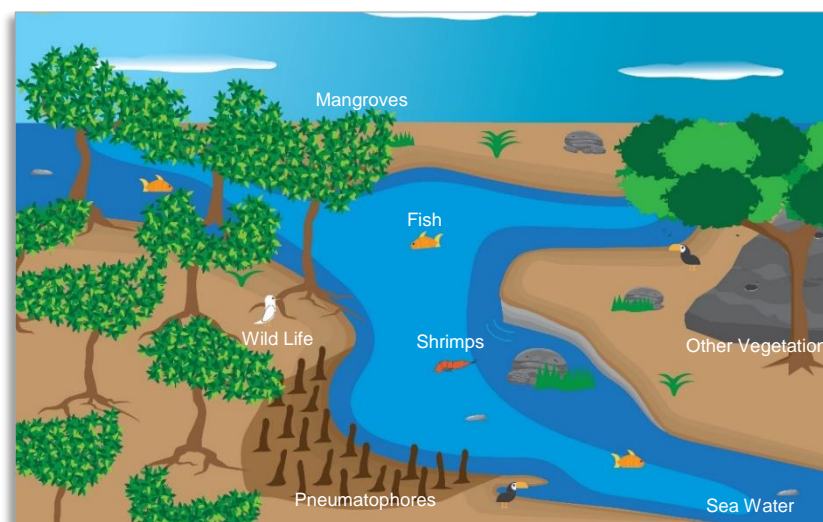
Figure 2-2: Mangrove ecosystem

2.6   What is Above Ground Biomass – AGB

Above ground biomass (AGB) is an organic material, present in leaves, stem, and above ground roots. In an investigation into AGB, Thomas *et al.* (2017) reported that mangrove plants mainly consist of above ground biomass – AGB and below ground biomass – BGB and both are helpful in calculating carbon storage. There are two primary methods to measure AGB; destructive and non-destructive. This study is based on non-destructive method (Komiyama *et al.* 2008; Kamal *et al.* 2022; Gitelson *et al.* 2003; Stovall *et al.* 2018b) of AGB estimation, as uprooting mangroves plants is restricted due to local regulations. Although, it has been found (Samra *et al.* 2025) that, the destructive methods have high accuracies but they are costly and time consuming. Researchers (Pham *et al.* 2019; Ximenes *et al.* 2023; Babiy *et al.* 2022; Jia *et al.* 2023; Friess *et al.* 2019; Goldberg *et al.* 2020; Ehlers *et al.* 2022) believe that mangrove biomass estimation is important to understand the carbon cycle, state of mangroves, ecosystem functions and for climate studies. A general concept of AGB is given in Figure 2-3.
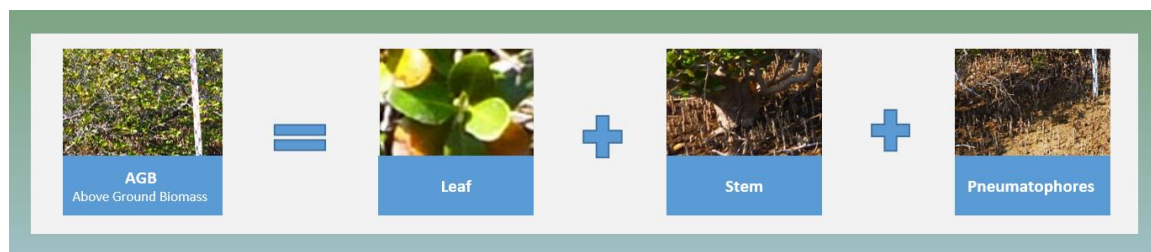
Figure 2-3 : Above ground biomass – AGB components

AGB importance cannot be denied in any agricultural application as a couple of researchers estimated biomass for grassland, crops and forest. For example, research studies (Ren & Zhou 2014, Pan *et al.* 2024; Riquelme *et al.* 2024) calculated AGB for grasslands to assess its productivity and canopy estimation. Similarly, Fu *et al.* (2014) measured AGB for wheat and Marcone *et al.* (2024) used it for spinach. In addition, AGB is measured in forest industry to study various ecological functions and carbon estimations. A series of papers from couple of researchers (Stovall *et al.* 2018a; Stovall *et al.* 2018b; Joetzjer *et al.* 2017; Su *et al.* 2024; Tanase *et al.* 2013; Santoro *et al.* 2022) where they calculated AGB for forest industry using remote sensing technologies. Likewise, this research intend to use the same approaches to measure mangrove AGB.

2.7   Remote Sensing of AGB

Previous studies (Farzanmanesh *et al.* 2024; Pham *et al.* 2020b; Jones *et al.* 2020; Jia *et al.* 2023; Huong *et al.* 2023; Wei 2010; Baloloy *et al.* 2018) suggested that remote sensing technologies have emerged as cost effective and time efficient techniques to estimate AGB. Although, some emphasis is also given in Chapter 1. There are many studies found on mangroves AGB research. Some researchers (Suardana *et al.* 2022; Huong *et al.* 2023; Bindu *et al.* 2020; Rahman *et al.*

2019; Thinley *et al.* 2024; Hirata *et al.* 2014; Farzanmanesh *et al.* 2024; Suardana *et al.* 2022; Nguyen *et al.* 2021; Wang *et al.* 2018; Doughty *et al.* 2021; Hu *et al.* 2020; Su *et al.* 2024) used optical remote sensing for mangrove extent and AGB using vegetation indices (VI) and regression. Others (Babiy *et al.* 2022; Pham *et al.* 2018; Lee *et al.* 2018; Harrell *et al.* 1995; Nandy *et al.* 2021; Austin *et al.* 2022; Saatchi *et al.* 2011; Ranson *et al.* 1997; Luckman *et al.* 1997; Cassol *et al.* 2021; Duncanson *et al.* 2020) used RADAR based datasets to study mangrove dynamics to calculate mangrove extent and AGB. Nevertheless, in all of these studies the importance of field work cannot be denied as it is not possible to calculate AGB without allometric equations where height and density are required. There are some studies (Fatoyinbo & Simard 2013; Simard *et al.* 2006; Aslan *et al.* 2022; Wong *et al.* 2020; Lagomasino *et al.* 2016; Lee *et al.* 2018; Wu *et al.* 2025; Jaramillo *et al.* 2018; Liao *et al.* 2020) where people try to get height from LiDAR, PolInSAR, InSAR techniques, TanDEM-X and SRTM. In another research Lucas *et al.* (2020), used multiple satellites datasets to study mangrove structure, and AGB. Henceforth, the role of allometric equations seems to be much important (Zanvo *et al.* 2023; Anees *et al.* 2024; Singh *et al.* 2023). Despite being labour intensive fieldwork it is important to collect DBH and wood density. To date, people are relying on remote sensing datasets, as they are non- destructive. Many researchers (Nandy *et al.* 2021; Pham *et al.* 2018; Lu et al; 2012; Hu *et al.* 2020; Sanam *et al.* 2024; Lucas *et al.* 2020) believe that, prediction of AGB is possible by integrating satellites and field data using statistical regression. A general concept multi-source remote sensing is given in Figure 2-3.
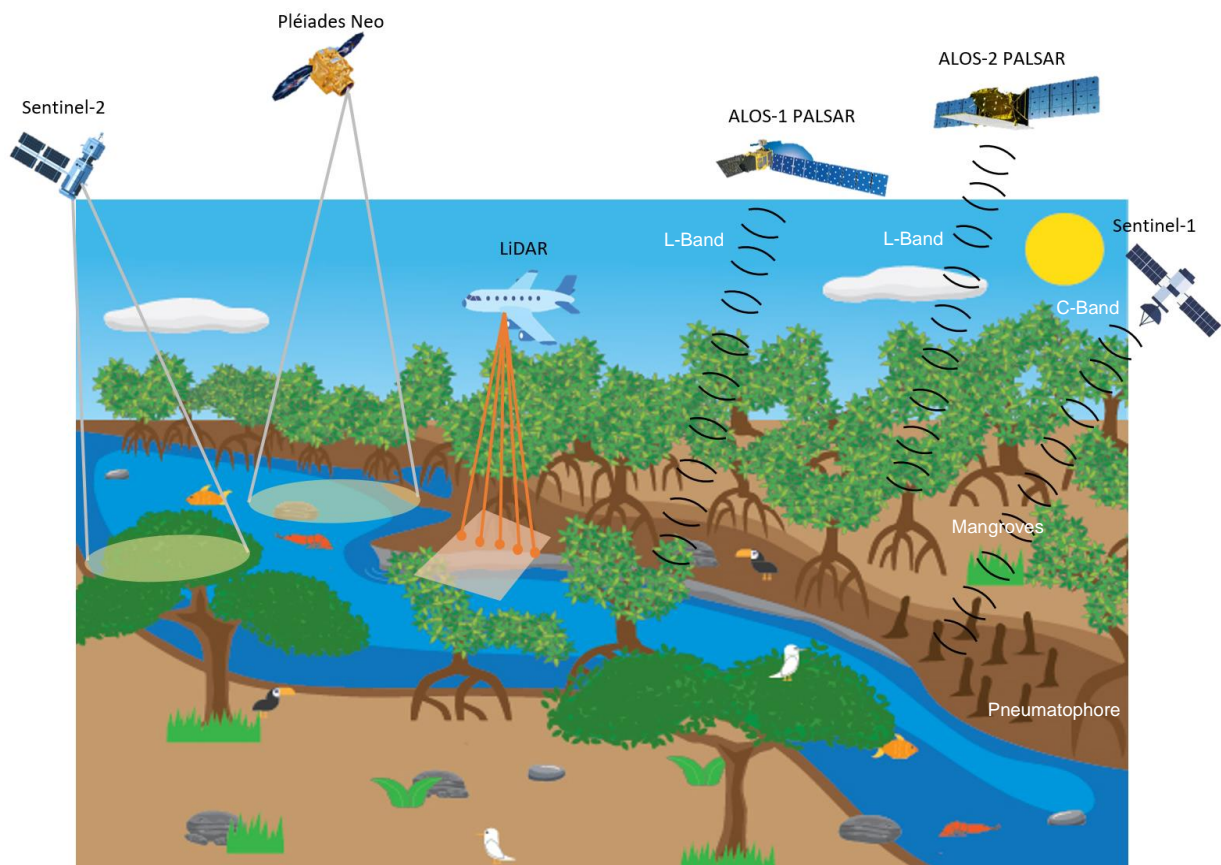
Figure 2-3: Mangrove study using multiple satellites

2.8 AGB Estimation from Field Measurements and LiDAR

The literature on field based AGB estimation (Hu *et al.* 2020; Samra *et al.* 2025) claimed that the field based methods might be labour intensive but possibly be more accurate in terms of results as compared to remote sensing techniques. However, this study is not going to collect the field data as it was collected in earlier work by university researchers. However, it will support satellite datasets measurements and help in regression analysis. To study *Avicenna marina*, many allometric equations are developed by researchers. Komiyama *et al.* (2008) reported that there are several allometric equations for various plant species of mangrove to calculate biomass. Some of them are generic and few of them are specific. In a follow-up study on AGB by Kamal *et al.* (2022) suggested that allometric equations are vital element in calculating AGB by using DBH and density. A study carried out by Wang *et al.* (2024) reported that field based methods are labour intensive and not cost effective. Below are few most common allometric equations for the field-based estimations. For instance, Komiyama *et al.* (2005) estimated AGB using Equation 2-1.

$$AGB = 0.251 * \rho * D^{2.46}$$ (Komiyama *et al.* 2005) **Equation: 2-1**

Here, ρ is the wood density (m^{-3}) and D is the diameter at breast height in cm and AGB in kilograms. Another, AGB equation found by Fu & Wu (2011) is given in Equation 2-2.

$$AGB = a(CD^2 * H)^b$$ (Fu & Wu 2011) **Equation: 2-2**

Here, CD represents crown diameter in m. H is height (m), *a* and *b* are coefficients and AGB measurements are in kg. There are many equations that are developed based on regions. A particular equation developed for *Avicennia marina* is given by in Equation 2-3.

$$AGB = (e^{-2.3902+0.4771*\ln(DBH)+1.945*\ln(D_{30})}) * 1.179712$$ (Jones *et al.* 2020) **Equation: 2-3**

Here, D_{30} is the diameter at 30cm, DBH is diameter at 130cm and AGB in kg. The most common approach to calculate AGB from LiDAR is canopy height model (CHM) which is extracted from subtraction of LiDAR$_{DSM}$ from LiDAR$_{DTM}$. This CHM is used as predictor variable to estimate AGB by applying regression with field based biomass.

2.9 Mangrove Study using Optical Satellites

2.9.1 AGB Estimation from Optical

Recently, AGB estimation from optical satellite imagery has drawn the attention of various researchers. A couple of them (Kamal *et al.* 2021; Farzanmanesh *et al.* 2024; Blanco *et al.* 2018; Thinley *et al.* 2024; Selvaraj & Pérez 2023a) described how vegetation indices (VI) such as NDVI, DVI, EVI, MVI and SAVI can be used as an explanatory variables to estimate AGB. In another research conducted by Wicaksono *et al.* (2015) used multispectral data for AGB estimation and carbon stock. Subsequently, another approach by Aseran *et al.* (2021) used NDVI from Landsat.

Unlike Aseran, Veiga *et al.* (2017) is more concerned with allometric equations to calculate biomass estimation. Some researchers combine allometric equations with optical VI to estimate AGB.

2.9.2 AGB Estimation from VI

In a comprehensive study of AGB Suardana *et al.* (2022) used vegetation indices NDVI, EVI and DVI as explanatory variables to calculate AGB. In another study, Neto *et al.* (2024) used Sentinel-2 data to derive NDVI (Equation 2-4), SAVI (Equation 2-5) and EVI to calculate AGB by applying regression. Therefore, optical satellites are a popular choice to calculate mangrove extent and a valuable option to calculate biomass supported by field data. In Figure 2-4, examples are given to calculate AGB using NDVI and SAVI through regression.
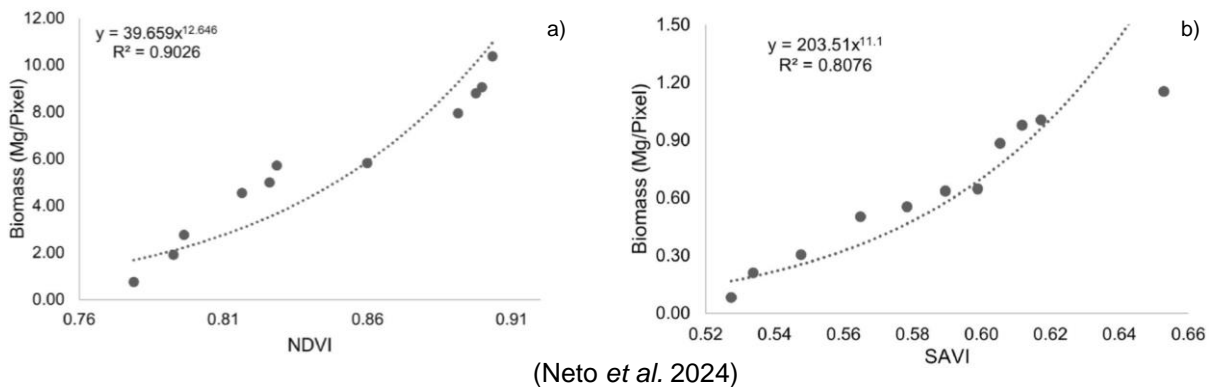
(Neto *et al.* 2024)

Figure 2-4: Examples of two regressions models using NDVI and SAVI

$$NDVI_{mb} = 39659 \; X \left(\frac{NIR - RED}{NIR + RED} \right)^{12646} \qquad \text{(Neto *et al.* 2024)} \qquad \textbf{Equation: 2-4}$$

$$SAVI_{mb} = 203.51 \; X \left[\frac{NIR - RED}{NIR + RED + L} \; X \; (1 + L) \right]^{11.1} \qquad \text{(Neto *et al.* 2024)} \qquad \textbf{Equation: 2-5}$$

In short, optical datasets seems to be good to measure upper canopy, mangrove extent and changes through time but field data is required to establish better correlation with AGB. To further examine AGB estimation through optical satellites Hamdan *et al.* (2013) used Landsat and SPOT-5 to calculate vegetation indices (NDVI, SAVI and OSAVI) and apply regression on these explanatory variables. In 2018, Wang *et al.* (2018) studied mangrove changes using Landsat. Previous research by Fatoyinbo *et al.* (2008) calculated mangrove extent from Landsat, height from SRTM and AGB using allometric equations. Vegetation based indices are very useful to extract information from satellite imageries. This information can extracted using two or more spectral bands. The most popular index for vegetation is NDVI and several studies (Baloloy *et al.* 2018; Aseran *et al.* 2021; Huong *et al.* 2023; Bindu *et al.* 2020; Yin *et al.* 2012) revealed a correlation between NDVI and field biomass. Therefore, NDVI is a key variable in this study to

estimate AGB as other researchers (Neto *et al.* 2024; Suardana *et al.* 2022; Hamdan *et al.* 2013) also believe the same.

Moreover, AGB estimation using high-resolution satellites has been done by many researchers. In a well-known study, Zhu *et al.* (2020) used high-resolution satellite WorldView-2 to identify mangrove species by vegetation indices and segmentation and also used regression to calculate biomass. Along the same line, Kamal *et al.* (2021) used WorldView-2 for NDVI and LAI to study mangrove net primary production, photosynthetic and evapotranspiration. Currently, WorldView-2, Pléiades Neo, PlanetScope, Geo-Eye, IKONOS, QuickBird are most common choices in higher resolution. Huong *et al.* 2023, considered Planetscope data to calculate NDVI and classification of data for AGB estimation. Likewise, Hidayatullah *et al.* (2023) used WorldView-2 data to calculate NDVI and EVI and regression approaches. A list of vegetation indices is given in Chapter 3, that will be used in this study. Considering all of this evidence, AGB estimation from VI appears to be positively correlated with field biomass.

2.10 Mangrove extent from Classification

Classification schemes (Khorram *et al.* 2016; Gao 2009; Richards, 2022) can be classified into two main groups: pixel and object based categories. The overall classification term is very broad however, Baghdadi and Zribi (2016) mainly divided into unsupervised and supervised. Popular unsupervised classification techniques are k-means classifier & ISO cluster and supervised techniques are SVR, Maximum Likelihood and RT (Pham *et al.* 2017; Pham *et al.* 2020a; Saim & Aly 2025). But, this study will be focus on RT and ISO cluster techniques for high resolution dataset Pléiades Neo. Maurya *et al.* (2021) and Su *et al.* (2024), suggested that random forest is a powerful classification technique, which can handle easily high dimensions of data. Tian *et al.* (2016) and Patnaik *et al.* (2021) described that it is based on decision trees and bootstrap aggregation. Huong *et al.* (2023) and Pham *et al.* (2018) used RT to calculate mangrove AGB estimations and various other researchers (Anees *et al.* 2024; Su *et al.* 2024; Lin *et al.* 2023; Nandy *et al.* 2021) used random forest technique to classify forest structure and AGB. In contrast, some researchers (Rahman *et al.* 2019; Borra *et al.* 2019; Liu & Mason 2016; Richards 2013) used unsupervised classification Iterative Self-Organizing Data Analysis technique (ISO cluster) scheme to get initial estimates, as it does not need any training data samples. It is believed that, this is very suitable technique if there is no field knowledge is available. No classification is complete until its accuracy checked and validated. The most common technique to check validation is a confusion matrix and kappa test which is written as in Equation 2-6.

$$\widehat{K} = \frac{p_0 - p_c}{1 - p_c} \qquad \text{(Mather \& Koch 2011)} \qquad \textbf{Equation: 2-6}$$

Here p_0 is an observed value and p_c is the chance value. This test will be perform to validate the accuracy of this RT classification. Confusion matrix gives the information about correctly classified

pixels against the total number of pixels. It helps us to identify errors in classify image by doing observation on the ground.

2.11 Mangrove Study using RADAR Satellites

2.11.1 AGB Estimation from RADAR Backscatter

RADAR is acronym for radio detection and ranging which works in a microwave region by transmitting and receiving microwave signals. Interestingly, this study is going to explore mangrove backscatter in both C-band and L-band of microwave region. In a Figure 2-5 the penetration depth for each band is shown.
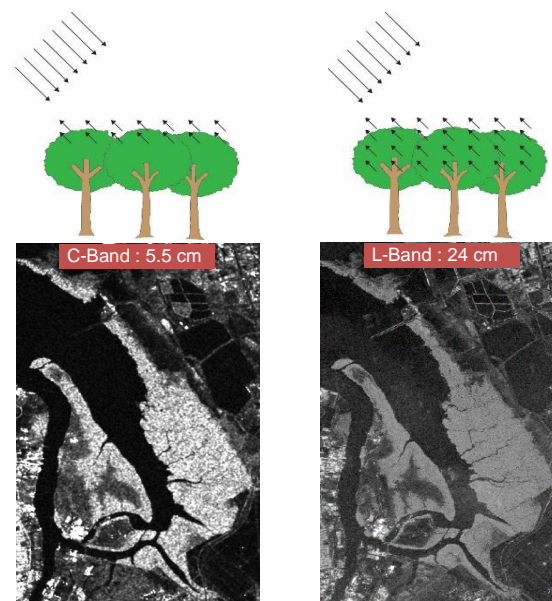
Figure 2-5: RADAR signal interaction with mangrove in C & L band

The potential of SAR imagery to study mangroves is very large, but the real advantage is the day and night capability. In a studies (Pham *et al.* 2019, Nesha *et al.* 2020; Pham *et al.* 2018; 2020a; Hamdan *et al.* 2014; Lucas *et al.* 2007; Naidoo *et al.* 2015; Mahasani *et al.* 2021; Pham & Yoshino 2016), it was shown that SAR is a good option to study biomass and structural properties of mangrove forest. The most favourite bands to study mangroves are (C, L and P) bands but Ghosh & Behera (2021) considered L-band to be more effective and consistent with the desired outcome. However, at the time of writing this literature review spaceborne P-band RADAR is not available. Moreover, RADAR data considered to have dual (HV, HH) and quad (HH, HV, VV, VH) polarisation depending upon the sensor capability. However, most favourite combinations for mangroves are HH and HV. In RADAR backscatter, mainly three scattering phenomena can be observed; surface, double bounce and volume scattering. Moreover, literature (Anderson *et al.* 2019; Brown *et al.* 2016; Fatnassi *et al.* 2023) shows that the most common scattering in mangroves is volume and double bounce scattering. In a Figure 2-6, different scattering types can be seen.
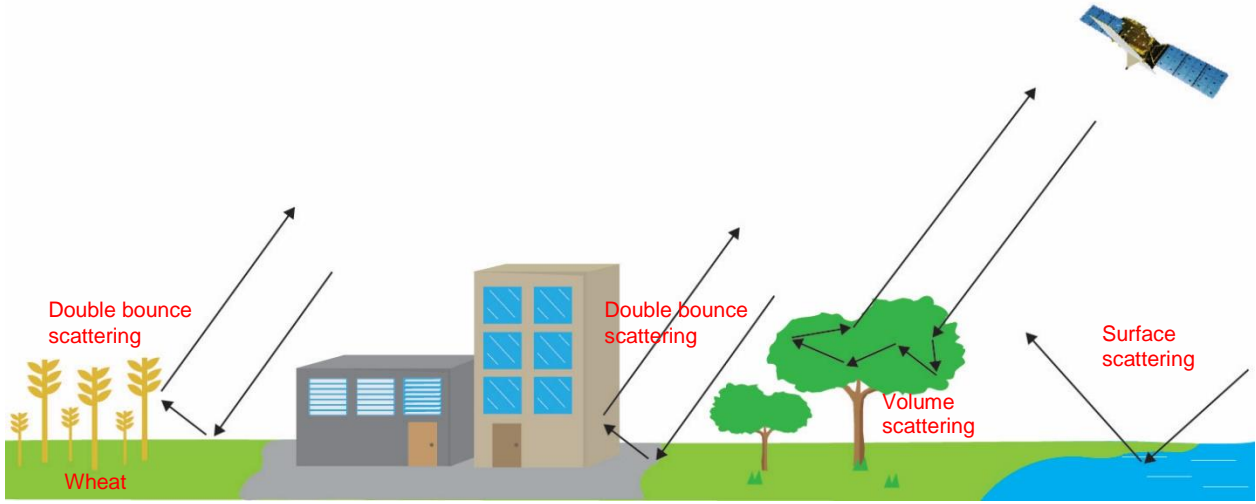
Figure 2-6: RADAR scattering types

2.11.2 AGB estimation from RADAR Vegetation Indices

Some researchers (Vaghela *et al.* 2021; Szigarski *et al.* 2018; Chen *et al.* 2023; Mandal *et al.* 2020) used RADAR based vegetation indices to calculate AGB. The most common index is radar vegetation index - RVI. In this study, RVI will be used to for AGB estimation by applying regression model. Additionally, canopy structure index – CSI and radar forest degradation index RFDI will also be utilised to explore hidden aspect of the mangroves forest. The normal values for RVI are ($0 \leq RVI \leq 1$) with 0 representing the landscape and 1 corresponding to healthy vegetation. The value of CSI ranges are ($-1 \leq CSI \leq +1$) with -1 depicting canopy vertical structure and +1 is the representing of horizontal structure. Moreover, RFDI values describes the denser and deforested landscape.

2.11.3 AGB Estimation from Decomposition

SAR polarisation considers the study of polarisation state of electromagnetic energy. The polarisation of SAR might be single polarised (H or V), dual polarized (H and V) and fully polarised (HH, HV, VH, VV). Cassol *et al.* (2021) used decomposition coefficients to measure AGB in Brazilian forest and Ghosh *et al.* (2021) and Zhang *et al.* (2023) used the coherence values to calculate AGB using IWCM model. Along the same line, Deodoro *et al.* (2024) used decomposition to study soil properties. It is one of the important parameters to study object properties. In general, scattering might be of two types; coherent and incoherent (Yamaguchi 2020). In coherent decomposition, the scattering matrix is used to describe the polarisation behaviour of the object. The scattering matrix is given in Equation 2-7.

$$S = \begin{bmatrix} S_{HH} & S_{HV} \\ S_{VH} & S_{VV} \end{bmatrix}$$ (Yonezawa *et al.* 2012) **Equation: 2-7**

In this study, model based Freeman-Durden and eigen-based (H-α) decomposition will be used for object behaviour and these decompositions can be calculated using covariance matrix (C3) or

coherency (T3) matrix. Mainly, Freeman-Durden decomposition models the scatter into three types; surface, double bounce and volume scattering. Mathematically, total scattering of the object can be written as in Equation 2-8.

$$[T] = [T_S] + [T_D] + [T_V] \qquad \text{(Mandal \textit{et al.} 2021)} \qquad \textbf{Equation: 2-8}$$

Here, $[T]$ is the total scattering. $[T_S], [T_D], [T_V]$ are surface, double bounce and volume scattering respectively. Cong Peng *et al.* (2025) used Freeman-Durden decomposition for AGB estimation of fir forest. Next decomposition, which is going to be explored is eigen-based decomposition, It is based on eigenvalues and eigenvectors. Equation 2-9 shows the three scattering components of this decomposition.

$$[T] = \lambda_1[T_1] + \lambda_2[T_2] + \lambda_3[T_3] \qquad \text{(Kumar \textit{et al.} 2023)} \qquad \textbf{Equation: 2-9}$$

Here, λ_1, λ_2 and λ_3 are eigenvalues and T_1, T_2 and T_3 are eigenvectors. In this composition, entropy, anisotropy and alpha angle will be calculated. The first component entropy values ranges are ($0 \leq H \leq 1$). Higher eigenvalues mean strong scattering like forest and agriculture fields. Next important parameter is α-angle and it value ranges from ($0° \leq \alpha \leq 90°$). $\alpha=0°$ displays single bounce, $\alpha=45°$ represents volume scattering and $\alpha=90°$ displays double bounce. Moreover, anisotropy refers to disparity of scattering based on eigenvalues. However, entropy, anisotropy and mean alpha angle can be calculated using Equation 2-10, Equation 2-11 and Equation 2-12 respectively.

$$H = \sum_{i=1}^{q} \left(-P_i log_q (P_i)\right) \qquad \text{(Chen \textit{et al.} 2020)} \qquad \textbf{Equation: 2-10}$$

Here P_i denotes probability of Eigen value. Moreover, α-angle can be written as mathematically.

$$\alpha = \sum_{i=1}^{3} (P_i \alpha_i) \qquad \text{(Ji \& Wu 2015)} \qquad \textbf{Equation: 2-11}$$

Here P_i is the eigenstate. Anisotropy can described as Equation 2-25.

$$A = \frac{\lambda_2 - \lambda_3}{\lambda_2 + \lambda_3} \qquad \text{(Yonezawa \textit{et al.} 2012)} \qquad \textbf{Equation: 2-12}$$

Here λ_2, λ_3 are the eigenvalues of coherency matrix. Henceforth, decomposition of mangroves using RADAR polarimetric is very useful for AGB estimations. In a recent decomposition study by Fu *et al.* (2023) used coherent and incoherent coefficients values to measure AGB of mangroves.

The detailed of RADAR characteristics, mathematical forms of polarisation vectors and polarimetric decomposition are given in Appendix F 1-1.

2.12 AGB Estimation from Data Fusion

Fusion is basically integration of two or more raster images or data to form a new raster from which to extract more information. Recently, some researchers (Sudiana *et al.* 2024; Saim & Aly 2025; Zhu *et al.* 2025; Selvaraj & Pérez 2023b; Schowengerdt, 2007; Konecny, 2014) used fusion approaches to extract features from satellite imagery and AGB estimation. They have merged optical datasets with RADAR or vice versa to improve outcome and to increase correlation among potential variables. Debastiani *et al.* 2019 used LiDAR, optical and RADAR data fusion for biomass estimation in Brazilian tropical forest. In a similar approach, Zhu *et al.* (2020) used fusion using LiDAR and WorldView-2 for mangroves AGB estimation. Likewise, (Mai *et al.* 2025) used LiDAR data with optical and RADAR for biomass estimation of mangroves. There are many approaches available for data fusion but (Pohl & Genderen, 2017; Chang & Bai 2018) has described into three general categories (Figure 2-7); pixel level fusion, feature and decision level. However, among those there are other techniques are available for multisensory data such as pan-sharpening, PCA, component substitution-CS, GLCM, high frequency injection (HFI), high pass filter (HPF), multi-resolution transformation (MRT) and statistical based regression approaches. The focus in this study will be into pixel level fusion of SAR and optical imagery. However, processes will also cover pan-sharpening, PCA and GLCM based approaches.
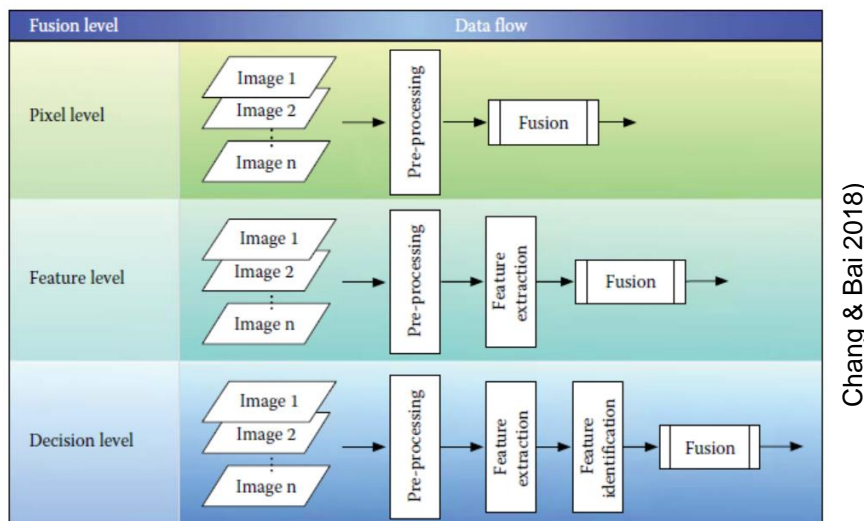
Figure 2-7: Different level of fusion approaches

The deeper insights of few fusion approaches (PCA, GLCM) are given in Appendix F 1-2 & Appendix F 1-3.

2.13 Statistical Analysis

This study utilises correlation and regression analysis for remote sensing variables. These explanatory variables are expected to be analysed against field$_{Biomass}$ through regression. The results from regression models will be helpful to calculate final AGB estimation. Regression is a very well-known statistical technique which is use to estimate dependent variable using

explanatory variables. Silva *et al.* (2018) used regression to calculate AGB from LiDAR of tropical forest and Lagomasino *et al.* (2016) used it for mangroves canopy height. The simplest form of regression is given in Equation 2-13.

$$y = mx + c$$

(Sullivan 2017) **Equation: 2-13**

Here, y is the response variable, x is the single explanatory variable and m is the slope of the line and c is the y-intercept. Many researchers (Fatoyinbo *et al.* 2018; Bindu *et al.* 2020; Li *et al.* 2024; Feliciano *et al.*2017; Neto *et al.* 2024) use regression to calculate mangrove biomass. Some of them (Effendi *et al.* 2024; Quang *et al.* 2022; Sainuddin *et al.* 2023; Harrell *et al.* 1995; Ovejero *et al.* 2023) used it for forest AGB estimations. But, if the multiple explanatory variables are involved, it is called multiple regression and its mathematical form can be represented as given in Equation 2-14.

$$y = \beta_0 + \beta_1 x_1 + \beta_2 x_2 + \beta_3 x_3 \ldots + \varepsilon$$

(Cassol *et al.* 2021) **Equation: 2-14**

Here y is the response variable, x_1, x_2, x_3 are explanatory variables, β_0 is the y-intercept and ε is the error.

2.14 Summary and Research Gaps

The evidence presented in this chapter, suggests that comprehensive research using multi-source datasets optical, LiDAR and RADAR to monitor mangrove spatial extent mapping, AGB estimation using remote sensing variables supported by field$_{Biomass}$ through regression may lead to valid estimates of mangrove AGB. Previous studies are available at global scale and narrow in focus at the regional level. Additionally, some of the datasets are having quality issues and not available at very high resolution. This study ultimately will lead to fill or improve a knowledge gap by studying a couple of remote sensing variables related to a specific species and a focused environment. Previously, not too many regression models existed for this area. Taken together, optical and RADAR based studies have not taken place for this area at high resolution before and especially there has been a lack in RADAR decomposition analysis. Moreover, little is known about fusion approaches for AGB estimation of this area.

CHAPTER THREE : METHODS

This chapter describes the methods and techniques, which are used to answer the research questions proposed in Chapter 1. Methods deals with AGB estimations from LiDAR and field datasets, optical, RADAR and fusion approaches. First, the chapter deals with the overall approach of methodology and discusses the data acquisitions and their analysis. Thereafter, it elaborates upon field data and LiDAR data analysis for AGB estimation used as "truth" for subsequent work. In the next section, the chapter elaborates pre-processing steps, analysis and procedures to calculate indices, GLCM matrices, PCA analysis and fusion processes to estimate AGB.

3.1   Main Research Approaches

This research mainly aimed to answers the research questions using following steps which are summarised in Figure 3-1 (See Appendix B 1-1 for detailed workflow).

Step 01

This step involved biomass estimation using field data. The results were provided for biomass estimation for each field sample point.

Step 02

This step included LiDAR data processing and extraction of CHM from DGM and DSM. Later, it involved biomass estimation by applying linear regression between $LiDAR_{CHM}$ and $field_{Heights}$ and as a result a biomass layer was produced to calculate AGB.

Step 03

Involved pre-processing of optical imagery (Pléiades Neo and Sentinel-2 satellites).

Step 04

This also involved extent of mangroves by performing various classification approaches such as RT and ISO cluster on Pléiades Neo_{8-band} composite and preparation of mangrove mask and classification validation.

Step 05

This involved calculation of vegetation indices such as NDVI, NDVIre and PCA for Pléiades Neo imagery and calculation of regression models.

Step-06

This step involved vegetation indices and PCA computation for Sentinel-2 imagery and preparation of regression models.

Step-07

This step involved pre-processing of RADAR imagery ALOS-1 PALSAR and Sentinel-1 in SNAP and mangrove AGB estimation from RADAR. This step also involved calculation of GLCM matrix and PCA and selection of best regression model.

Step-08

This step involved decomposition analysis using polarimetric RADAR data (ALOS-2 PALSAR) to calculate Freeman-Durden and H-α decompositions to explore biomass estimation. This also involved calculation of RADAR vegetation indices.

Step-09

This step involved pixel based fusion of optical and RADAR datasets and selection of best regression model through PCA.

Step-10

This step involved AGB estimations from LIDAR, optical, RADAR and fusion based on regression models and preparation of AGB maps.

Step-11

This involved spatial analysis of mangroves, using DEM and raster surfaces, such as distance to water, mangrove forest floor, astronomical tide level and NDVI comparison for biomass distribution and analysis.

Figure 3-1: General workflow diagram
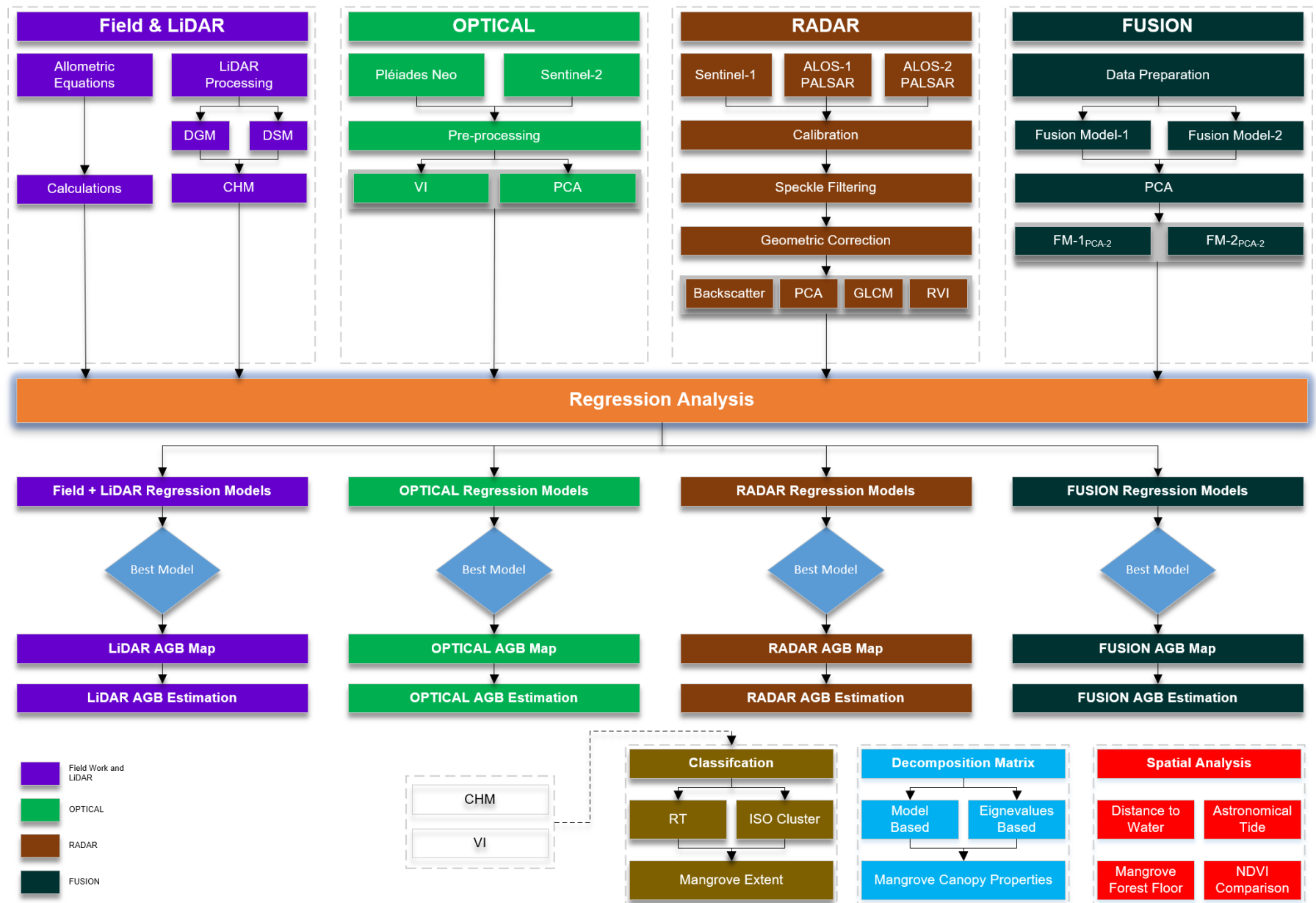
The detailed workflow chart is given in the Appendix B 1-1.

24

3.2 Field and LiDAR Data Acquisition and Processing

3.2.1 Biomass Estimation from Field

Field data was collected by a coastal team from Flinders University not including the thesis author and overall 26 points were measured using 10m buffer zones. Due accessibility and tough terrain, most of the points were accessible along the creeks only. From the field data, mean height values and biomass were noted for each buffer zone. Next, AGB was estimated for each buffer zone

Figure 3-2: Field & LiDAR workflow

using allometric equations as computed by many researchers (Jones *et al.* 2020; Vinh *et al.* 2019; Pandey *et al.* 2022; Tran *et al.* 2017; Zanvo *et al.* 2023; Komiyama *et al.* 2008) using the same approach. The overall workflow for field and LiDAR data is given in Figure 3-2. In this study AGB estimations and mangrove heights were provided by coastal team in a separate MS Excel sheet. The field sample points are available in Appendix C 1-1.

3.2.2 Biomass Estimation from LiDAR

LiDAR data was acquired by Airborne Research Australia (ARA) with 0.1m resolution and pre-processing was completed by ARA. This data was acquired with150m line separation in a grid format. In Table 3-1 LiDAR data characteristics are given.

Table 3-1: LiDAR data acquisition characteristics

Instrument name	Height	Pulse rate	Point density	Point spacing	Acquisition date	Company
Riegl Q680i	450m	400 kHz	~16 pts/m^2	0.42	17 Mar 2021	ARA

3.2.3 LiDAR$_{CHM}$ Processing

From the LiDAR data, a LiDAR$_{CHM}$ layer was generated, by extracting DSM from DEM, and produced a mangrove heights layer raster. In this study, LIDAR$_{CHM}$ was provided by ARA in individual tiles with a spatial resolution of 0.5m. Next, these tiles were mosaicked together and reprojected to to "WGS 1984 UTM Zone 54S" to maintain its interoperability with other datasets. After visual analysis, it was identified that, this canopy model LIDAR$_{CHM}$ exhibited some horizontal shift relative to other satellite datasets. Thus, this LiDAR$_{CHM}$ was geometrically corrected to Pléiades Neo imagery. After rectification, it was clipped to the study area boundary. The LiDAR$_{CHM}$ heights ranged from 0m to 24m which included features such as tall trees and power pylons. It was assumed from the field data and by field experts mangroves heights are thought to be found within the range of 0.5m to 12m in St Kilda area. Consequently, LiDAR$_{CHM}$ threshold values were set to 0.5m to 12m using "Con" tool in ArcGIS Pro.

3.2.4 Regression Models – LiDAR

To provide AGB estimation, first a relationship was established between field $Field_{Heights}$ and $LIDAR_{CHM}$ heights. To establish this relationship, first zonal statistics were calculated in $LiDAR_{CHM}$ for the 26 sample points in ArcGIS Pro using zonal statistics tool. These statistics provided $LiDAR_{CHM-max}$, $LiDAR_{CHM-mean}$, $LiDAR_{CHM-median}$ and $LiDAR_{CHM-PCT95}$. Thereafter, four scatterplots were constructed in MS Excel between mean $field_{Heights}$ and ($LiDAR_{CHM-max}$, $LiDAR_{CHM-mean}$, $LiDAR_{CHM-median}$ & $LiDAR_{CHM-PCT95}$) respectively and regression was applied to observe better R^2 value. A regression is useful tool to predict dependent variable as used by many researchers (Fatoyinbo *et al.* 2018; Effendi *et al.* 2023; Akay *et al.* 2009; Li *et al.* 2024; Feliciano *et al.* 2017). In this study, simple linear regression was applied to predict R^2 values for $LiDAR_{CHM}$. Initially, $LiDAR_{mean}$ and $LiDAR_{PCT95}$ was taken into consideration as the R^2 for both was of decent value. Later, after careful consideration $LiDAR_{CHM-mean}$ was selected for next analysis.

Next, a scatterplot was constructed between $field_{Heights}$ and $field_{Biomass}$ in MS Excel and regression was applied to generate regression equation and R^2 value. By using this relationship mangrove biomass was calculated from $LiDAR_{CHM-mean}$ (Wang *et al.* 2023; Mandal *et al.* 2024; Silva *et al.* 2018; Lagomasino *et al.* 2016). Regression equations are given in result sections.

3.2.5 Digital Elevation Model (DEM) Processing

To undertake spatial analysis of mangrove distribution DEM tiles were provided with a 0.1m resolution and then mosaicked together and clipped to the study area.

3.3 Optical Data Acquisition and Processing

For this study, two optical satellite images were acquired from Pléiades Neo and Sentinel-2. This optical imagery was used to biomass estimation (AGB) and mangrove extent. The acquisition dates and bands characteristics of optical satellites are given in Table 3-2. The general workflow of the optical processing is given in Figure 3-3.

Figure 3-3: Optical workflow
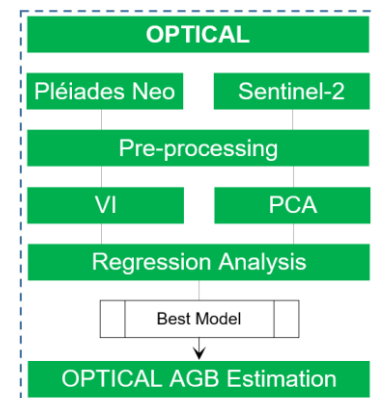
Table 3-2: Pléiades Neo and Sentinel-2 image characteristics

Name	Bands	Spatial Resolution		Acquisition date	Company
		Panchromatic	Multispectral		
Pléiades Neo	6	0.3m	1.2m	2 Nov 2023	Airbus
Sentinel-2	12	-	10m, 20m, 60m	11 Aug 2024 05 Nov 2023	ESA

3.3.1 Pléiades Neo Pre-processing

Pléiades Neo comprises of six multispectral spectral bands with 1.2m resolution and one band of 0.3m resolution in a Panchromatic mode. The detail of the spectral bands and resolutions are given in Table 3-3. (See Appendix B 1-1 for detailed workflow)

Table 3-3: Pléiades Neo bands characteristics

Spectral bands	Bands ranges	Resolution
Deep Blue	400 – 450 nm	1.2 m
Blue	450 – 520 nm	1.2 m
Green	530 – 590 nm	1.2 m
Red	620 – 690 nm	1.2 m
Red Edge	700 – 750 nm	1.2 m
NIR	770 – 880 nm	1.2 m
Panchromatic	450 – 800 nm	0.3 m

At first, Pléiades Neo multiple images mosaicked for panchromatic and all multispectral bands using "*Mosaic To New Raster*" tool in ArcGIS Pro stored as 16 bit unassigned format in a geodatabase. As a result, 6-band composite formed in which RGB represented as red, green and blue (3-2-1) and NED represented as NIR, red edge and deep blue (4-5-6) bands combination. The output cell size was set to 1.3m. Before moving on towards next processing, pan-sharpening was applied using Gram-Schmidt using "*Create Pan-sharpened Raster Dataset*" in ArcGIS Pro. The weight settings for band was set to default, which was 0.9 for red, 0.75 for green and 0.5 to blue bands. Later two 8-band composite were prepared Pléiades $Neo_{8\text{-bands}}$ and Pléiades Neo $Sharpen_{8\text{-bands}}$ by adding Pléiades Neo_{NDVI} and $LiDAR_{CHM}$.

3.3.2 Mangrove Extent from Classification

The mangrove extent was calculated using two different classification approaches mainly. The first one was random tree (RT), which is also known as random forest in literature (Anees *et al.* 2024; Maurya *et al.* 2021; Su *et al.* 2024). The second one was unsupervised ISO cluster (Rahman *et al.* 2019; Borra *et al.* 2019; Liu & Mason 2016; Richards 2013) to get the mangrove extent. Two composites Pléiades Neo $Sharpen_{8\text{-bands}}$ and Pléiades $Neo_{8\text{-bands}}$ which were prepared in earlier steps by composite them with Pléiades Neo_{NDVI} and $LiDAR_{CHM}$.

3.3.3 Supervised Classification – RT

Firstly, supervised classification random tree – RT (Tian *et al.* 2016; Patnaik *et al.* 2021; Nandy *et al.* 2021) on Pléiades Neo $Sharpen_{8\text{-bands}}$ composite of (0.3m) resolution was performed. While doing Pléiades Neo $Sharpen_{8\text{ bands}}$ classification there were eight classes (mangroves, salt marsh, mangrove water, sea water, barren land, agricultural fields, mangrove empty areas and mangrove

shadows) defined in training sample manger. After that, training samples were taken for each class in editor. Before classification, there was approximately 1022 training samples were taken in total for various land cover classes. While RT classification the main settings for maximum number of trees was set to 100 and minimum tree depth was 50. Setting for maximum number of samples per class was set to 1000. In the last step, class definition file was created to observe the weightage or participation of each raster layer in classification process. This classification was performed at 0.3m resolution. After classification, the outcome was reclassified for mangrove and non-mangroves zones using reclassify tool in ArcGIS Pro. After that, the area was calculated for mangroves using classification pixel count and the area of each pixel.

Likewise, random tree (RT) was performed on Pléiades Neo$_{8\,bands}$ composite at 1.3m resolution with land cover classes of (mangroves, mangrove shadows, salt marsh, mangrove water, barren land, white sheds and mangrove barren) areas. In this classification five classes were defined in training sample manger and 584 training samples were taken in total for each land cover class. The other setting for RT classification was same as performed earlier. Later, this classification was converted into mangrove and non-mangroves areas to calculate the area from Pléiades Neo$_{8\,bands}$.

3.3.4 Unsupervised Classification – ISO Cluster

Unsupervised classification – ISO cluster (Liu & Mason 2016; Rahman *et al.* 2019; Borra *et al.* 2019) was also performed on Pléiades Neo Sharpen$_{8\text{-bands}}$ and Pléiades Neo$_{8\text{-bands}}$. This classification was performed for both composites with twenty classes. The setting for maximum merge distance was 0.5 pixel and sample per cluster was set to 20 with a skip factor of 10. This classification was run for both composites at 0.3m and 1.3m resolution. Next, by visual analysis best mangrove classes were chosen and rasters was reclassified as mangroves and non-mangroves areas. After reclassify the rasters, areas were calculated from both images.

3.3.5 Accuracy Assessment for Pléiades Neo Classification

Next, accuracy assessment was planned for both unsupervised and supervised classification but due to time constraints, it was only performed on RT classified Pléiades Neo Sharpen$_{8\text{-bands}}$ as this was the best classification through visual inspection. 400 accuracy points were generated using stratified random sampling technique in ArcGIS Pro for mangrove and non-mangrove areas on the RT classified of Pléiades Neo Sharpen$_{8\text{-bands}}$. Later, these points were verified for mangroves and non-mangroves using google imagery and very high-resolution aerial imagery (10.5cm) acquired simultaneously with airborne LiDAR. Later, confusion matrix was calculated and a Kappa test (Mather & Koch 2011) was performed in ArcGIS Pro for error assessment.

3.3.6 Comparison of Mangrove Extent

The area of mangroves was computed among various classification results (RT & ISO Cluster) run on Pléiades Neo Sharpen$_{8\text{-bands}}$ and Pléiades Neo multispectral$_{8\text{-bands}}$. The following equation was

used to calculate the area for each classification.

$$Area = (h_{pixel}m * v_{pixel}m * total\ pixels)/1,000,000\ km^2$$

Here, h_{pixel} and v_{pixel} are satellite pixel size in meters and m is the measurement unit in meter. Later, a comparison was performed in in MS Excel for area calculation from two classification approaches on two different composite of Pléiades Neo (0.3m, 1.3m) resolutions.

3.3.7 Mangrove Mask – from RT Classification

Upon checking classification results, calculated areas were not demonstrating such a huge difference in measurements. Therefore, a binary mask for non-mangroves was prepared from the best classification result. This mask was used to clip other optical and RADAR datasets for mangroves.

3.3.8 Vector Datasets

In this study, there was some vector datasets were prepared such as mangrove study area boundary and marine water polygons and point data for creek names.

3.3.9 Sentinel-2 Pre-processing

In the processing of Sentinel-2 imagery all bands were transformed to the same resolution of 10m. In the final output, band 8A represented as 9th band and resampled 9th represented as band 10 etc. The RGB visual combination in Sentinel-2 was 8 4 3. At last, the masked image was prepared from this data. The spectral bands and resolutions are given in Table 3-4 (Pour *et al.* 2023).

Table 3-4: Sentinel-2 bands characteristics

	Spectral bands	Bands ranges		Resolution
B1	Aerosol	433 – 453	nm	60m
B2	Blue	458 – 523	nm	10m
B3	Green	543 – 578	nm	10m
B4	Red	650 – 680	nm	10m
B5	Red-edge 1	698 – 713	nm	20m
B6	Red-edge 2	733 – 748	nm	20m
B7	Red-edge 3	773 – 793	nm	20m
B8	NIR 1	785 – 899	nm	10m
B8A	NIR 2	855 – 875	nm	20m
B9	Water vapour	930 – 950	nm	60m
B10	SWIR Cirrus	1365 – 1385 nm		60m
B11	SWIR 1	1565 – 1655 nm		20m
B12	SWIR 2	2100 – 2280 nm		20m

3.3.10 Optical Indices – VI

Indices have crucial importance to identify changes in soil, water content and vegetation. In this study, six vegetation indices (Table 3-5) were calculated to assist in mangrove detection, health and calculation of biomass using regression. For Pléiades Neo, only two indices (NDVI and NDVIre) were calculated as they are very popular among the researchers (Aseran *et al.* 2021; Huong *et al.* 2023; Bindu *et al.* 2020; Yin *et al.* 2012; Liu & Zhu 2024). However, NDVI was the crucial for couple of reasons. One is for creating Pléiades Neo$_{NDVI}$ raster to improve RT classification. Secondly, to calculate the regression model, and lastly to have comparison between Pléiades Neo$_{NDVI}$ with Sentinel-2$_{NDVI}$ for mangroves regions. However, for Sentinel-2 all six indices were calculated as mentioned in Table 3-5. Among those, some of the indices were only calculated for Sentinel-2 such as the mangrove vegetation index (MVI), as it is commonly (Binh *et al.* 2022; Baloloy *et al.* 2020; Farzanmanesh *et al.* 2024) used to distinguish mangroves from other vegetation. Normalized difference moisture index (NDMI) which was used to identify water content and stress in mangroves. Additionally, combined mangrove recognition index (CMRI) was calculated from the difference of (NDVI & NDWI) to differentiate between mangroves and other vegetation types. Mainly, NDWI is used to detect surface water in wetland environments. For Sentinel-2, NDMI was used to see the mangrove reflectance response in shortwave infrared regions. All these indices were calculated in "Raster Calculator" in ArcGIS Pro by formulae given in the Table 3-5. Later, NDVI rasters were masked with the classification mangrove mask prepared in earlier steps and thresholded at a value of 0.30 to remove noise at the edges and negative values in the dataset.

Table 3-5: Popular optical vegetation indices for mangroves

Indices	Satellite	Formula	Authors
NDVI	Pléiades Neo Sentinel-2	$\dfrac{NIR - Red}{NIR + Red}$	(Ruan *et al.* 2022)
NDVIre	Pléiades Neo Sentinel-2	$\dfrac{NIR - RedEdge}{NIR + RedEdge}$	(Liu & Zhu 2024)
MVI	Sentinel-2	$\dfrac{NIR - Green}{SWIR1 - Green}$	(Binh *et al.* 2022) (Baloloy *et al.* 2020)
NDMI	Sentinel-2	$\dfrac{SWIR2 - Green}{SWIR2 + Green}$	(Taloor *et al.* 2021)
NDWI	Sentinel-2	$\dfrac{Green - NIR}{Green + NIR}$	(McFeeters 1996)
CMRI	Sentinel-2	$NDVI - NDWI$	(Gupta *et al.* 2018)

To calculate AGB estimations zonal statistics were computed in ArcGIS Pro for Pléiades Neo and Sentinel-2 indices. Later, correlation was performed in MS Excel between each vegetation indices and field$_{Biomass}$ and value of R^2 were noted.

3.3.11 PCA Analysis for Optical

To perform the additional analysis principal component analysis – PCA (Chuvieco 2016; Pham *et al.* 2018; Hirosawa *et al.* 1996; Estornell *et al.* 2013; Raja 2016; Younes *et al.* 2025; Canty, 2019) was performed on the two optical satellites (Pléiades Neo and Sentinel-2) in ArcGIS Pro. Firstly, PCA was calculated on Pléiades Neo using its six multispectral bands and output data file was generated to investigate eigenvalues for each component. Next, PCA was calculated for Sentinel-2 for its 12 bands. The main aim of PCA was to identify potentially hidden relationship in the datasets for mangrove and understanding of the band correlation. In the next stage, higher percentage values were noted and best components of PCA were identified. Next zonal statistics were calculated for best PCA layer and regression process was run and the best R^2 value was noted.

3.4 Mangroves Spatial Analysis

3.4.1 Distance to Water Analysis for Mangroves

To explore if there were any spatial trends in mangrove distribution, a water layer was extracted through the unsupervised classification of Pléiades Neo Sharpen$_{8-bands}$. The output raster was reclassified to extract the water only by applying binary mask approach in raster calculator. After that, raster data was converted into vector polygons. Next, majority filtering was applied to remove errors and tiny polygons using raster calculator in ArcGIS pro. To generalise the water polygons a spatial smoothing filter was applied at the end. Later, distance raster was generated using LiDAR$_{Biomass}$ raster and water layer by using "Distance Accumulation" tool in ArcGIS Pro. Then. LiDAR$_{Biomass}$ layer was combined with distance accumulation layer as a band composite and a scatter plot was constructed to identify if distance to marine water is important for mangroves distribution and above ground biomass (AGB).

3.4.2 Astronomical Tide Analysis for Mangroves

In this analysis, a DEM (0.1m) was prepared from LiDAR DEM tiles and resampled to 0.5m resolution, as 0.1m was not suitable for this analysis. After that, two threshold values of heights 0.3m and 1m was applied on DEM to extract two rasters (DEM$_{0.3m}$ & DEM$_{1m}$) ranges from 0 to 0.3m and 0 to 1m respectively. Next, these rasters were reclassified to display water levels at different tide levels of 0.3m and 1m of water. Mangroves height distribution from the LIDAR data was divided into three zones; low, medium and high and was displayed on two tides levels. The main purpose of this analysis to see how tidal height impacted the growth of mangroves in terms of its biomass.

3.4.3 Mangrove Forest Floor Analysis

For this analysis, the resampled version of 0.5m DEM of was used. This main purpose of this visualisation was to present the mangrove biomass distribution on the DEM to visualise underneath conditions of the mangrove canopy. This analysis finally represented catchments and

hidden channels under the mangroves canopy and mangrove distribution on ridges and near salt water creeks.

3.4.4 NDVI Comparison between Pléiades Neo and Sentinel-2

The main purpose of this analysis was to compare NDVI's values from two different satellites (Pléiades Neo and Sentinel-2). For this analysis, NDVI (Kamal *et al.* 2021; Huong *et al.* 2023; Hidayatullah *et al.* 2023; Zhu *et al.* 2020; Baloloy *et al.* 2018; Aseran *et al.* 2021; Bindu *et al.* 2020; Yin *et al.* 2012) was calculated for both satellites in raster calculator in ArcGIS Pro by standard NDVI formula as given in Equation 3-2.

$$NDVI = \frac{NIR - RED}{NIR + RED}$$

Equation: 3-2

Here, NIR represents the near infrared band and RED is the red band of the satellite. First, Pléiades Neo$_{NDVI}$ was calculated at 1.3m resolution then it was resampled to 5m to aligned with Sentinel-2 resampled NDVI of 5m. Likewise, Sentinel-2$_{NDVI}$ was processed at 10m resolution and resampled to 5m. Next, Pléiades Neo$_{RT}$ masked of 5m was applied on Pléiades Neo NDVI$_{5m}$ and Sentinel-2 NDVI$_{5m}$ to subtracted non-mangroves areas and a threshold value of (> 0.30) was applied to define the edges and remove the distorted edges in a raster calculator. Next, both NDVIs was classified in quartiles through symbology, which divided the pixel levels into four equal intervals. Lastly, both NDVIs rasters was reclassified in ArcGIS Pro using reclassification tool and classified NDVI into four different categories using symbology; Very High, High, Medium and Low.

3.5 RADAR Data Acquisition and Processing

RADAR imagery was acquired for three satellites; ALOS-1 PALSAR, ALOS-2 PALSAR and Sentinel-1. The main purpose of RADAR imagery to calculate the AGB using backscatter coefficients, PCA analysis, GLCM matrix analysis and RADAR based vegetation indices. Additionally, decomposition analysis was performed to study the scattering behaviour of mangroves. Table 3-6, presents RADAR characteristics, wavelengths, polarisations modes and acquisitions dates. (See Appendix B 1-1 for detailed workflow)
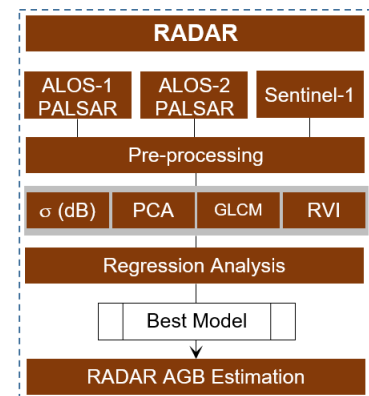
Figure 3-4: RADAR workflow

Table 3-6: ALOS-1, ALOS-2 and Sentinel-1 image characteristics

Name	Bands	Modes	Resolutions	Acquisition
ALOS-1 PALSAR	L-Band	HH, HV	7m - 10m	30 Oct 2010
ALOS-2 PALSAR	L-Band	HH, HV, VV, VH	3m, 6m, 10m	23 Oct 2023
Sentinel-1	C-Band	VH, VV	5m, 20m	03-Nov-2023

3.5.1 ALOS-1 PALSAR Pre-processing

The ALOS-1 PALSAR imagery was downloaded from Alaska Satellite Facility (ASF) facility for the date of 30th October 2010 in two polarization levels (HH, HV). The latest imagery for ALOS-1 PALSAR was not available as the satellite service was discontinued in 2011. Due to unavailability of latest imagery, it was ensured that at least season should be the same as with other imagery. To start the pre-processing it was imported into ESA SNAP software. At first, the image was calibrated using standard procedure and converted into sigma-naught (σ^o) (See Appendix F 1-1). Lee Sigma filter was subsequently applied to reduce the RADAR speckle and then geometric correction was applied with an output resolution of 14m approximately. SRTM 1sec HGT DEM was set as a reference with a resampling method of nearest neighbour. The output coordinate system was set to UTM Zone 54, South and datum was WGS84. Next, a subset was created using the previously created mangrove mask (see section 3.3.7) and backscatter data was converted into dB values. Table 3-7 provides basic characteristics of ALOS-1 PALSAR. The schematic diagram of this workflow is given in Figure 3-5. (See Appendix B 1-1 for detailed workflow)

Table 3-7: ALOS-1 PALSAR characteristics

Parameters	ALOS-1 PALSAR
Band	L-Band
Wavelength	22.9 cm
Frequency	1.27 GHz
Polarization	HH, VV
Process level	Level 1.1, 1.5, 2.1, 2.2
Sensor height	691.65 km
Revisit time	46 days
Launch date	2006
Organization	JAXA

ALOS-1 PALSAR

Image Credits : JAXA

Read — Calibration — Speckle Filter — Terrain-Correction

Amplitude_VH
Intensity_VH
Amplitude_VV
Intensity_VV

$\sigma^o[dB] = 10\log_{10}(DN)^2 + CF$ Lee Sigma

Subset — LinearToFromdB — Write

Sigma0_VH
Sigma0_VV
Sigma0_VH_db
Sigma0_VV_db
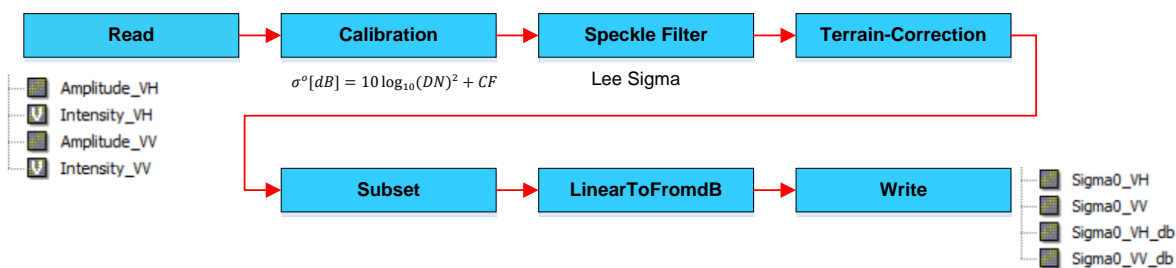
Figure 3-5: ALOS-1 PALSAR processing in SNAP for $\sigma°$

3.5.2 ALOS-2 PALSAR Pre-processing

The data for ALOS-2 PALSAR was acquired on 23-Oct-2023 and four polarisations (HH, HV, VV and VH) in three different data formats (Level1.1, Level1.5 and Level 2.1). From this data format σ^o was calculated and then complex data format was computed while doing calibration for decomposition analysis. Lee Sigma filtering process was applied with a sigma value of 0.9 and a

filter window size of 3x3. Number of looks was set to 1 with target window size of 7x7. σ^o was used to get final polarisation into decibels for analysis. By using this workflow four polarisation of σ^o (HH, HV, VH, VV) in decibel (dB) values were available for regressions analysis. The details of the processing is given in Figure 3-6. Level 1.1 the "raw" format, was acquired for development of decomposition matrices such as covariance (C3) and coherence (T3) matrices. Later, these metrics led to calculate advanced decompositions analysis such as Freeman-Durden for scattering based components and H-α to calculate eigenvalues associated with eigenvectors. The detailed workflow for complex data processing is shown in Figure 3-7. Moreover, Table 3-8 represents main characterises of ALOS-2 PALSAR. (See Appendix B 1-1 for detailed workflow)

Table 3-8: ALOS-2 PALSAR characteristics

Parameters	ALOS-2 PALSAR
Band	L-Band
Wavelength	22.9 – 25 cm
Frequency	1.257 GHz
Polarization	HH, HV, VH, VV
Process level	Level 1.1, 1.5, 2.1
Sensor height	628 km
Revisit time	14 days
Launch date	2014
Organization	JAXA
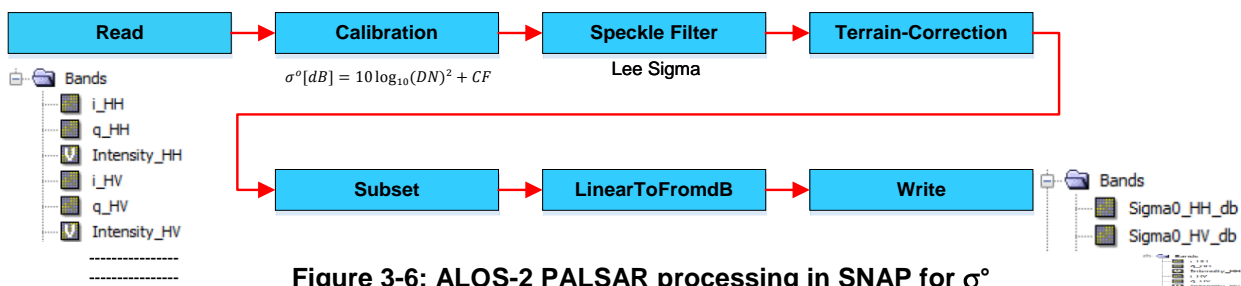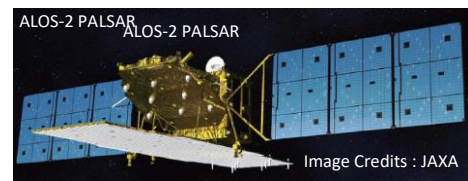
Figure 3-6: ALOS-2 PALSAR processing in SNAP for σ°
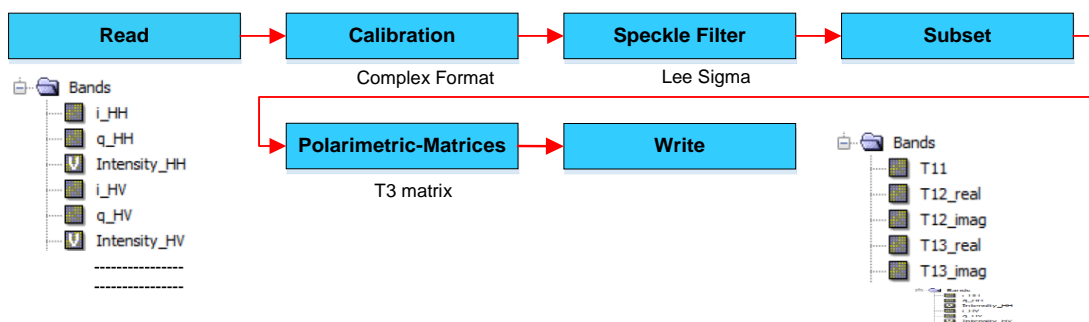
Figure 3-7: ALOS-2 PALSAR processing in SNAP for complex data

3.5.3 Polarimetric Decomposition

Two polarimetric decompositions (Cassol *et al.* 2021; Ghosh *et al.* 2021; Zhang *et al.* 2023; Deodoro *et al.* 2024; Yonezawa *et al.* 2012; Mandal *et al.* 2021; Kumar *et al.* 2023; Fu *et al.* 2023) were performed using T3 matrix, which was calculated in last step for ALOS-2 PALSAR. Polarimetric decomposition are only possible from complex data. Whilst many decompositions are available, Freeman-Durden and H-α were selected. Freeman Durden decomposition was calculated using T3 matrix in ESA SNAP to view the volume, surface and double bounce scattering in mangroves. Next terrain correction was applied to get the resultant image to align with other datasets. The details of the workflow for Freeman-Durden is given in Figure 3-8.
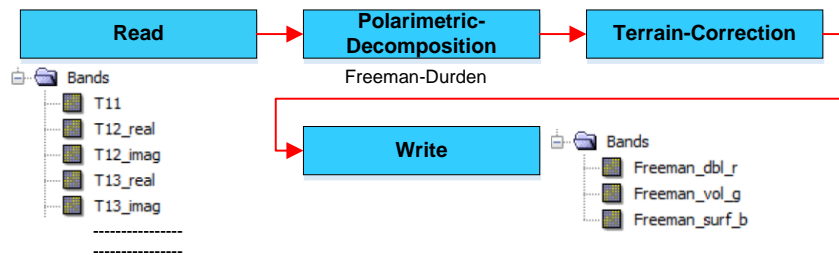
Figure 3-8: ALOS-2 PALSAR Freeman decomposition

Likewise, H-α decomposition was also calculated using T3 matrix to get entropy & anisotropy values and alpha angle in ESA SNAP and the final output was terrain corrected as described in Figure 3-9.
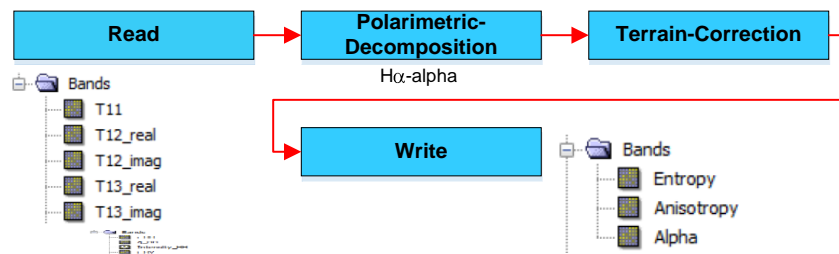
Figure 3-9: ALOS-2 PALSAR H-α decomposition

After processing in SNAP, it was found that there is a small misalignment of ALOS-1 PALSAR and ALOS-2 PALSAR outputs even though the projection was same for all datasets. To align with other datasets, it was georeferenced with the optical multispectral imagery of Pléiades Neo.

3.5.4   Sentinel-1 Pre-processing

Sentinel-1 data was acquired from Copernicus geoportal for the date of 03-Nov-2023. This was C-band data with dual polarisation (VH, VV). After downloading, it was directly imported in to SNAP software for processing. At first, the orbit file was applied to fix it. Next, calibration was applied followed by. Lee sigma filter for speckle reduction was applied and then geometric correction was applied to get the final outcome. Some important characteristics of the Sentinel-1 sensor is given in

a Table 3-9 and the general workflow diagram of Sentinel-1 pre-processing is given in Figure 3-10. (See Appendix B 1-1 for detailed workflow)

Table 3-9: Sentinel-1 sensor characteristics

Parameters	Sentinel-1
Band	C-Band
Wavelength	5 – 6 cm
Frequency	5.405 GHz
Polarization	HH, VV
Process level	Level – 1 S
Sensor height	693 km
Revisit time	12 days
Launch date	2014
Organization	ESA
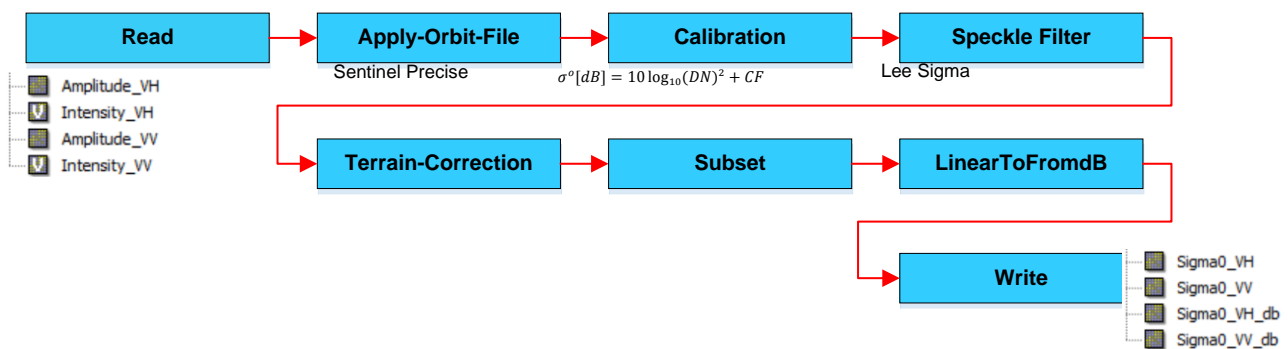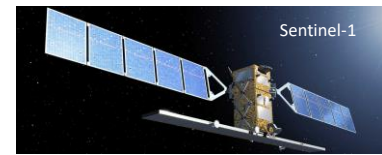
Figure 3-10: Sentinel-1 processing in SNAP

3.5.5 RADAR Indices – VI

Table 3-10 represents the RADAR based indices (Vaghela *et al.* 2021; Szigarski *et al.* 2018; Chen *et al.* 2023; Mandal *et al.* 2020; Joshi *et al.* 2015), which were calculated for ALOS-2 PALSAR to explore L-band properties with four polarisations. ALOS-2 PALSAR radar vegetation index (RVI) was calculated using Equation 3-3. The schematic diagram for ALOS-2 PALSAR RVI is given in Figure 3-11.

Table 3-10: Popular RADAR vegetation indices

Indices	Formula	Authors
RVI$_{Quad}$	$RVI_{(HH,HV,VH,VV)} = \dfrac{8HV}{HH + HV + VH + VV}$	(Szigarski *et al.* 2018)
RVI$_{Dual}$	$RVI_{(HH,HV)} = \dfrac{4HV}{HH + HV}$	(Mandal *et al.* 2020)
CSI	$CSI_{(HH,VV)} = \dfrac{HH - VV}{HH + VV}$	(Chen *et al.* 2023)

36

RFDI	$RFDI_{(HH,HV,VH,VV)} = \dfrac{HH - HV}{HH + HV}$	(Joshi *et al.* 2015)

The normal range for RVI index is 0 to 1. 0 describing landscape and 1 representing the healthy vegetation. Likewise, CSI ranges from -1 to +1. The values near -1 represents canopy vertical structure and values near to +1 describes horizontal structure of the canopy. Similarly, lower RFDI values < 0.3 represents denser forest and higher values of > 0.6 depicts the deforested landscape.
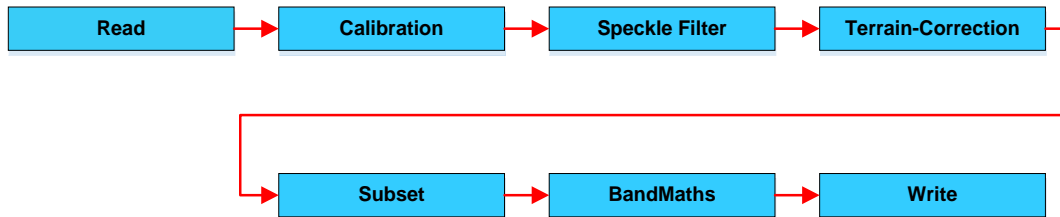
Figure 3-11: ALOS-2 PALSAR processing in SNAP for Indices computation

$$RVI_{ALOS\text{-}2} = (8 * Sigma0\_HV) / (Sigma0\_HH + Sigma0\_VV + (2 * Sigma0\_HV))$$

(Szigarski *et al.* 2018)   **Equation: 3-3**

Moreover, RFDI and CSI was only calculated for ALOS-2 PALSAR as it was quad polarised. Calculation for both indices were applied in band math in SNAP with Equations 3-4 and 3-5 respectively.

$$RFDI_{ALOS\text{-}2} = (Sigma0\_HH - Sigma0\_HV) / (Sigma0\_HH + Sigma0\_HV)$$

(Joshi *et al.* 2015)   **Equation: 3-4**

$$CSI_{ALOS\text{-}2} = Sigma0\_HH - Sigma0\_VV / Sigma0\_HH + Sigma0\_VV$$

(Chen *et al.* 2023)   **Equation: 3-5**

Additionally, RVI index for the dual pole ALOS-1 PALSAR and Sentinel-1 was calculated in SNAP using Equations 3-6 and 3-7 respectively.

$$RVI_{ALOS\text{-}1} = (4* Sigma0\_HV)/(Sigma0\_HH + Sigma0\_HV)$$

(ESRI n.d.)   **Equation: 3-6**

$$RVI_{Sentinel\text{-}1} = (4* Sigma0\_VH)/(Sigma0\_VV + Sigma0\_VH)$$

(CDSE n.d.)   **Equation: 3-7**

3.5.6 RADAR Principal Component Analysis – PCA

PCA analysis (Younes *et al.* 2025; Chuvieco 2016; Estornell *et al.* 2013; Raja 2016) was computed for ALOS-1 PALSAR, ALOS-2 PALSAR and Sentinel-1 imagery. After pre-processing of all RADAR imageries PCA component was computed for each. Firstly, ALOS-1 PALSAR backscatter (HH, HV) were taken into account to calculate PCA by selecting its two polarisations in SNAP.

Next, PCA values were computed for ALOS-2 PALSAR for all of its four polarisation. Lastly, Sentinel-1 PCA was computed for its two polarisations (VH, VV). The main procedure of all RADAR PCA's is given in the Figure 3-12.
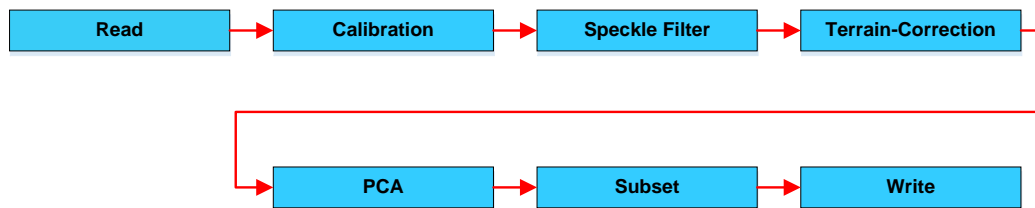
Figure 3-12: RADAR principal component analysis ─ PCA

3.5.7 RADAR GLCM Metrics

To explore RADAR texture or any noticeable patterns, gray level occurrence matrix – GLCM (Conti *et al.* 2025; Chunju Peng *et al.* 2025; Huong *et al.* 2023; Nandy *et al.* 2021) was calculated for ALOS-1 PALSAR, ALOS-2 PALSAR and Sentinel-1 in SNAP. Texture is the pattern of intensity variations and is important to characterize the identified objects. The purpose of this to study the characteristics of the image based on specific relationship in the image or to identify textural variations based on neighbouring pixels. GLCM matrix was calculated in SNAP using probabilistic quantizer with window size of 9x9. The quantization level was set to 32 bit and angle value was set to "All". These values were calculated for contrast, dissimilarity, homogeneity, ASM, energy, maximum probability, entropy, mean, variance and correlation. The main workflow is given in Figure 3-13.
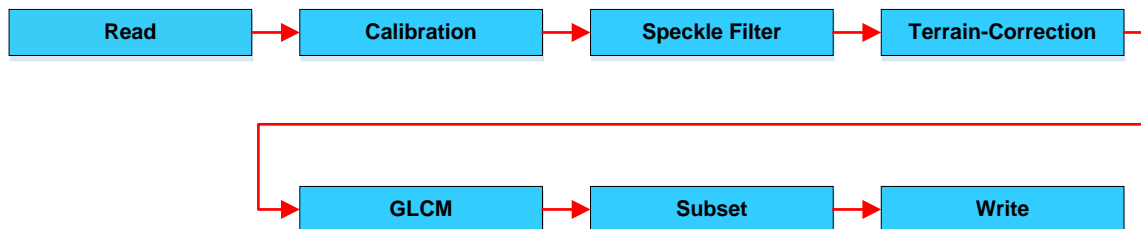
Figure 3-13: GLCM matrix

3.5.8 Regression Models from RADAR

From the RADAR, there were twelve regression models computed. Firstly, regression was applied between RADAR backscatter (Sainuddin *et al.* 2023; Saatchi *et al.* 2011) and field$_{Biomass}$ in SNAP using correlative plot tool by applying mangrove extent and field$_{Biomass}$ data. The resultant R^2 values were noted for each backscatter coefficient. Next, the same approach was applied for RADAR vegetation indices, PCA and GLCM (Younes *et al.* 2025; Estornell *et al.* 2013; Selvaraj *et al.* 2023; Huong *et al.* 2023) matrices to observe R^2 values and their relative regression equations. Consequently, R^2 values were calculated for each potential category for all RADAR satellite (ALOS-1 PALSAR, ALOS-2 PALSAR and Sentinel-1 in ESA SNAP.

3.6 Fusion Data Preparation and Processing

Fusion approaches are very well known to be extract the complex values from the data (Debastiani *et al.* 2019; Sudiana *et al.* 2024; Mai *et al.* 2025). Thus, a pixel based fusion approach was used to explore the heterogeneity of the satellite data through explanatory variables to predict AGB. There were two fusion models were generated; first was ALOS-2 PALSAR and Pléiades Neo and second was ALOS-2 PALSAR and Sentinel-2 (Figure 3-3). (See Appendix B 1-1 for detailed workflow)
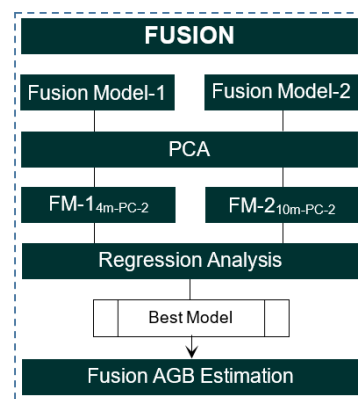
Figure 3-14: Fusion workflow

Preparation of the first fusion (Mai *et al.* 2025) model F1$_{4m-10bands}$
Pléiades Neo composite used 6-bands (B1, B2, B3, B4, B5, B6) in "Composite Band" tool and then resampled to 4m in GeoTIFF format. Next, ALOS-2 PALSAR (HH, HV, VH, VV) was imported in ArcGIS Pro and composite was prepared using four polarisations and resampled to 4m to make the same spatial resolution aligned with Pléiades Neo. After preparation of each band composite for both Sentinel-2 & ALOS-2 PALSAR they were fused together using pixel-based approach. Next, it was clipped to the study area and PCA was computed on 10-band composite (F1$_{4m-10bands}$) and a log file was exported to identify the best component based on eigenvalues. After that, zonal statistics were calculated for PC-1, PC-2 and PC-3. Then, tabular statistics table were joined together with mean field$_{Biomass}$ by taking "plot" as primary key. Next, scatter plots were drawn between each PC and field$_{Biomass}$ to observe the R^2 value.

The second fusion model F1$_{10m-8bands}$ had used ALOS-2 PALSAR and Sentinel-2. First, Sentinel-2 imagery (B2, B3, B4, B8) was imported into ESA SNAP with a resolution of 10m. Next, ALOS-2 PALSAR data was imported and pre-processing (calibration, filter, and geometric correction) was completed. After that, subset was created for the study area in both images. In next, collocation was applied to take all of bands in one dataset. Later, PCA was calculated on the this band set. After that, study boundary and mangrove mean biomass file was imported into SNAP and R^2 was calculated using correlative plot.

3.7 Optimal Biomass Models

Lastly, AGB estimations were carried out from best regression models (LiDAR, optical and RADAR) in each domain. The calculation procedure was almost same in each category except the resultant regression equations. The relevant equations are given in Chapter 4 along with their biomass layer. To calculate biomass, firstly the remote sensing variable was chosen based on best R^2 value and then masked with mangrove RT classification to remove non-mangrove areas. This masking was prepared earlier in classification process (see section 3.3.7). After that, exploratory variable (x) was replaced with masked layer in regression equation and new biomass layer was

generated for each category (LiDAR, optical & RADAR) in ArcGIS Pro. Finally, total biomass was calculated in tons using that biomass layer.

3.8   Software used

The main software used in this research is described in Table 3-11.

Table 3-11: Software used in this project

Software	Purpose
ArcGIS Pro 10.3	Mapping, Geo-processing, Geodatabases
ESA SNAP 9.0	SAR data processing, Data calibration, Filtering Geometric correction
ENVI 5.4	Raster data analysis
Microsoft Excel	Statistical analysis
Microsoft Word	Report writing
Microsoft Visio	Workflow diagrams

CHAPTER FOUR : RESULTS

This chapter describes the results of the processes, described in Chapter 3 to answer the research questions posed in Chapter 1. The first section, addresses the field and LiDAR based data outputs. In the next section, mangrove extent results and AGB estimation from optical data using two satellites (Pléiades Neo and Sentinel-2) are presented; further this section describes some deeper insights of mangrove spatial analysis. This is followed by results from AGB estimation from RADAR satellites (ALOS-1 PALSAR, ALOS-2 PALSAR & Sentinel-1) and thoughtful consideration of decomposition methods for mangroves. Finally, fusion-based approaches for assessing mangrove AGB are presented.

4.1   Biomass Estimation from Field Data

For this project, field heights and biomass data was provided as project reference so, it was just analyzed for the field heights and biomass using 26 sample points and became the control for next stages of the research. Surprisingly, this control data showed a high R^2 value (0.87) which indicated that there is high correlation between mean $field_{Heights}$ and $field_{Biomass}$ for the 26 sample points. The samples points are given in Appendix C 1-1. The biomass values were ranges between 13 t h^{-1} to 136 t h^{-1} with an average value of 59.7 t h^{-1}. The minimum value of AGB $\approx$13 t ha^{-1} was observed for the 1.5m of mean height. As this research showed high correlation between field height and biomass, this regression model was adopted for satellite based analysis (Figure 4-1). A regression summary for field based AGB and field heights is given in Table 4-1.
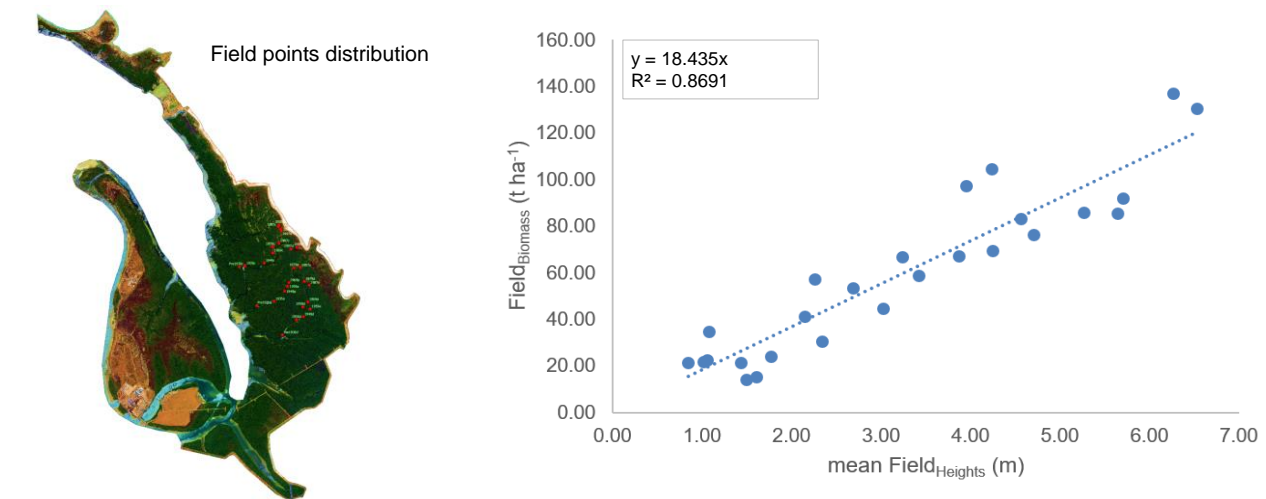
Figure 4-1: Left: distribution of field sample points; Right: Correlation scatter plot between field AGB and mean field$_{Heights}$

Table 4-1: Summary statistics of the regression model of mean field$_{Heights}$ and field$_{Biomass}$

Regression Statistics	
Multiple R	0.93237819
R Square	0.869329089

Adjusted R Square	0.863884468			
Standard Error	13.00981355			
Observations	26			

ANOVA

	df	SS	MS	F	Significance F
Regression	1	27024.56296	27024.56296	159.6675	4.25979E-12
Residual	24	4062.125967	169.2552486		
Total	25	31086.68893			

	Coefficients	Standard Error	t Stat	P-value
Intercept	-1.069490536	5.443963193	-0.196454402	0.845909
Field Heights$_{mean}$	18.69187904	1.479260616	12.63596072	4.26E-12

4.2　Biomass Estimation from LiDAR

4.2.1　Relationship Between Airborne LiDAR$_{CHM}$ and Field$_{Heights}$

LiDAR based AGB estimation was derived from canopy height model (CHM) by subtracting DTM from DSM. To determine AGB from LiDAR a first relationship was established between mean field$_{Heights}$ and LiDAR$_{CHM}$ mean heights for the field sample points. As a result, a linear relationship was established using the best-fit model for heights. In addition, CHM$_{mean}$, CHM$_{max}$, CHM$_{median}$ and CHM$_{PCT95}$ regressions were also calculated. In the analysis, linear and exponential models were found to be the best to correlate mean heights of LiDAR$_{CHM}$ and field$_{Heights}$ as shown in Figure 4-3a. However, for simplicity, it was decided to use linear model in correlation. During this analysis, LiDAR$_{CHM}$ heights were considered as response variable and field$_{Heights}$ were considered as explanatory variable. The result obtained from this relationship showed the R^2 value of approximately 0.87 in a linear model. In Figure 4-2: LiDAR heights of mangroves are shown in a 3D view.
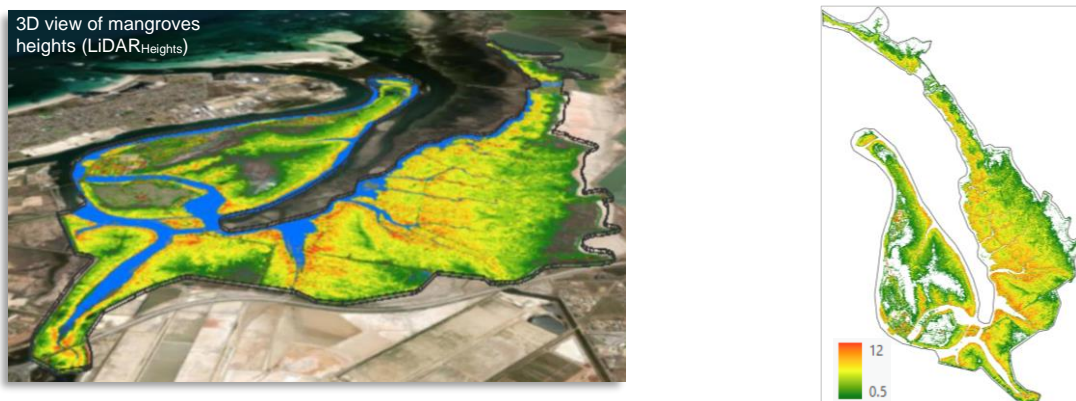
Figure 4-2: Distribution of LIDAR$_{CHM}$ heights in 3D

Figure 4-3b presents box and whisker plot for possible combinations of LiDAR heights (CHM$_{mean}$, CHM$_{max}$, CHM$_{median}$ and CHM$_{PCT95}$) and between field$_{Heights}$. From the graph, it can be seen that the mean values of LiDAR$_{CHM}$ ranges between 1m to 7m. In contrast, mean field heights values starts

from 0.84m to 6.53m. This shows that, there is half-meter difference between LiDAR$_{CHM}$ and field$_{Heights}$ mean heights.
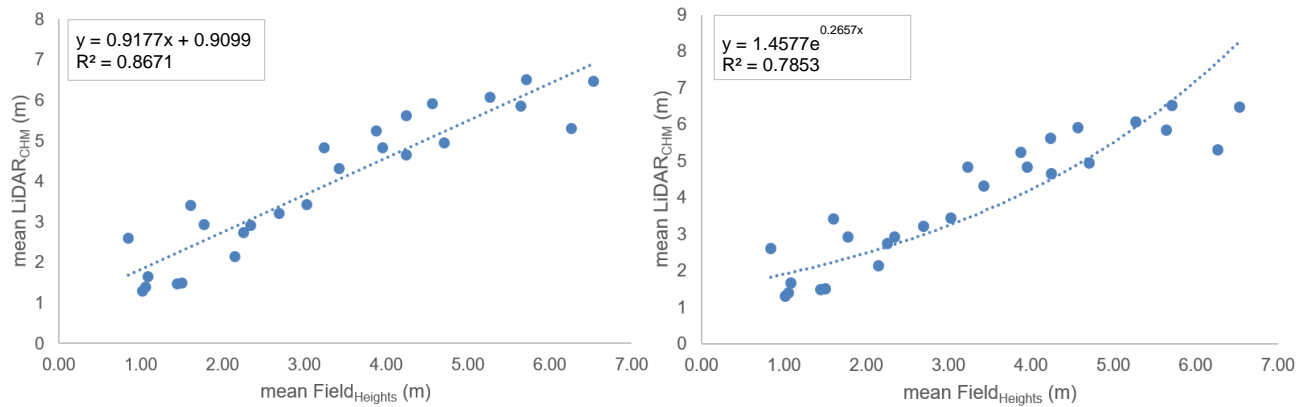
a) Correlation scatterplot between mean heights (LiDAR$_{CHM}$ and field$_{Heights}$); Left (Linear regression); Right (Exponential regression)
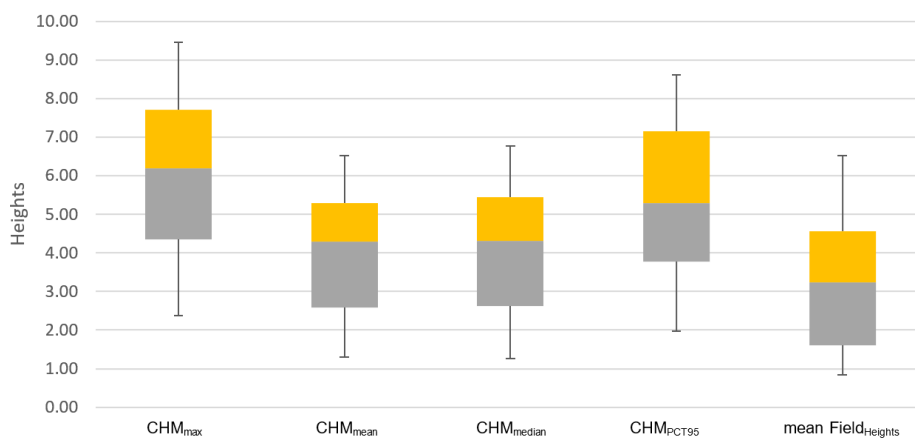
b) Box and whisker plot for LiDAR$_{CHM}$ and based field$_{Heights}$

Figure 4-3: Graphical representation of LiDAR$_{CHM}$ and field$_{Heights}$

4.2.2 Relationship Between LiDAR$_{Heights}$ and Field$_{Biomass}$

To calculate AGB, a regression was applied between LiDAR$_{Heights}$ and field$_{Biomass}$. The resultant value of (R^2=0.74) showed that this model can explain only 74% of the biomass variation. The correlation scatter plot for this analysis has shown in Figure 4-4.
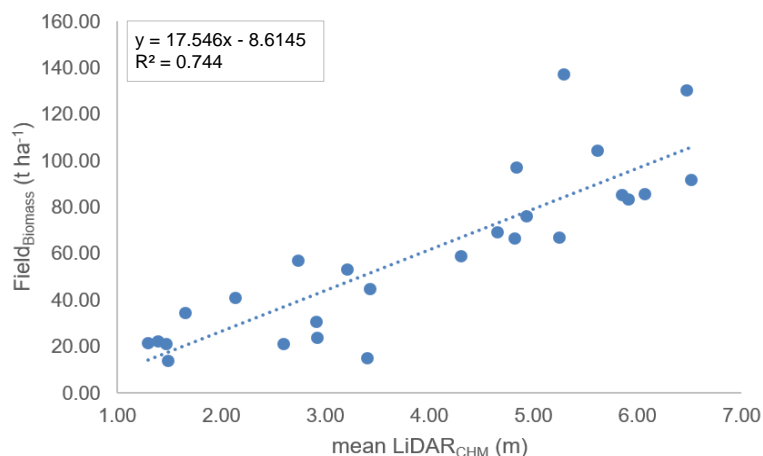
Figure 4-4: Correlation scatterplot between mean LiDAR$_{Heights}$ and field$_{Biomass}$

4.2.3 Optimal Biomass model from LiDAR

The best LiDAR$_{CHM}$ model was derived from LiDAR canopy height model (CHM) using regression with a R^2 value of 0.74 (Figure 4-5a). This value of R^2 was statistically significant and was able to explain 74% of the biomass variant.

$$y = 17.546x - 8.6145$$

Equation: 4-1

The biomass layer was computed using Equation 4-1 and shown in Figure 4-5c. The predicted biomass values were ranged between 0.15 to 202 tons h^{-1} with a mean value of 74.42 tons h^{-1}. The canopy height model (CHM) yielded a total biomass of 96,149 tons. In Figure 4-5b, quartile ranges Q1=51.63, Q2=72.37, Q3=95.64 are shown for biomass values in a whisker model and min and max values are shown in graphical representation. The detailed map is in (Appendix A 1-1).

a)

b)

c)
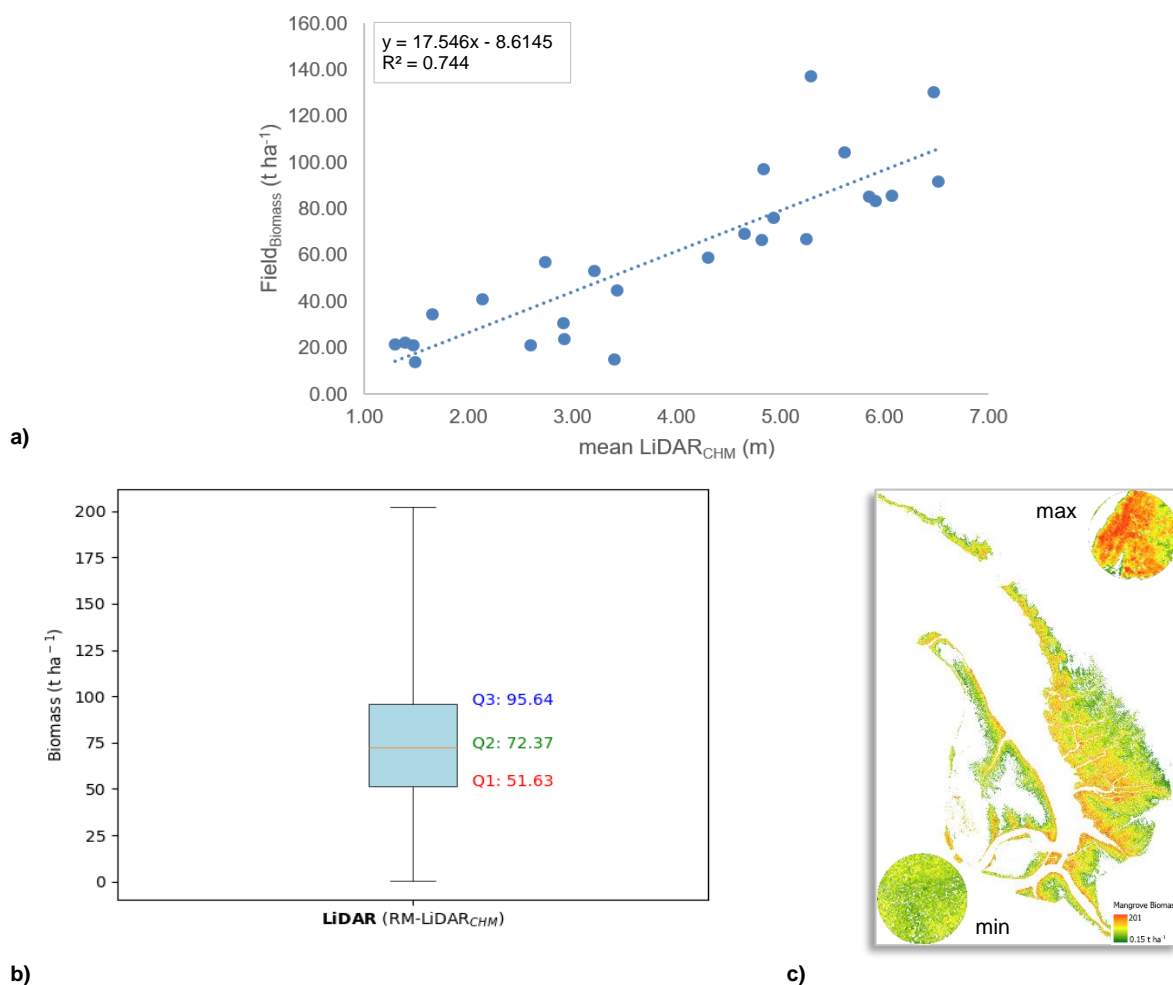
Figure 4-5: Biomass estimation from LiDAR regression model

4.2.4 LiDAR$_{Heights}$ Ground Truth

To validate LiDAR$_{Height}$ values an additional field survey was conducted for the study site. It was found that there are minor discrepancies between LiDAR$_{Heights}$ and manual field$_{Heights}$. The detail of the survey and photographs are given in Appendices C 1-2, C 1-3.

4.3   Biomass Estimation from Optical Data

In this study, optical data from two satellites Pléiades Neo and Sentinel-2 was used to explore mangrove AGB through vegetation indices, principal component analysis-PCA and machine learning approaches such as random trees (RT) and ISO cluster based classifications.

4.3.1   Pléiades Neo Pre-processing

Figure 4-6 represents Pléiades Neo datasets. Here mangrove reflectance pixels in panchromatic, RGB (Red, Green, Blue) and NED (NIR, RedEdge and Deep Blue) can be observed. The spectral resolution of RGB and NED combinations is 1.3m.

Figure 4-6: A portion of Pléiades Neo multispectral bands composites and panchromatic

4.3.2   Pléiades Neo Composites

In Figure 4-7, Pléiades Neo multispectral and pan-sharpen composites of 6-bands are shown. The spatial resolution of multispectral bands is 1.3m and pan-sharpened bands is 0.3m.

Figure 4-7: Pléiades Neo multispectral and pan-sharpened RGB composites

4.3.3   Pléiades Neo Composites with NDVI and LiDAR$_{CHM}$

Figure 4-8 represents Pléiades Neo band composites of multispectral and pan-sharpen with NDVI and LiDAR$_{CHM}$. These composites were prepared by adding NDVI and LiDAR$_{CHM}$ with 6-band

multispectral and pan-sharpen datasets. The main purpose of this was to prepare a better combination of bands for mangrove classification. The NDVI threshold values were set in the range from 0.30 to 0.85 for mangroves. The height values of LiDAR$_{CHM}$ was range from 0.5m to 12m. These values of height were selected based on assumption that mangroves minimum height is 0.5m and below that, there are potentially other species. Likewise, maximum height was assumed to 12m by visual observation on LiDAR$_{CHM}$ values for mangroves.
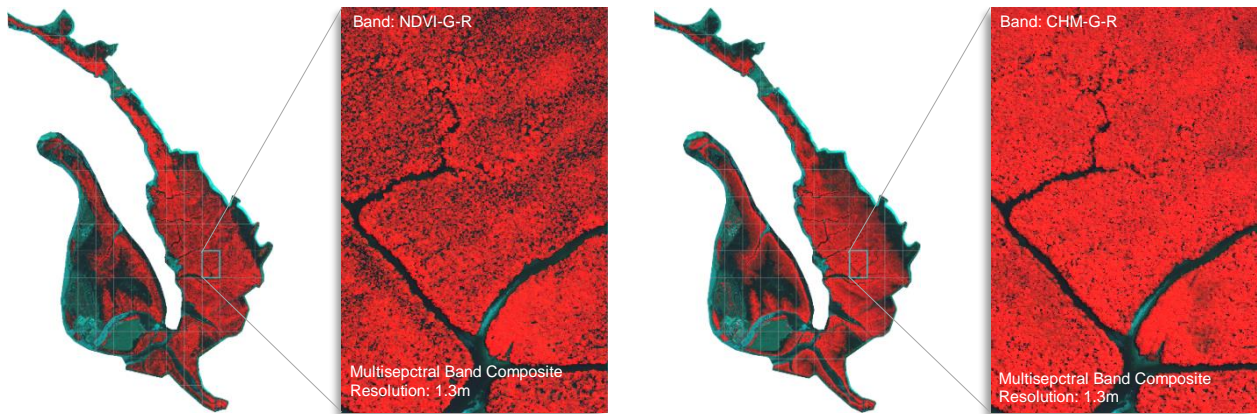
Figure 4-8: A portion of Pléiades Neo composites with NDVI and CHM

4.3.4 Pléiades Neo Classification

The classification work was accomplished to measure mangrove extent through supervised (random trees – RT) and unsupervised (ISO cluster) approaches. Overall, 4 classification of Pléiades Neo imagery were taken into account.

4.3.4.1 Pléiades Neo Classification (Random Trees – RT)

Firstly, RT classification (Figure 4-9) was performed on each 8-band stack of multispectral (1.3m) and pan-sharpen (0.3m) stack of Pléiades Neo. Both, Pléiades Neo$_{NDVI}$ and LiDAR$_{CHM}$ was combined together to improve supervised classification training samples and classification results.
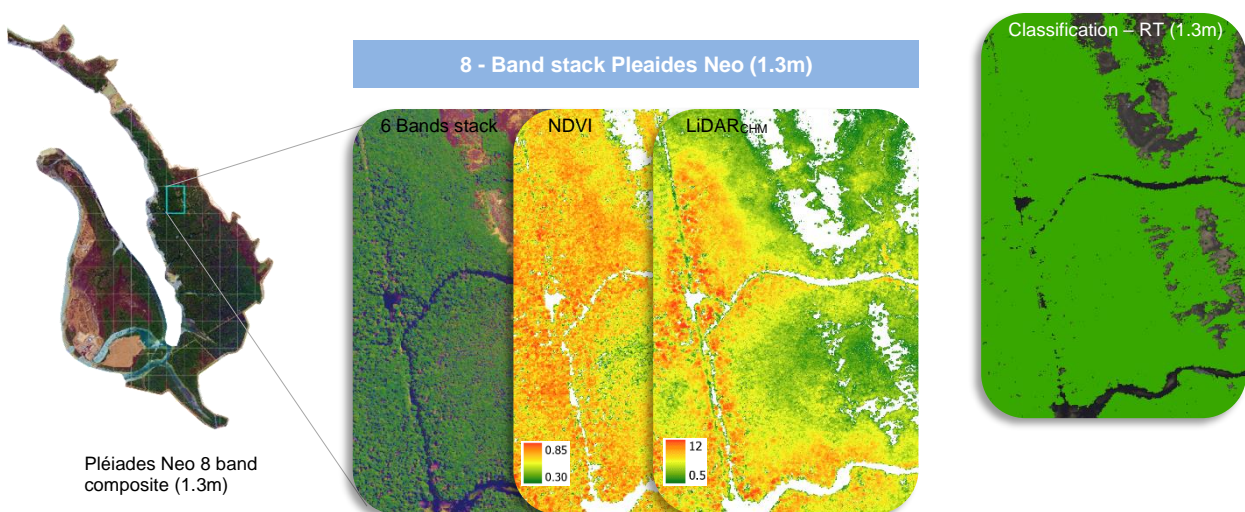
Figure 4-9: Random tree (RT) classification for Pléiades Neo

4.3.4.2 Pléiades Neo Classification (ISO Cluster)

In Figure 4-10 two ISO cluster classification results for Pléiades Neo stack of 8-band including NDVI and LiDAR$_{CHM}$ layers can be observed. Figure 4-10a represents ISO cluster classification on 8-band stack of Pléiades Neo at 0.3m resolution. Likewise, in Figure 4-10b represents ISO cluster classification at 1.3m resolution on 8-band stack of Pléiades Neo.

a)

Pan-sharpen 8 band composite (0.3m)   ISO Cluster classification on 8 band stack (0.3m)

b)

Pan-sharpen 8 band composite (1.3m)   ISO Cluster classification on 8 band stack (1.3m)
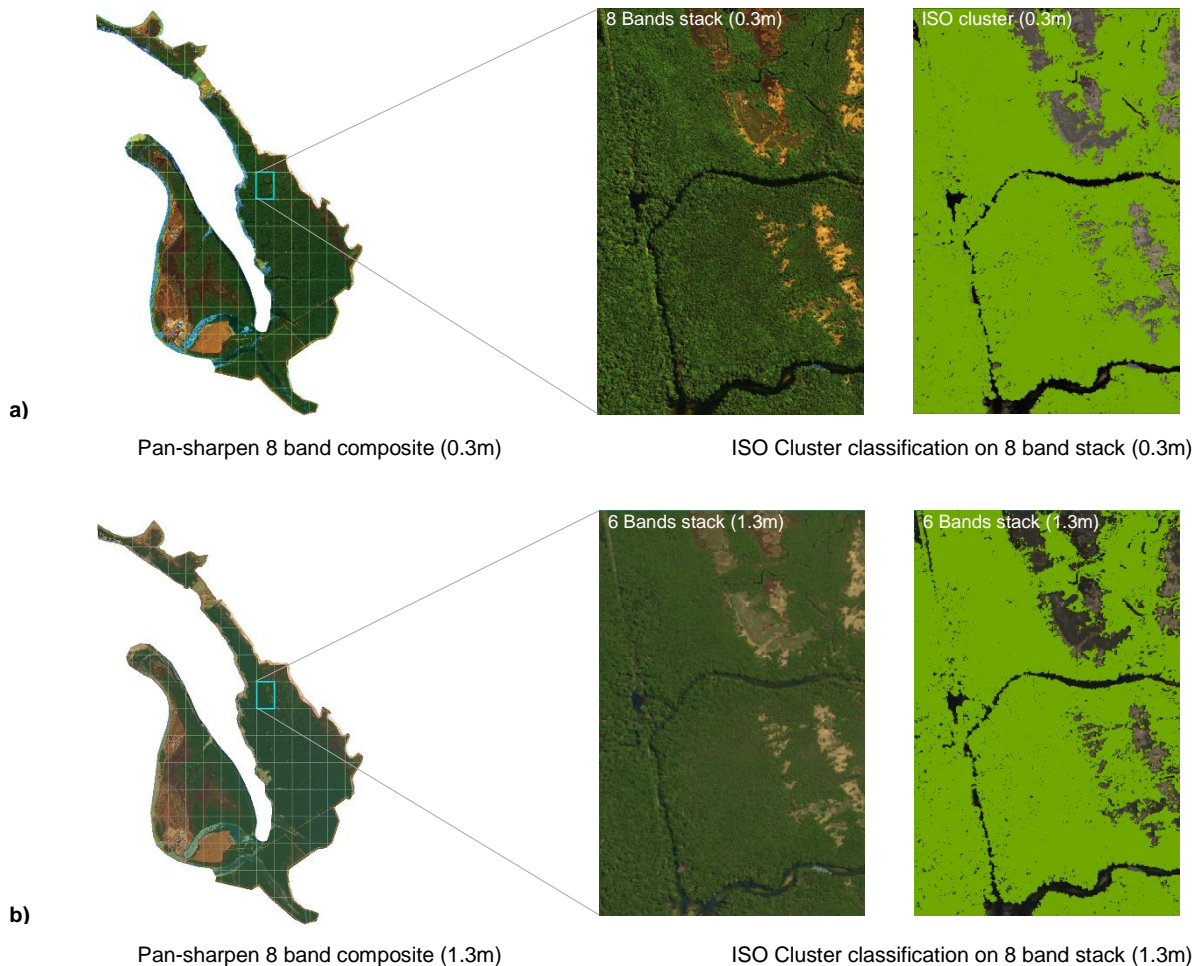
Figure 4-10: Pléiades Neo unsupervised classification

4.3.4.3 Ground Truth for Random Trees (RT) Classification

In Figure 4-11 the results are shown for Pléiades Neo classification for random trees – RT (0.3m). The accuracy results are given below. Figure 4-11a is showing the binary classification for mangrove and non-mangrove areas and in Figure 4-11b is showing 400 random points on google imagery of approximately of the same date for ground truth. Additionally, we have also used LiDAR based RGB imagery of 0.10m resolution in ground truth. From Table 4-2 it can be seen that the user accuracy is almost 89% for mangroves and procedural accuracy seems to be 99%. The value of Kappa test is 0.86 which is clear indicator of high accuracy of classification. Normally, this value ranges between 0 and 1.
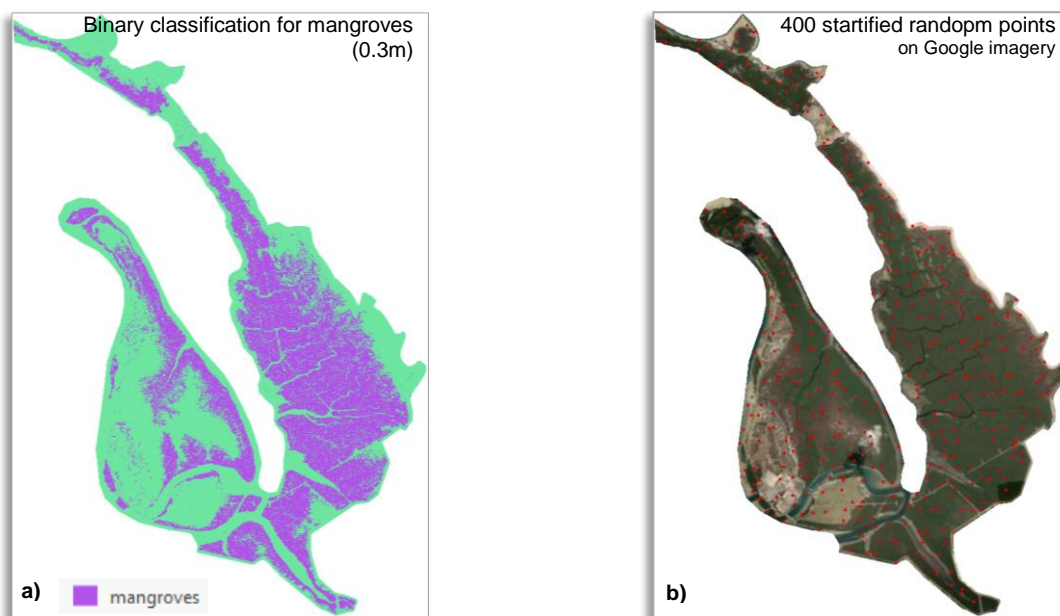
Figure 4-11: Pléiades Neo classification accuracy assessment

Table 4-2: Classification accuracy matrix

Class	Mangroves	Non-mangroves	Total	U accuracy	Kappa
Mangroves	208	24	232	0.89	0
Non-mangroves	2	166	168	0.98	0
Total	210	190	400	0	0
P Accuracy	0.99	0.87	0	0.93	0
Kappa	0	0	0	0	0.86

4.3.4.4 Mangrove Extent from Classification

The area of mangrove extent was calculated using two machine learning approaches (RT and ISO Cluster). In Table 4-3, the difference between the mangrove extent can be seen clearly. From supervised classification (RT) it seems to be approximately 13 km^2 and 15.78 km^2 from 8-bands Pléiades Neo (0.3m) and Pléiades Neo sharpen (1.3m) imagery respectively. On the other hand, from unsupervised classification (ISO Cluster) it appears to be 14.35 km^2 and 14.99 km^2 using 8-bands Pléiades Neo (0.3m) and Pléiades Neo sharpen (1.3m) respectively. Overall, all of the areas are close to each other approximately with the difference of 1-2 km^2. 3D view of the RT classification (0.3m) shown in Figure 4-12a and mangrove extent comparison is shown in bar graph in Figure 4-12b. (See Appendix A 1-5)

Table 4-3: St Kilda mangroves extent comparison summary

Data	Bands	Resolution	Method	Pixels	Area (km^2)
Pléiades Neo pan-sharpen	8	0.3m	RT	145410212	13.09

Pléiades Neo XS	8	1.3m	RT	9337202	15.78
Pléiades Neo pan-sharpen	8	0.3m	ISO Cluster	159476978	14.35
Pléiades Neo XS	8	1.3m	ISO Cluster	8871420	14.99

a) 3D view of mangroves classification (0.3m)
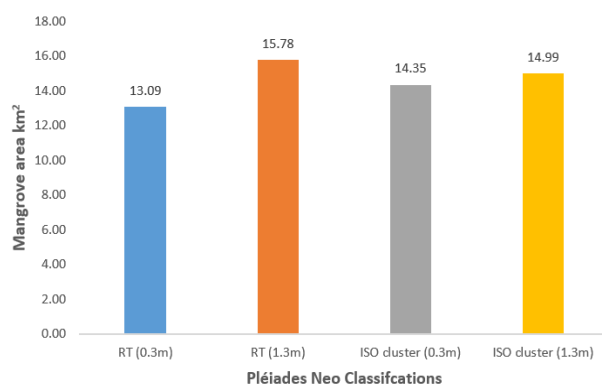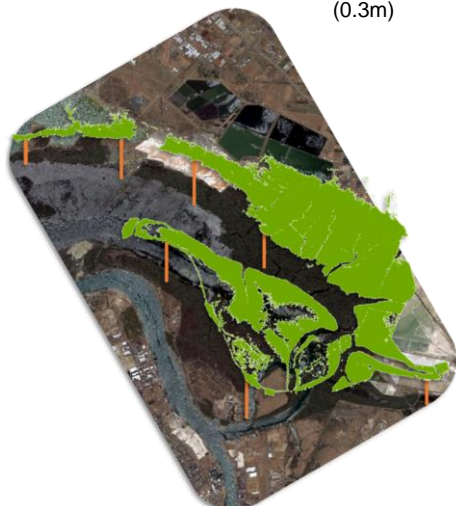
b) Bar graph showing areas calculated from classifications

Figure 4-12: Mangrove extents measured from two different classification

4.3.5 Pléiades Neo Vegetation Indices

Pléiades Neo NDVI (Figure 4-13) layers was calculated on 6-band multispectral imagery with a 1.3m resolution. Its values were ranged between 0.30 to 0.85 after applying threshold.

Figure 4-13: Pléiades Neo NDVI

4.3.6 Principal Component Analysis – PCA of Pléiades Neo

From the Table 4-4, it can be concluded that first two axis PC-1 and PC-2 are responsible for 98% of the total variance. Therefore, the rest of the component may be disregarded. The main purpose of the PC analysis was to reduce the dimensionality and complexity of the data to capture maximum information using axes. In the Table 4-5, from eigenvalues and eigenvectors matrix, it can be seen that PC-2 contains all negative values except one, which is seems to be indicator of

better texture information in that axis and potential to have high reflectance of vegetation. In a Figure 4-14, two components (PC-1 & PC-2) of PCA are shown.
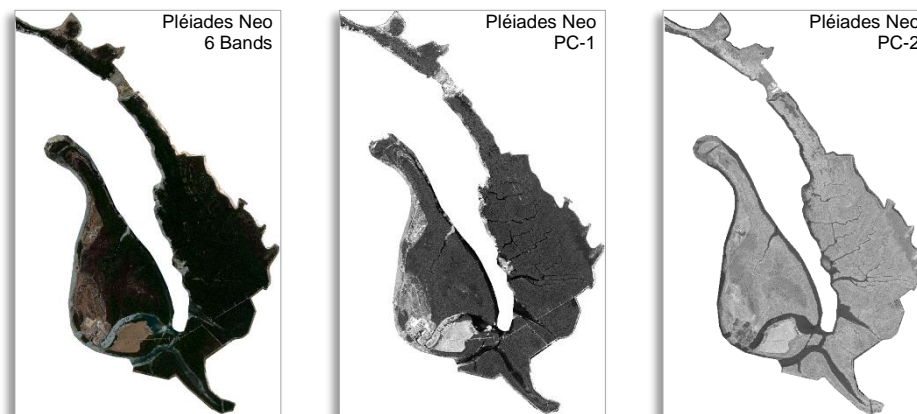
Figure 4-14: Pléiades Neo principal component analysis

Table 4-4: Summary of eigenvalues and percentages of Pléiades Neo PCA

PC Layer	Eigenvalues	Eigenvalues(%)	Accumulative
PC1	5066531.34291	88.0769	88.0769
PC2	607595.07831	10.5625	98.6394
PC3	52339.58385	0.9099	99.5493
PC4	12959.28674	0.2253	99.7746
PC5	8794.66216	0.1529	99.9275
PC6	4172.70509	0.0725	100.0000

Table 4-5: Summary for eigenvalues for each PC in Pléiades Neo PCA

PC Layer	PC1	PC2	PC3	PC4	PC5	PC6
PC1	0.45400	-0.22839	-0.69746	-0.00037	-0.49225	0.11386
PC2	0.38653	-0.34701	0.02504	-0.53352	0.56457	0.35520
PC3	0.32552	-0.36771	0.37701	-0.22636	-0.22886	-0.71629
PC4	0.45857	0.71478	0.28905	-0.29570	-0.27740	0.17568
PC5	0.49719	0.25503	-0.18419	0.51822	0.52379	-0.33305
PC6	0.28467	-0.34096	0.50330	0.55509	-0.18779	0.45389

4.3.7 Regression Models from Pléiades Neo

4.3.7.1 NDVI Based Model

From the Figure 4-15, it can be seen that in a linear relationship R^2 value for NDVI and field$_{Biomass}$ is 0.40. In contrast, in exponential model it seems to be 0.48 which appears to be higher than the linear relationship. Therefore, NDVI based regression model can only explain 40% and 48% of the AGB.
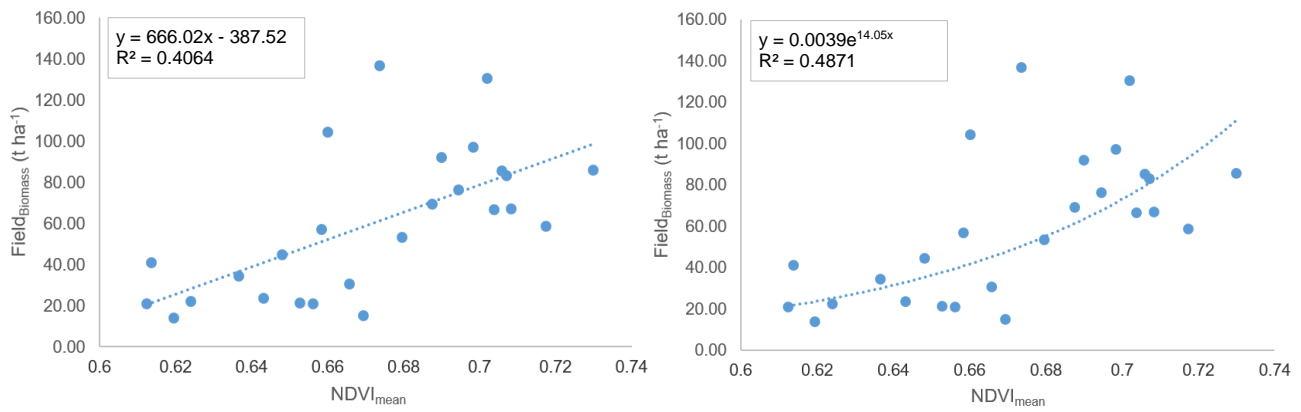
Figure 4-15: Regression models Pléiades Neo NDVI; Left (Linear Regression); Right (Exponential Regression

4.3.7.2 PCA Based Model

Figure 4-16a, represents the results of PC-1 for Pléiades Neo. PC-1$_{mean}$ has the R^2 value of 0.07 and PC-1$_{PCT90}$ has the R^2 value of 0.16. Likewise, Figure 4-16b shows the relationship between field$_{Biomass}$ and PC-2$_{mean}$. In that analysis, R^2 value from PC-2$_{mean}$ is 0.12 and PC-2$_{PCT90}$ is 0.26. Overall, this relationship seems to be weaker and can explain only 26% of the biomass variance.

a) Pléiades Neo PC-1
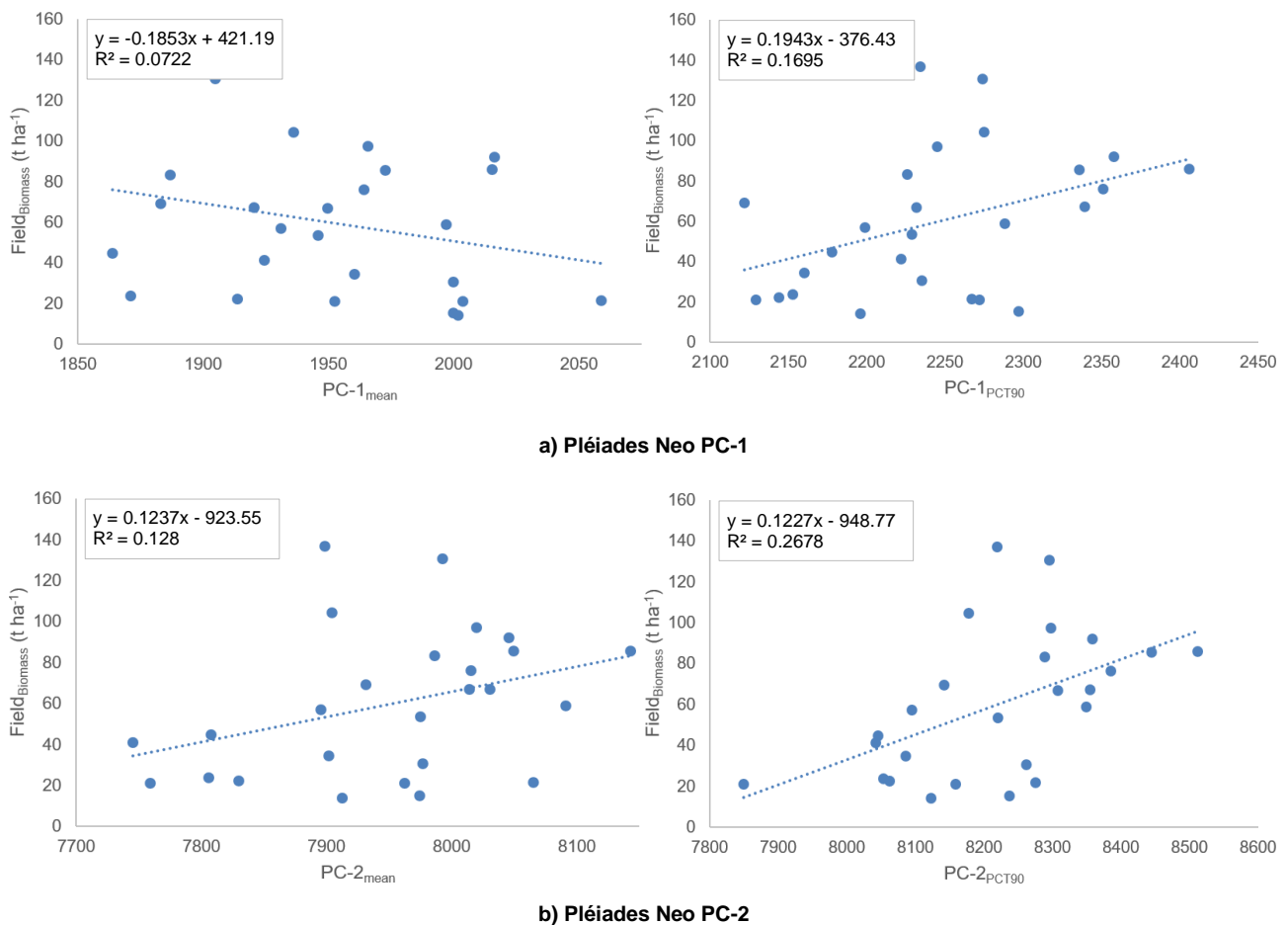
b) Pléiades Neo PC-2

Figure 4-16: Correlation scatterplot between PCA (PC-1, PC-2) and field biomass

4.3.8 Regression Models Summary - Pléiades Neo

Table 4-6 represents all of the models derived from Pléiades Neo satellite. Here, it can be seen that the highest value of (R^2=0.48) obtained from Pléiades Neo$_{NDVI}$ which is exponential and (R^2=0.40) is from the linear regression model. The other values derived from PCA and NDVIre seems to be pretty low.

Table 4-6: Regression models from Pléiades Neo

Model	R^2	Equation	Relation
RM-PLNeo$_{NDVI}$	0.40 0.48	$y = 666.02x - 387.52$ $y = 0.0039e^{14.05x}$	Positive linear Exponential
RM-PLNeo$_{PC-1\ PCT90}$	0.16	$y = 0.1943x - 376.43$	Positive linear
RM-PLNeo$_{PC-2\ PCT90}$	0.27	$y = 0.122x - 948.77$	Positive linear
RM-PLNeo$_{NDVIre}$	0.06	$y = 519.80x - 56.02$	Positive linear

4.3.9 Sentinel-2 Dataset Pre-processing

Figure 4-17 represents various combination of Sentinel-2 pre-processing such as natural colour (4 3 2), Infrared colour (8 4 3) and shortwave-infrared (12 8A 4). In all these combinations, mangroves reflectance variations can be seen clearly.
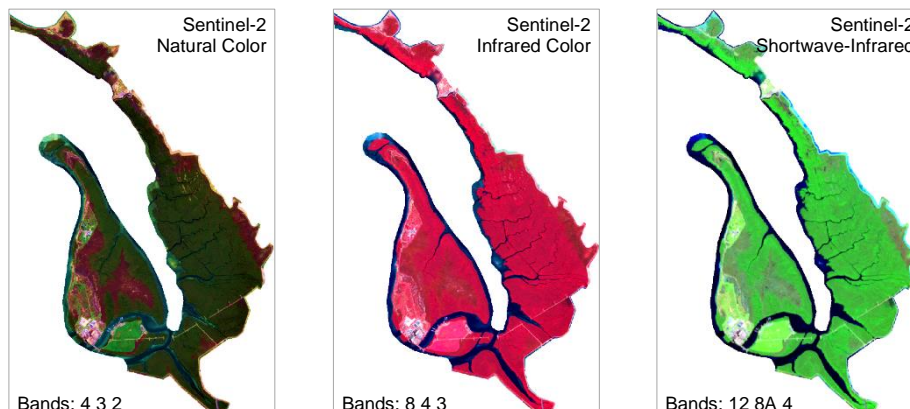
Figure 4-17: Sentinel-2 imageries

4.3.10 Sentinel-2 Vegetation Indices

From Sentinel-2 data, mainly four (NDVI, NDVIre, MVI and CMRI) indices were computed to calculate AGB estimation. In Figure 4-18 and Figure 4-19, reflectance response of these indices are shown. In addition to that, two additional indices (NDMI and NDWI2) were calculated to compute CMRI for AGB estimation (Figure 4-19). Finally, regression analysis was completed using these four vegetation indices vs field$_{Biomass}$. Hence, it can be seen that the highest value of R^2 achieved
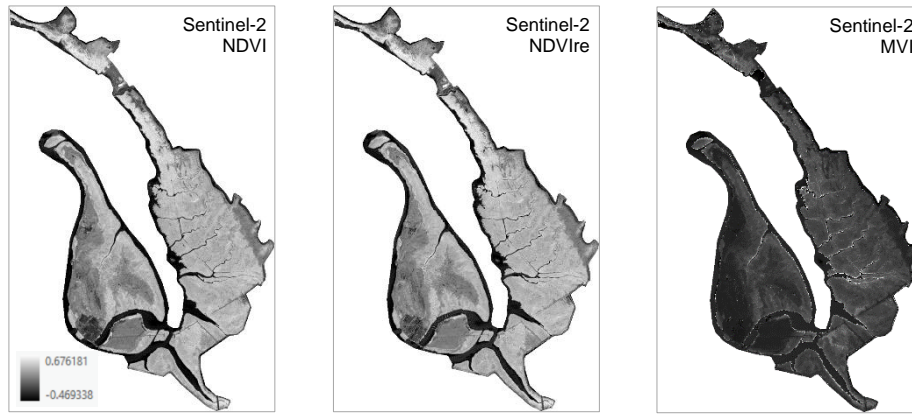
Figure 4-18: Sentinel-2 vegetation indices (NDVI, NDVIre, MVI)
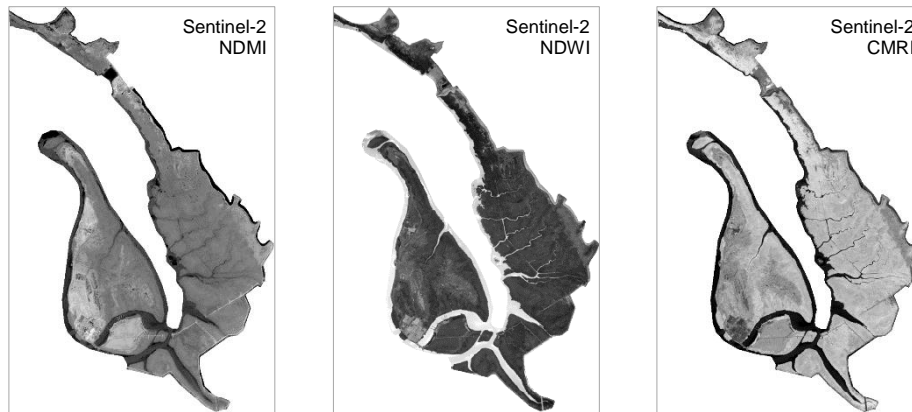
Figure 4-19: Calculation of Sentinel-2 CMRI from NDMI and NDWI

through MVI indices which is 0.48 and relationship is positively correlated. The second highest value of R^2 is 0.40 is derived from NDVIre. Surprisingly, NDVI just gave the R^2 value of 0.24. Moreover, lowest value is 0.19 and the relationship is exponential. All of the regression equations for each category is displayed in Figure 4-20 along with their R^2 values.
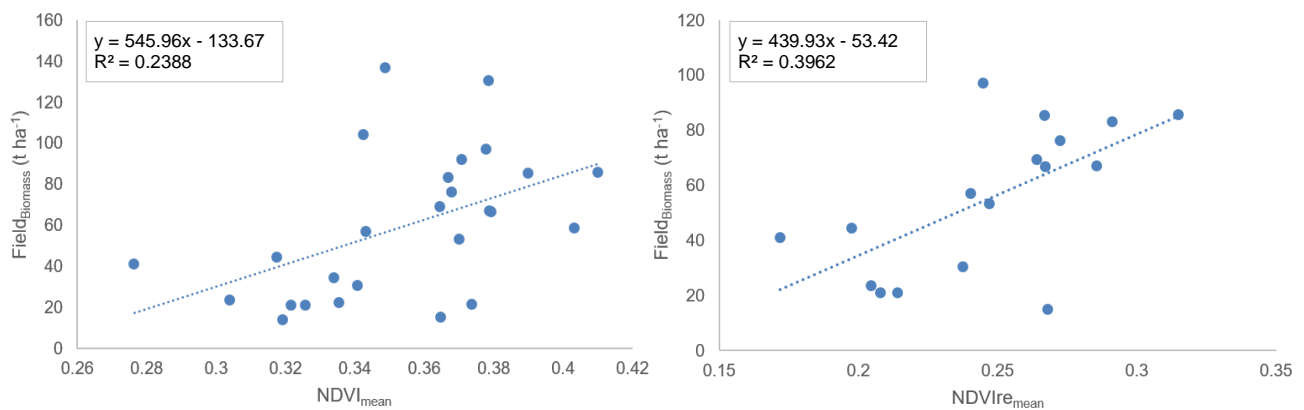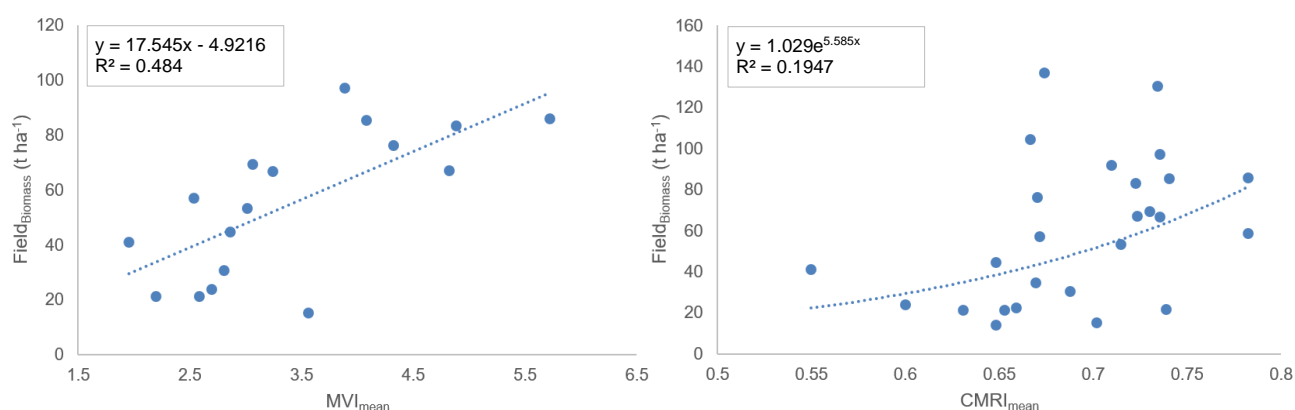
Figure 4-20: Regression models Sentinel-2 vegetation index (VI)

4.3.11 PCA Analysis – Sentinel-2

In Figure 4-21, the principal component analysis (PCA) is shown for first three axis. However, it was derived for 12 Sentinel-2 bands to explore the data dimensionality. Form the Table 4-7, it is obvious that PC-1 and PC-2 components contains 97% of the information. Therefore, PC-1 and PC-2 were used in regression analysis.
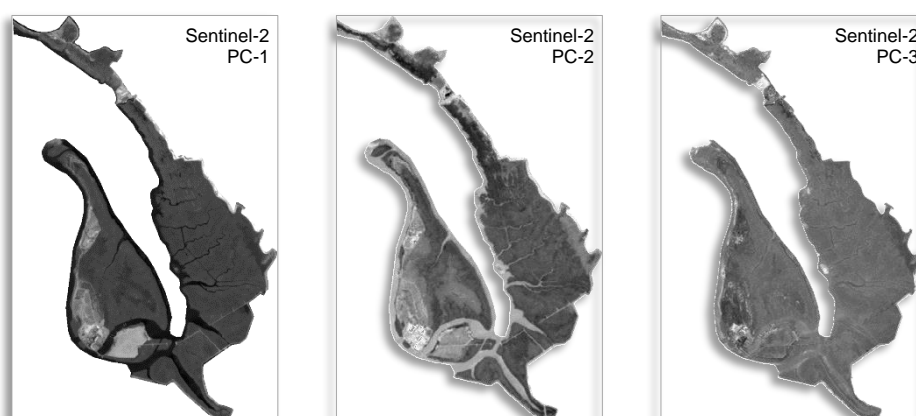
Figure 4-21: Principal component analysis of Sentinel-2

Table 4-7: Summary of eigenvalues and percentages of Sentinel-2 PCA

PC Layer	Eigenvalues	Eigenvalues(%)	Accumulative
PC1	14527043.75	93.5282	93.52
PC2	647826.96	4.1708	97.69
PC3	228504.26	1.4712	99.17
PC4	46812.72	0.3014	99.47
PC5	31868.95	0.2052	99.67
PC6	19094.61	0.1229	99.79
PC7	11109.54	0.0715	99.87
PC8	8998.91	0.0579	99.92
PC9	4032.14	0.0260	99.95

PC10	2684.57	0.0173	99.97
PC11	2492.87	0.0160	99.98
PC12	1790.00	0.0115	100.00

From PCA model, it can be seen that PC-2 has a higher value of 0.18 and also it is negatively correlated. However, PC-1 value was very low which was approximately 0.008 and seemed very weak positive relationship between PC-1 and fieldB_{iomass}. The PC-1 and PC-2 results are shown in Figure 4-22.
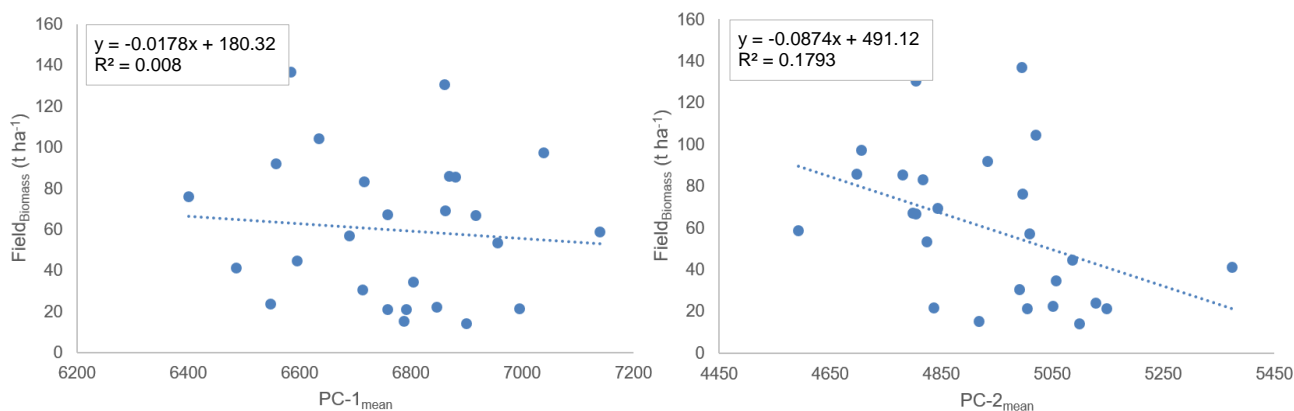
Figure 4-22: Sentinel-2 regression models from PCA; Left (Positive linear model); Right (Negative linear model)

4.3.12 Regression Models – Sentinel-2

Table 4-8 represents regression models derived from Sentinel-2 data. The highest value of R^2 achieved from S2$_{MVI}$ model, which is presumably reasonable to explain 48% of the biomass variability and positively linear. The second highest value of the regression model is from S2$_{NDVIre}$ which is (R^2=0.40) and able to explain 40% of the biomass variant. The R^2 values from other remote sensing variables seems to be low.

Table 4-8: Regression models from Sentinel-2

Model	R^2	Equation	Relation
RM-S2$_{NDVI}$	0.21	$y = 600x - 154$	Positive linear
RM-S2$_{NDVIre}$	0.40	$y = 439.93x - 53.42$	Positive linear
RM-S2$_{MVI}$	0.48	$y = 17.54x - 4.92$	Positive linear
RM-S2$_{PC-2}$	0.18	$y = -0.08x + 491$	Negative linear
RM-S2$_{CMRI}$	0.17	$y = 271.56x - 128.10$	Positive linear

4.3.13 Regression Models from Optical Data

In a Table 4-9, a summary of best regression models is shown extracted from optical data. Here, it can be seen that the highest value of the R^2 obtained from Pléiades Neo$_{NDVI}$ regression model which is approximately 0.40. In contrast the value of (R^2=0.48) is higher in Sentinel-2 MVI index. Another, highest value of (R^2=0.40) obtained from Sentinel-2 using NDVIre.

Table 4-9: Regression models from optical data

Model	R²	Model	R²
RM-PLNeo$_{NDVI}$	0.40	RM-S2$_{NDVI}$	0.21
RM-PLNeo$_{NDVIre}$	0.06	RM-S2$_{NDVIre}$	0.40
RM-PLNeo$_{PC-2}$	0.27	RM-S2$_{MVI}$	0.48
		RM-S2$_{CMRI}$	0.17
		RM-S2$_{PC-2}$	0.18

4.3.14 Optimal Biomass Model from Optical

The best optical regression model, between Sentinel-2$_{MVI}$ and field$_{Biomass}$, derived with a R² value of 0.48. This coefficient of determination R² seems to be moderate but good enough to explain at least half of the biomass variant.

$$y = 17.54x - 4.92$$ **Equation: 4-2**

The biomass layer was computed using Equation 4-2 by replacing the explanatory variable *(x)* with *(MVI)* and the output is represented in Figure 4-23c. The predicted biomass values from Sentinel-2$_{MVI}$ were ranged between 0.5 to 170 t ha^{-1} with a mean value of 54 t ha^{-1}. The best optical model produced a total biomass of 69,024 tons. In a whisker plot (Figure 4-23b), quartile ranges Q1=61.81, Q2=50.92, Q3=42.52 are shown extracted from optical biomass model. (See Appendix A 1-2)

a)

b)   c)
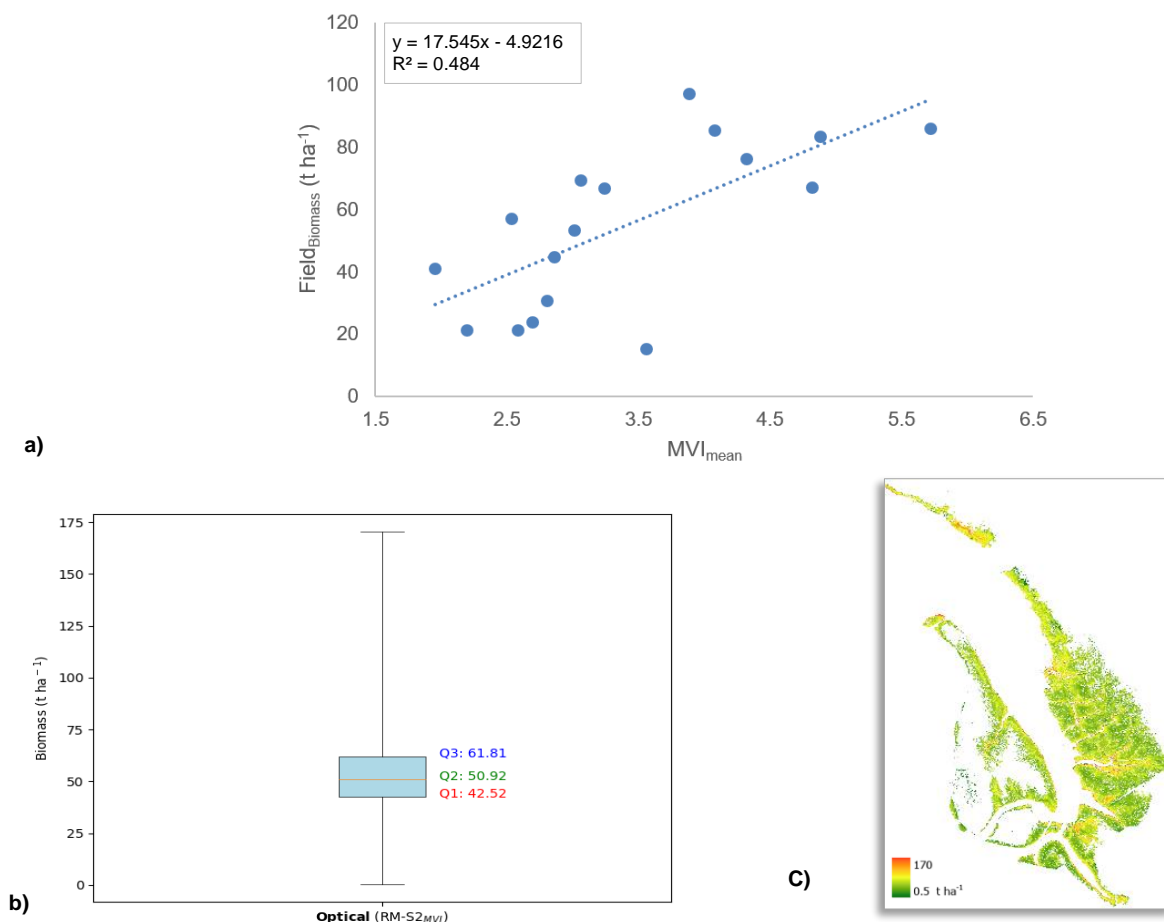
Figure 4-23: Biomass extraction from best regression model Sentinel-2$_{MVI}$

4.4 Spatial Analysis Derived from Optical Data

4.4.1 Distance to Water Analysis

This analysis explored the distance to water for each mangrove height category such as low, medium and high. The main purpose of this analysis was to identify if a relationship existed between distance to marine water and mangrove biomass existed. Figure 4-24 is showing the distance layer for mangroves from marine creek water. The Figure 4-24a is showing the distance of low (0.5m to 3m) height mangroves from creeks. Figure 4-24b and Figure 4-24c are showing the distances of medium (3m-6m) and the tallest (6m-12m) mangroves from the water creeks respectively. From this analysis, it was concluded that, high biomass of mangroves are along the creeks and of low biomass is away from the creeks.
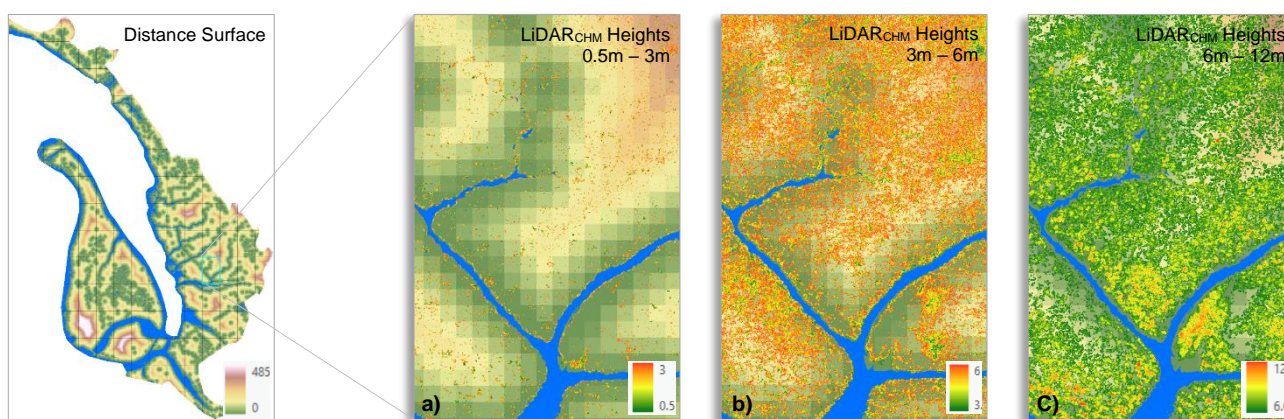
Figure 4-24: Distance to marine water analysis

4.4.2 Astronomical Tide Analysis

This comparison in Figure 4-25 shows astronomical tide levels of mangroves at 0.3m and 1m water level. This analysis describes water distribution scenarios in mangroves at various heights. This analysis was performed on DEM by extracting surface heights of 0.3m and 1m. In Figure 4-25a mangroves of low (0.5m-3m) and maximum heights (6m-12m) are displayed at 0.3m tide level. Likewise, in Figure 4-25b, mangrove distribution is displayed at 1m water level. This analysis showed how astronomical tide levels influences the mangrove distribution.
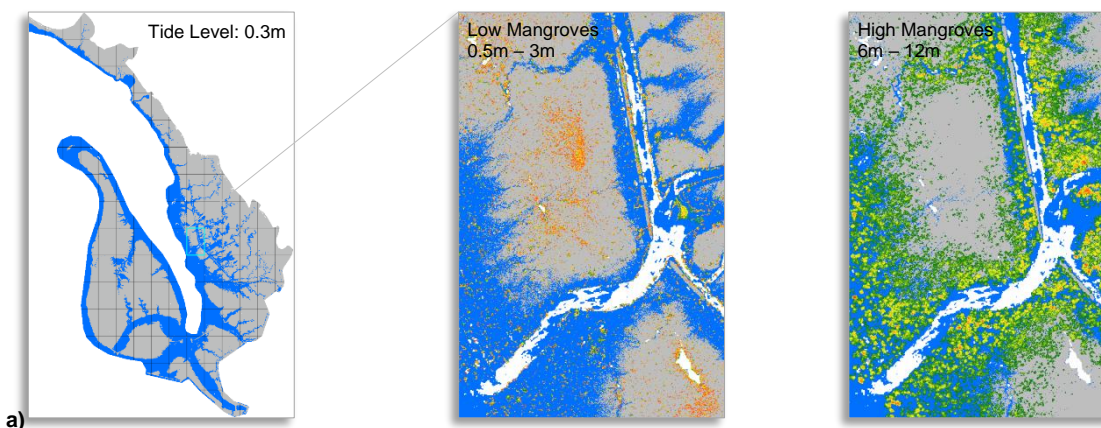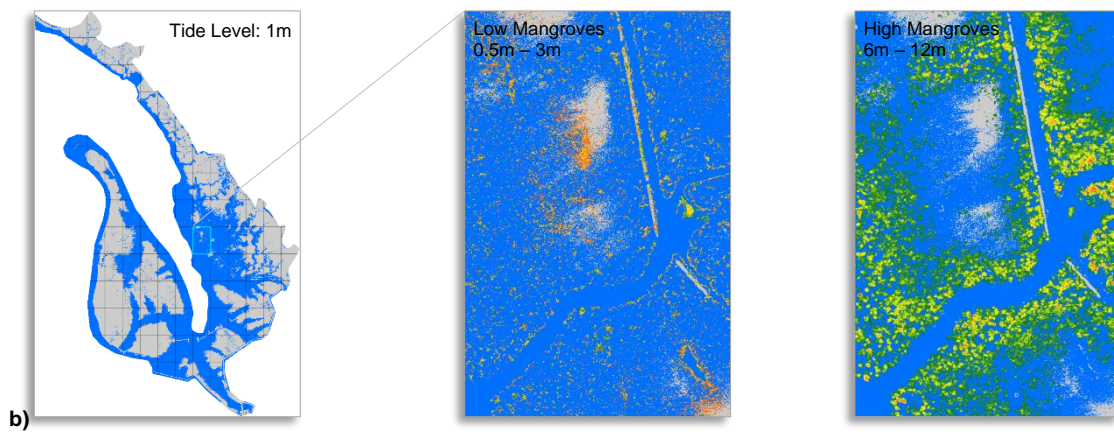
Figure 4-25: Astronomical tide analysis for various mangroves heights

4.4.3 Mangrove Forest Floor analysis

This analysis showed mangrove biomass distribution along the salt water channels, small catchments and on the ridges. This analysis was performed on digital elevation model (DEM) derived from LiDAR. Those ridges and under mangrove forest was not visible in the optical and not in the RADAR imagery. In Figure 4-26 forest floor beneath the mangroves can be seen clearly. The topography beneath the forest floor demonstrated the availability of nutrients and salt water which are very much important in AGB growth.
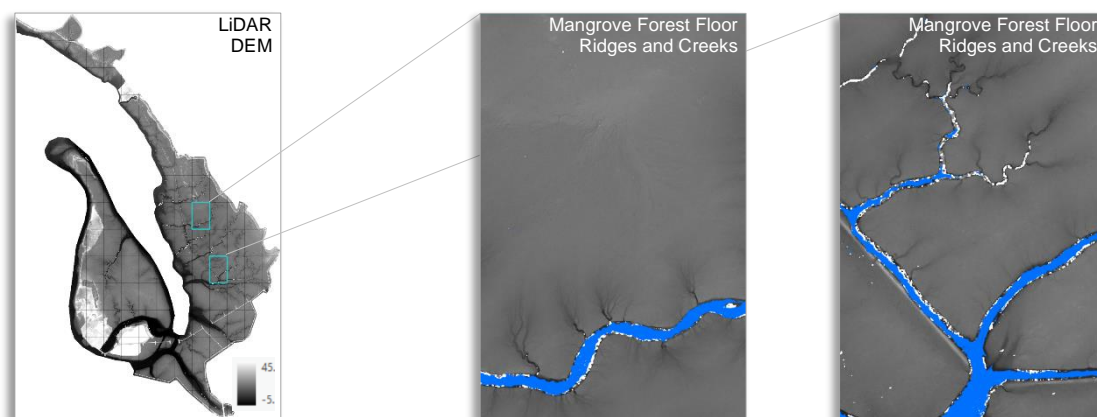
Figure 4-26: Forest floor under mangroves

4.4.4 NDVI Comparison Between Pléiades Neo and Sentinel-2

Quartile visual comparison of two NDVIs (Pléiades Neo & Sentinel-2) showed a high correlation visually. However, statistical regression (R^2=0.25) proved that the relationship is not statistically significant with weak positive relationship. Upon checking the wavelength and spectral sensitivity of both satellites, Pléiades Neo wavelength was found to be slightly varied for red and infrared regions as compared with Sentinel-2. Moreover, spatial resolution was also higher for Pléiades Neo. While doing this analysis, it was identified that NDVI values seem to be consistently high in

the Northern part and likely to be high along the salt creeks (Figure 4-27). In contrast, NDVI values were lower near salt marshes areas, as mangroves seems to be young and lower in heights.
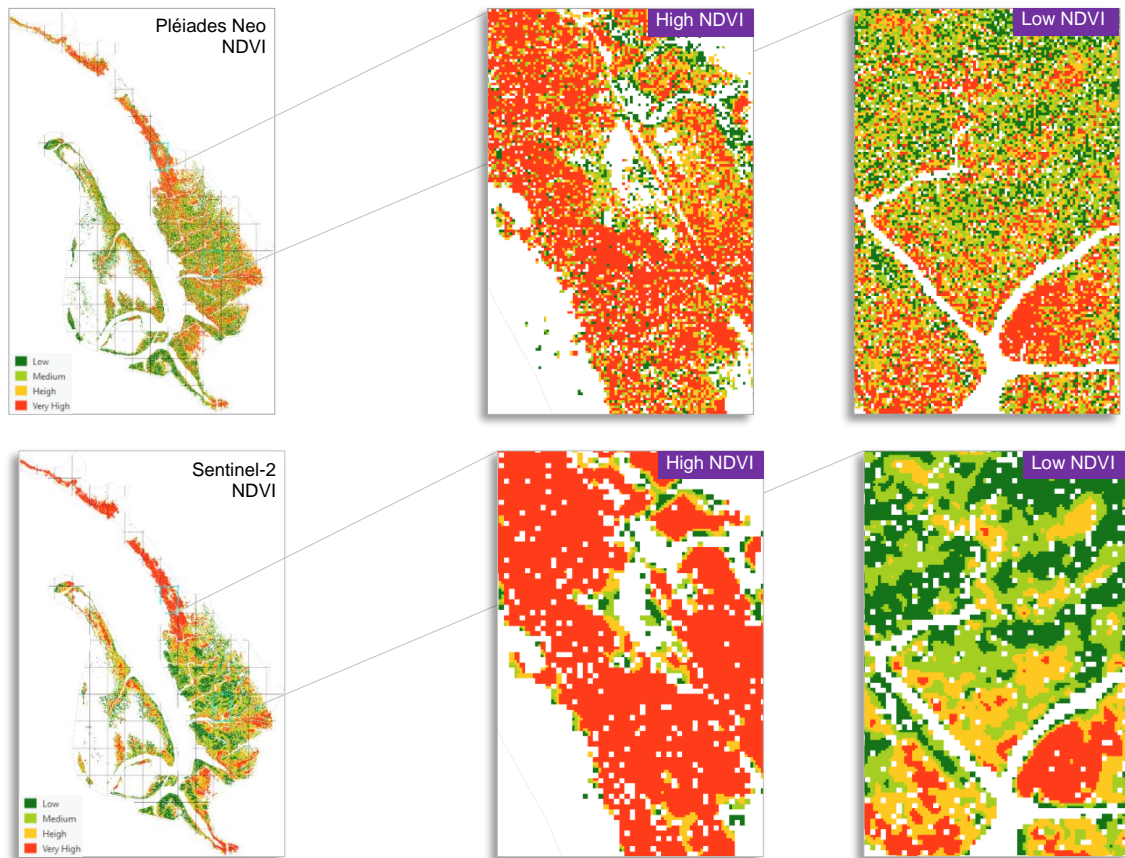
Figure 4-27: NDVI comparison between Pléiades Neo and Sentinel-2 5m

4.5 Biomass Estimation from RADAR Data

4.5.1 Pre-processing for ALOS-1 PALSAR

In a Figure, 4-28 ALOS-1 PALSAR HH and HV polarisations are displayed. This is a dual pole satellite and can provide single or dual polarisations at a certain time. This imagery was
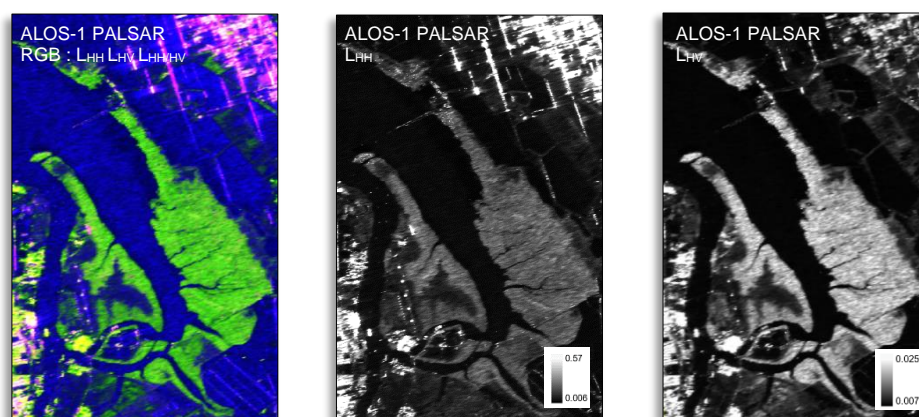
Figure 4-28: ALOS-1 PALSAR pre-processing

calibrated, de-speckled and geometrical corrected at 14m resolution. In Figure 4-29 mangrove and water profiles are shown in decibel (dB). The average values for mangroves in HH backscatter was -11 and in HV backscatter it was -17 in image profile.
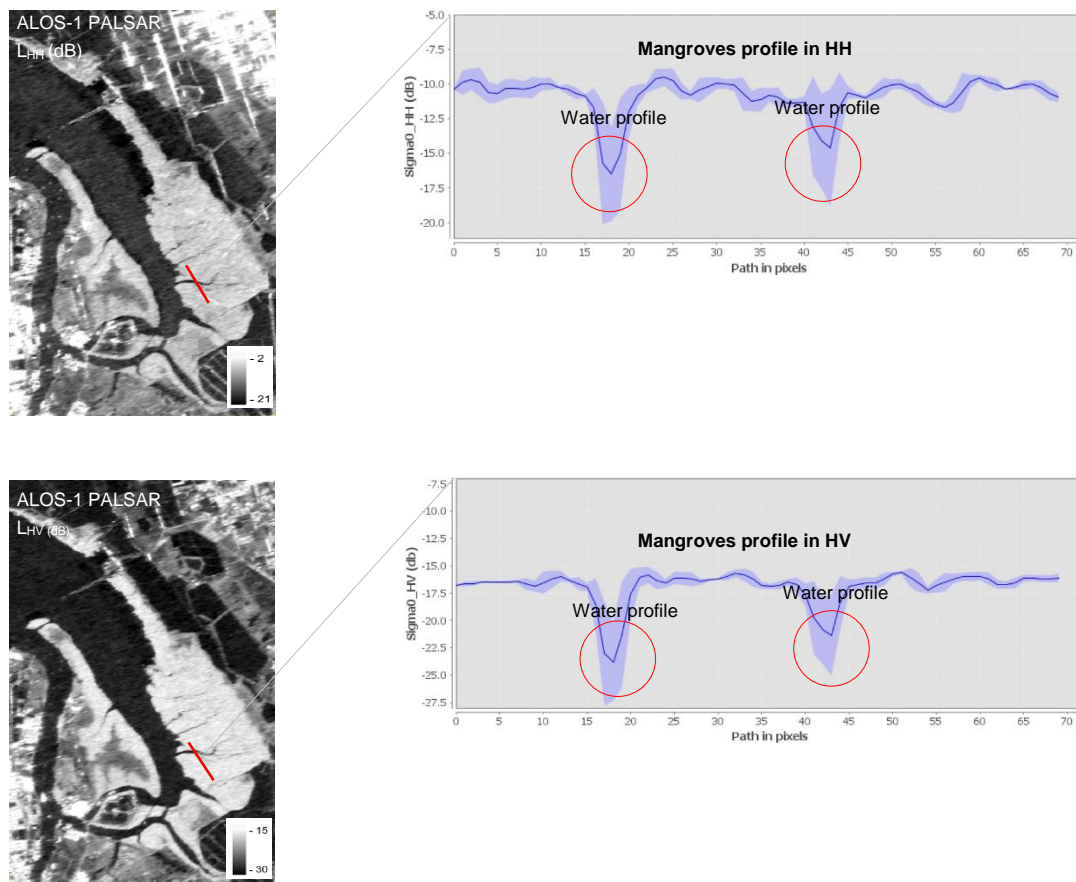
Figure 4-29: ALOS-1 PALSAR profile plots for HH and HV backscatters

4.5.2 PCA Analysis – ALOS-1 PALSAR

PCA was computed for two polarisation (HH and HV) of ALOS-1 PALSAR. The outcome of two components is displayed in Figure 4-30. Surprisingly, R^2 value of PC-2 component was 0.27 against field$_{Biomass}$.
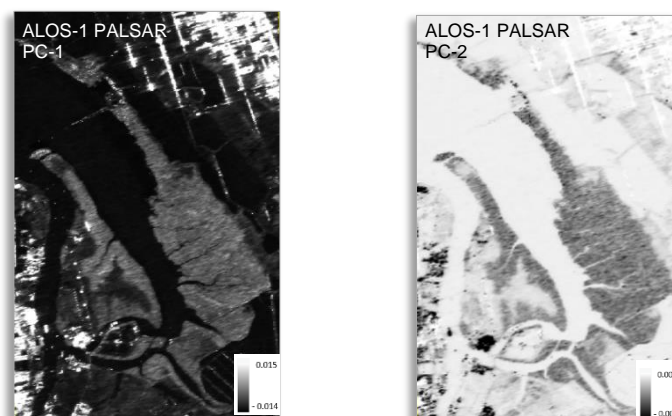
Figure 4-30: ALOS-1 PALSAR PCA components

4.5.3 GLCM Matrix – ALOS-1 PALSAR

GLCM was calculated for ALOS-1 PALSAR on intensity values. From a GLCM matrix, higher correlation values were found only for GLCM mean, variance and correlation. They are displayed in Figure 4-31.
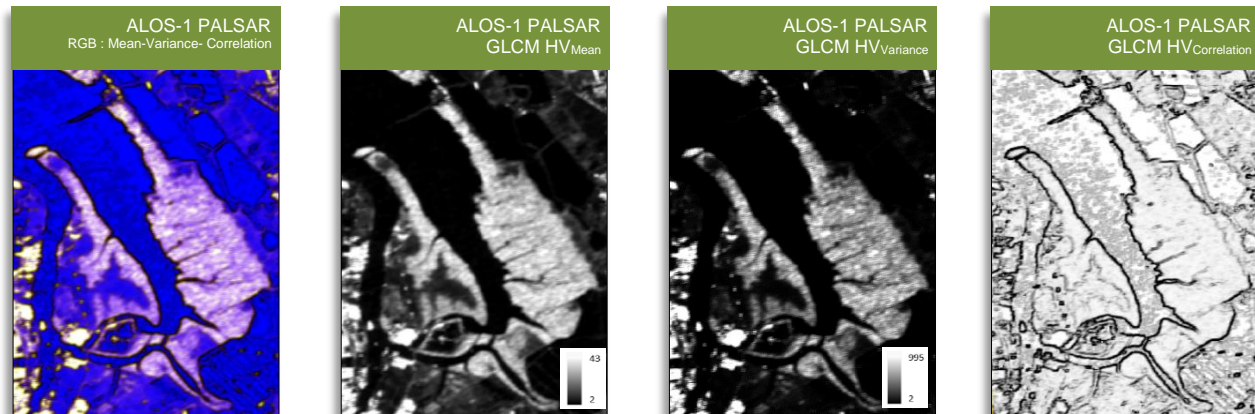
Figure 4-31: ALOS-1 PALSAR GLCM calculations

4.5.4 Regression Models – ALOS-1 PALSAR

In Table 4-10, regression models are shown derived from ALOS-1 PALSAR backscatter values, PCA, GLCM and RVI index. Here, it can be seen that PC-2 model seems to be higher in R^2 but it is exponential. In contrast, other three models (HV, GLCM and RVI) are seems to be linear models. The scatterplots for ALOS-1 PALSAR are given in Appendix D 1-1.

Table 4-10: Regression models from ALOS-1 PALSAR

Model	R^2	Equations	Relation
RM-ALOS1$_{HV}$	0.18	$y = 0.03516x - 19.56$	Positive linear
RM-ALOS1$_{PC-2}$	0.27	$y = -9.1439e^{-5x} - 0.0070$	Exponential
RM-ALOS1$_{GLCM-HVmean}$	0.23	$y = 0.137587x + 26.719$	Positive linear
RM-ALOS1$_{RVI}$	0.29	$y = 0.0027x + 0.563$	Positive linear

4.5.5 Pre-processing for ALOS-2 PALSAR

In Figure 4-32, all four polarisation are displayed along with their dB ranges. The final output resolution of this data was 4m after pre-processing. Moreover, statistical regression was computed between backscatter coefficients (HH, HV, VH & VV) against field$_{Biomass}$. Additionally, R^2 values were noted and the value of (R^2=0.14) for VH component was among the highest. This showed that L$_{VH}$ has the potential to explain only 14% of the biomass variant.
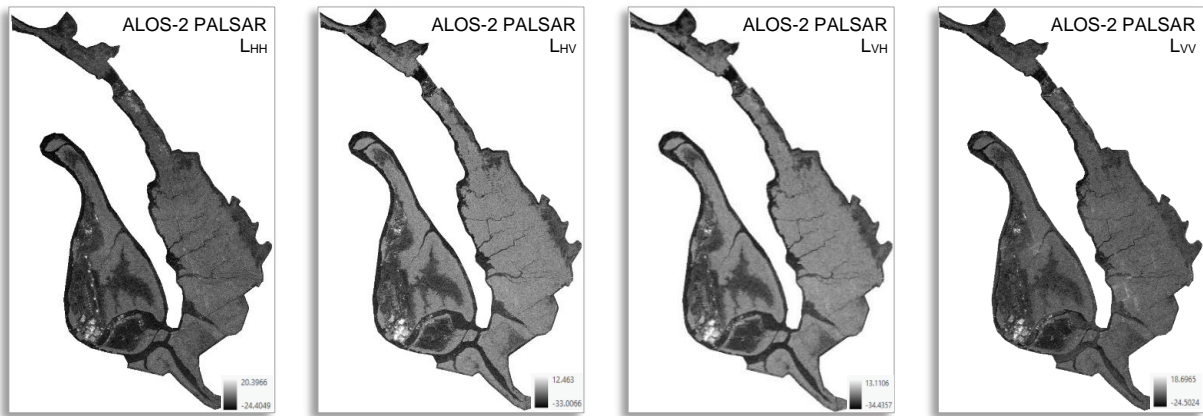
Figure 4-32: ALOS-2 PALSAR polarisations

In a Figure 4-33, mangroves enlargements are displayed ALOS-2 PALSAR to see the textural variations of mangroves in four different polarisations.
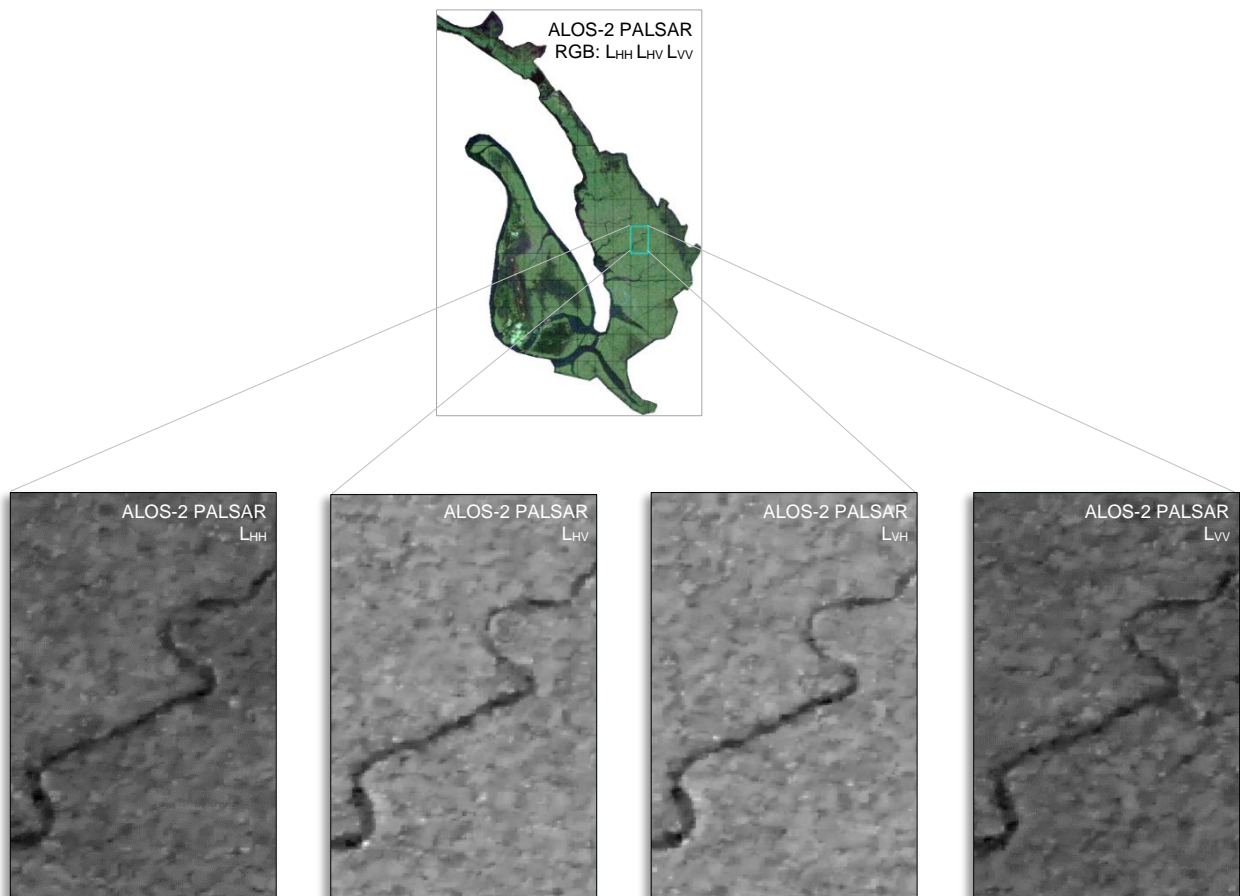
Figure 4-33: Textural variations in mangroves different polarisations

4.5.6 RADAR Vegetation Indices – ALOS-2 PALSAR

Figure 4-34a represents the radar vegetation index (RVI) for mangroves. It is a ratio of cross-polarised and like-polarised polarisations. It very similar to NDVI but in RADAR data it uses the backscatter. The output of RVI raster varied between 0 and 1. Here, 1 represented the dense and healthy forest conditions whereas 0 demonstrated sparse and low level forest conditions. Later, this index was used to calculate AGB using regression and R^2 value was 0.09.

Additionally, two more vegetation indices were calculated such as RFDI and CSI indices to see the forest degradation and structure conditions. Figure 4-34b, represents the RFDI values ranges between 0 to 1. In this case, dense forest is represented by 1 while degraded forest values lies between 0.4-0.6. Additionally, CSI results in the range of -1 to +1 are shown in Figure 4-34c. A value of +1 represented the mangrove's vertical structure, while a value of -1 showed the dominance of horizontal structure in the canopy. Later two indices were not used in AGB calculation directly, however, they were important to understand the mangrove distribution and degradation.
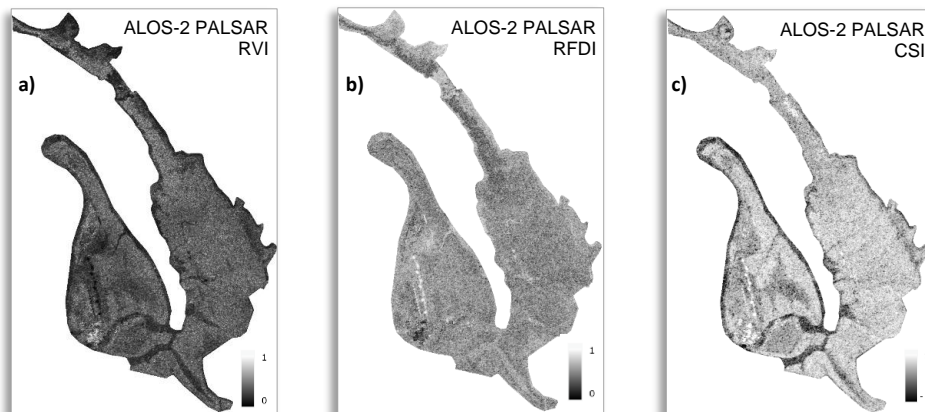
Figure 4-34: ALOS-2 PALSAR vegetation indices

4.5.7 PCA Analysis – ALOS-2 PALSAR

From the PCA composition text file, it can be observed that most of the information was captured along the axis-1 and axis-2, which is 84% and 10% respectively. In axis-4, it is just 1.23%. Therefore, axis-4 was not useful and dropped in further analysis. Therefore, the first two axis captured over 94% of the data values, which seems to be very helpful for estimating AGB. The value of R^2, between PC-2 and field$_{Biomass,}$ was 0.09 which seems to be pretty low for biomass calculation. Both of the PCA are shown in Figure 4-35 and percentage of eigenvalues for each component is given in Table 4-11.
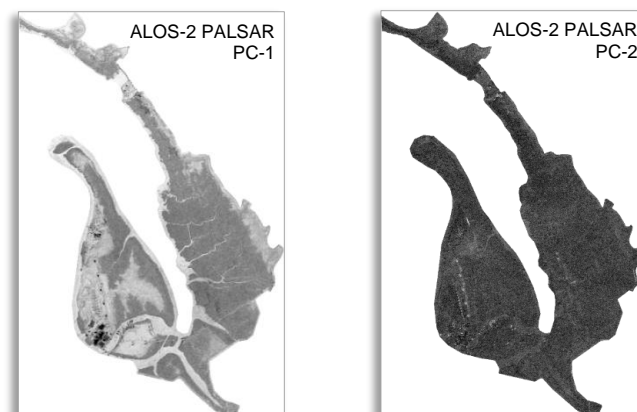
Figure 4-35: ALOS-2 PALSAR PCA components

Table 4-11: Summary of eigenvalues and percentages of ALOS-2 PALSAR

PC Layer	Eigenvalues	Eigenvalues (%)	Accumulative
PC1	55.59395	84.8721	84.8721
PC2	6.91136	10.5512	95.4232
PC3	2.18674	3.3384	98.7616
PC4	0.81118	1.2384	100

4.5.8 GLCM Matrix – ALOS-2 PALSAR

The grey level co-occurrence matrix (GLCM) was computed to investigate the backscatter characteristics based on specific relationship with in the image. The GLCM matrix was primarily divided into three groups; statistics, orderliness and contrast groups as shown in Figure 4-36. Each of these groups was further divided into three sub-categories; contrast group (*Contrast, Dissimilarity & Homogeneity*) orderliness (*ASM, Entropy & Max*), and statistics group (*mean, variance & correlation*). To calculate AGB, all of the groups were analysed and only statistical group mean provided the little better value of (R^2=0.04) but even though it was not statically significant to compute AGB.
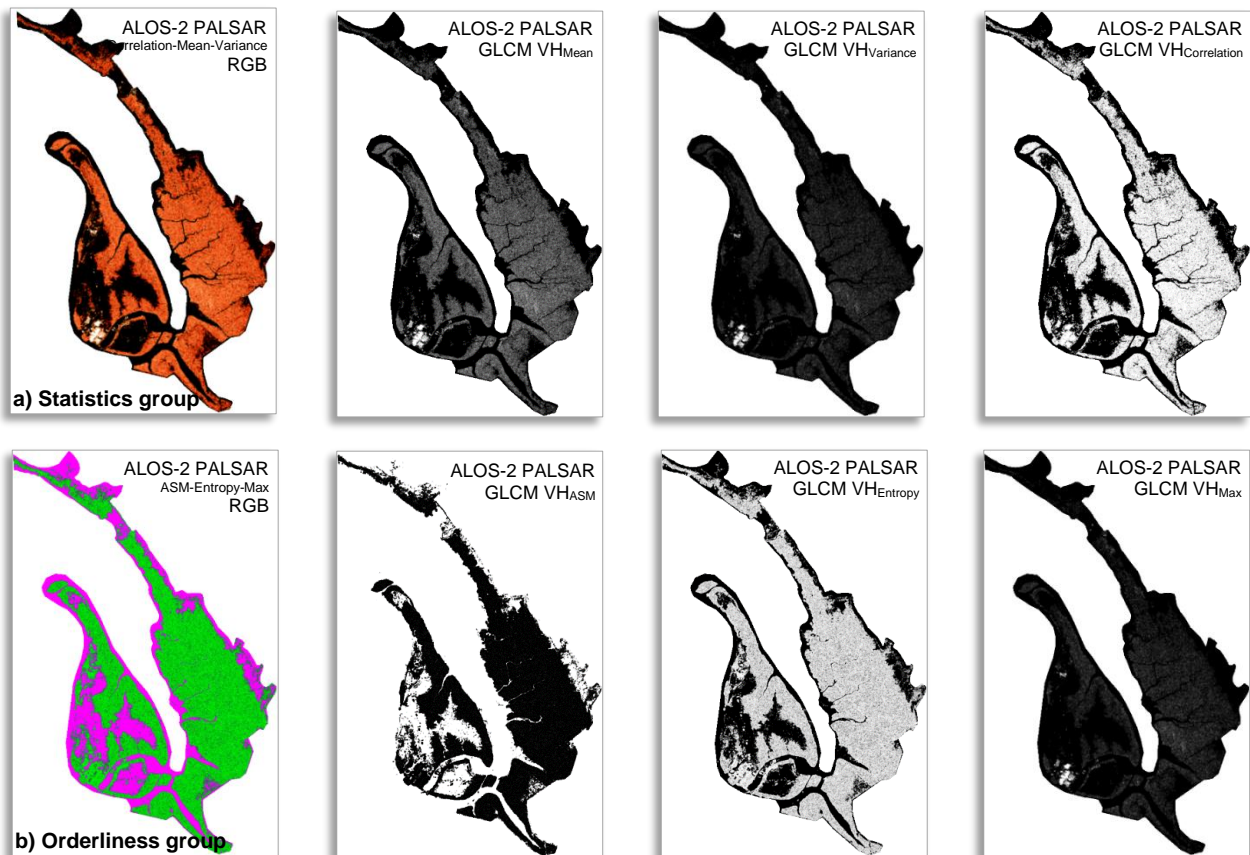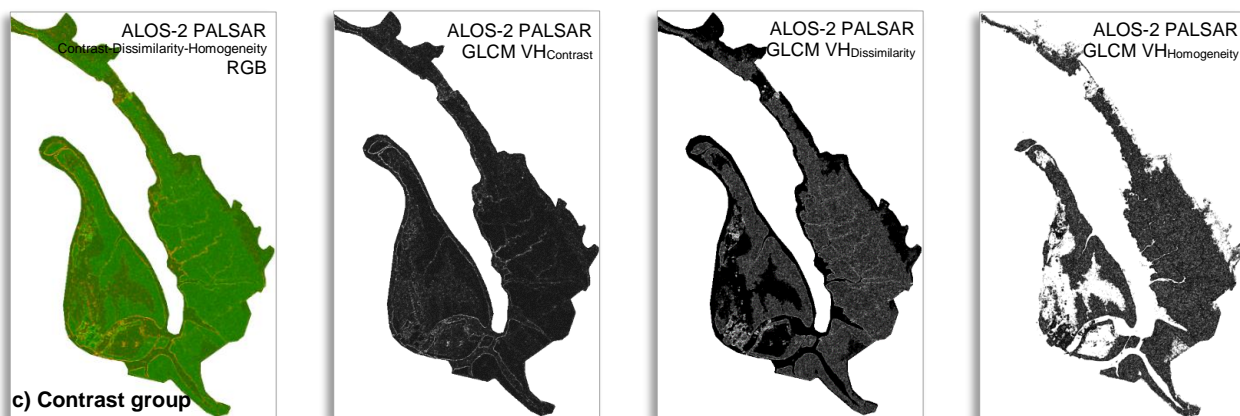
Figure 4-36: GLCM matrix combinations for ALOS-2 PALSAR

4.5.9 Regression Models – ALOS-2 PALSAR

In general, there were four models were derived from ALOS-2 PALSAR as described in Table 4-12. Backscatter and GLCM$_{VH}$ performed relatively better than the other two. The scatterplots for ALOS-2 PALSAR regression models are given in Appendix D 1-2.

Table 4-12: Regression models from ALOS-2 PALSAR

Model	R^2	Equations	Relation
RM-ALOS2$_{VH}$	0.14	$y = 12.451x + 270.59$	Positive linear
RM-ALOS2$_{PC-2}$	0.09	$y = -9.626x + 265.20$	Negative linear
RM-ALOS2$_{GLCM-VHvariance}$	0.15	$y = 0.0328x + 10.835$	Positive linear
RM-ALOS2$_{RVI}$	0.09	$y = 0.002x + 0.6138$	Positive linear

4.5.10 Polarimetric Matrix Analysis – ALOS-2 PALSAR

To work with polarimetric components of ALOS-2 PALSAR covariance (C3) and coherence (T3) matrices were calculated. In Figure 4-37, four polarisations of complex image are shown after calibration process. On the left complex RADAR image structure is shown.
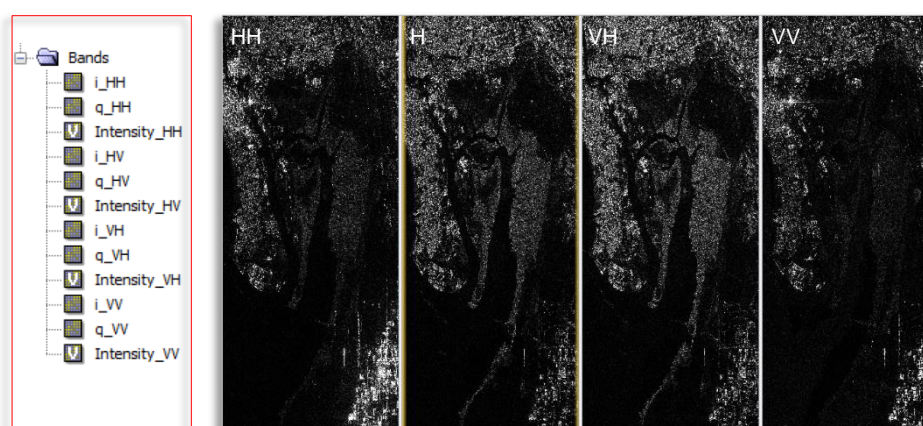
Figure 4-37: Four polarization of ALOS-2 PALSAR complex image

In Figure 4-38, diagonal of the (3x3) coherency matrix (T_{11}, T_{22}, T_{33}) is shown. This matrix was the starting point to compute target decomposition.
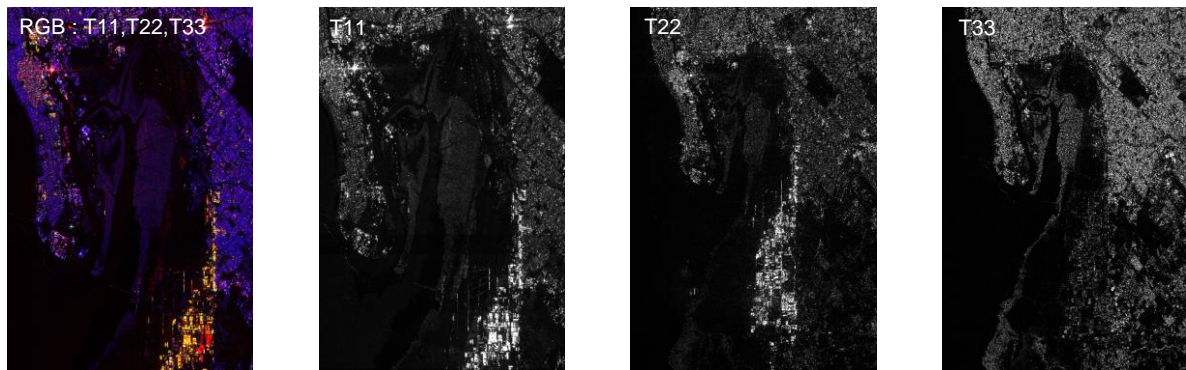
Figure 4-38: T3 matrix of ALOS-2 PALSAR

4.5.10.1 Freeman-Durden Decomposition

This composition is a model based decomposition and it was computed for surface, volume and double bounce scattering in the target. The individual components of each scattering are shown in Figure 4-39 as a), b) and c). In this study, volume scattering seems to be dominant in as shown in Figure 4-39d. The calculation of total scattering power for each component is out of scope. However, in a Table 4-13, min, max and mean values were computed for each scattering component. The regression was applied on volume scattering vs field$_{Biomass}$ but the value of R^2 from regression against biomass was almost 0 and no correlation was found. Hence, volume scattering was not taken into account for further analysis.
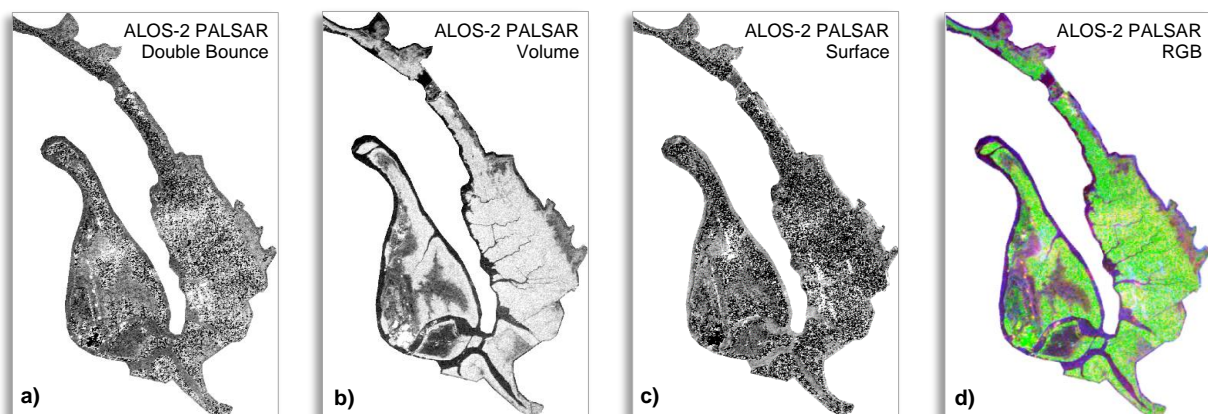
Figure 4-39: Freeman-Durden composition for ALOS-2 PALSAR

Table 4-13: Polarimetric scattering summary

Scattering Type	min	max	mean
Double bounce scattering	-23.82	11.43	-17.39
Volume scattering	-23.82	13.13	-11.76
Surface scattering	-23.82	9.44	-18.09

4.5.10.2 H-α Plane Decomposition

This decomposition is based on eigenvalues and eigenvectors and also known as Cloude-Pottier decomposition. In Figure 4-40, three components Entropy(H), Alpha(α) and Anisotropy(A) of H-α plane decomposition are shown. In Table 4-14 min, max values are given. Entropy value (0.84) most likely indicated that scattering phenomena is completely random and occurred in a complex scattering environment. Moreover, α mean angle value was close to 0.46, which indicated that volume scattering is present consistently in the target objects. Anisotropy mean value of 0.42 indicated that there are other scattering mechanisms also present such as double bounce or surface scattering but they are not dominant. Zone-5 of H-α plot (Figure 4-41), which most likely driven by entropy and alpha values, has showed the presence of antistrophic particles.
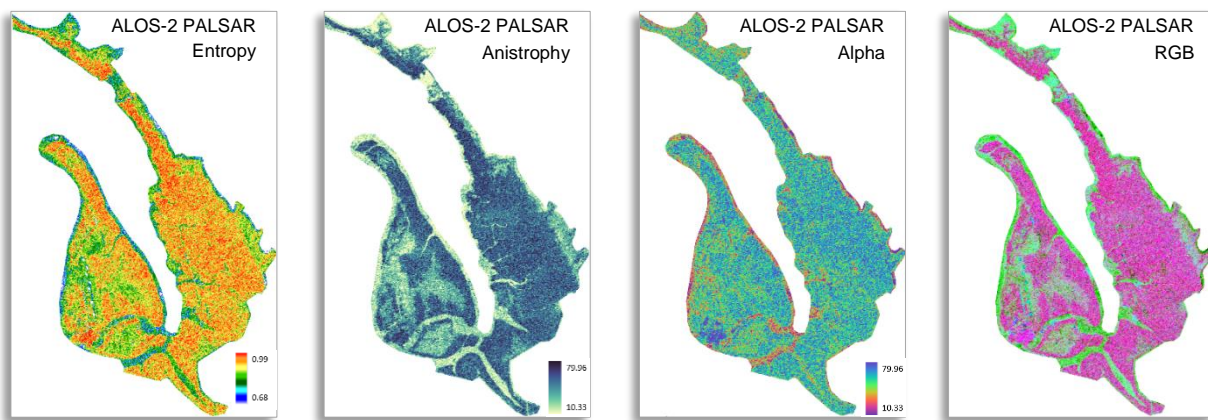
Figure 4-40: H-α decomposition

Table 4-14: Summary of H-α decomposition

Scattering Type	min	max	mean
Entropy (H)	0.068	0.99	0.84
Anistrophy (A)	0.0134	0.92	0.42
Alpha (α)	10.33	79.96	46.06

Z1 - Dihedral Reflector
Z2 - Dipole
Z3 - Bragg Surface
Z4 - Double Reflection
Z5 - Anisotropic Particles
Z6 - Random Surface
Z7 - Complex Structure
Z8 - Random Anisotropic Scatters
Z9 - Non-feasible
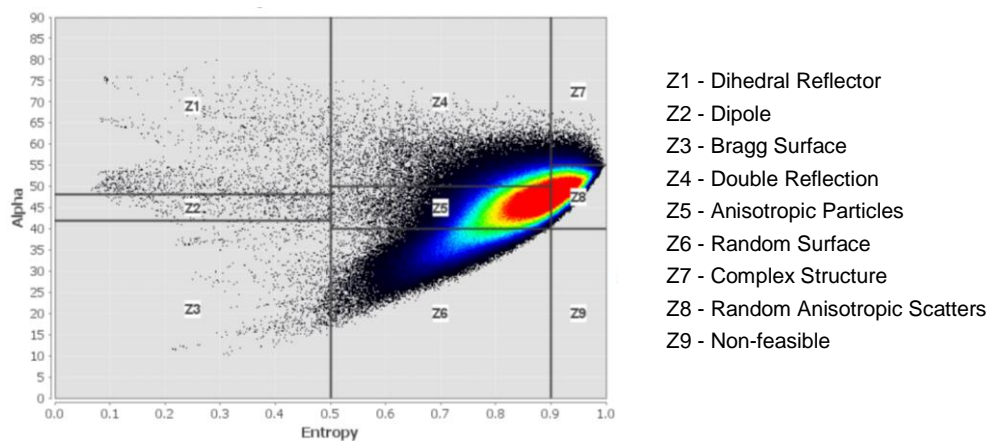
Figure 4-41: H-α plane plot for Cloude-Pottier decomposition

4.5.11 Pre-processing for Sentinel-1

In Figure 4-42, two polarisation of Sentinel-1 are shown. This is also known as dual pol satellite and provides backscatter information in C-band. All these polarisations were processed in ESA SNAP software for calibration, speckle filtering and geometric correction. The approximate resolution was 10m after geometric correction. Moreover, statistical regression, between RADAR backscatter and field$_{Biomass}$, computed R^2 value of 0.12 for C_{VV}.
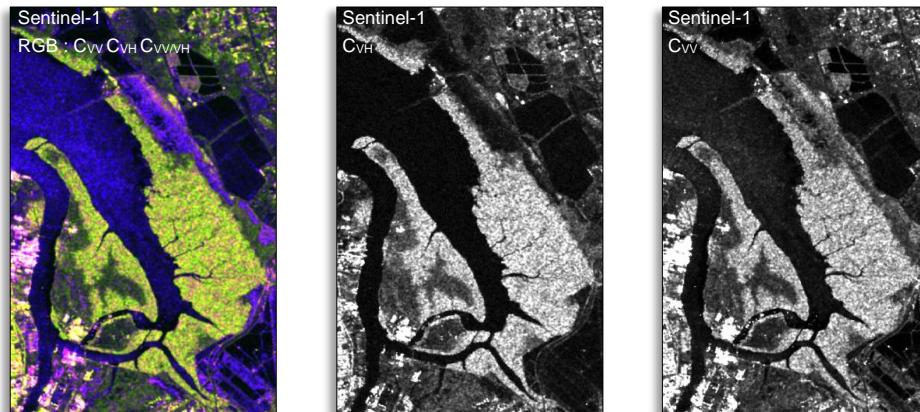
Figure 4-42: Sentinel-1 Polarisations

4.5.12 PCA Analysis – Sentinel-1

The PCA component of Sentinel-1 polarisations (VH, VV) is shown in Figure 4-43. The eigenvalues for first and second component was 0.0896 and 0.99 respectively. In a Table 4-15 below percentage for each eigenvalues has given. The noise value for this PCA was -0.0896. This PCA also explains that the PC-2 captured approximately 92% of the variance. Since PC-2 captured majority of the data, so it was used to calculate AGB and R^2 value from this analysis was 0.16, which does not seem to have any statistically significance.
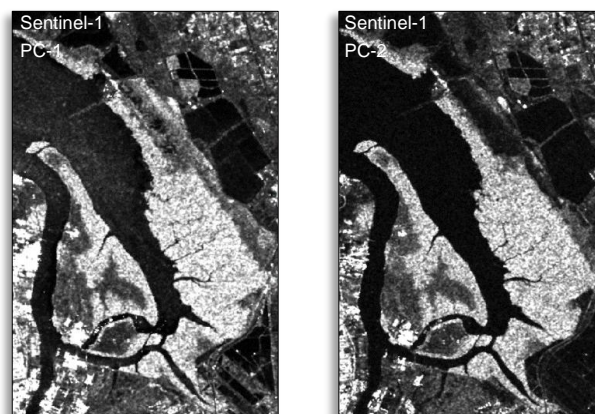
Figure 4-43: Sentinel-1 PCA

Table 4-15: Summary of eigenvalues and percentages of Sentinel-1

PC Layer	Eigenvalues	Eigenvalues (%)	Accumulative
PC1	0.0896	8.25	8.25
PC2	0.9959	91.74	100

4.5.13 GLCM Matrix – Sentinel-1

GLCM matrix was calculated for Sentinel-1 (VH & VV) polarisations. However, VV polarisation was taken into consideration due to its high value of variance. In the Figure, 4-44, statistical group for VV has shown (Mean, Variance and Correlation). Additionally, AGB estimation was estimated from this group and the R^2 value from GLCM VV_{mean} was 0.16.
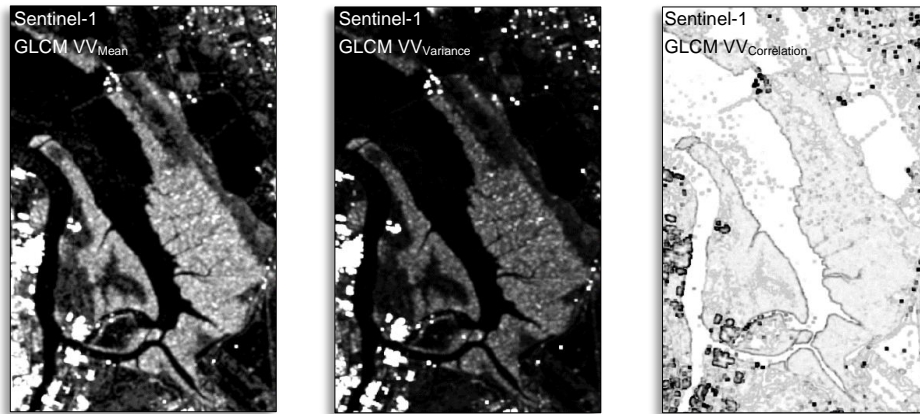
Figure 4-44: Sentinel-1 GLCM matrix

4.5.14 Regression Models – Sentinel-1

In Table 4-16, the summary of regression modes is given along with their equations and relationship. The Scatterplots for Sentinel-1 variables against field$_{Biomass}$ were calculated and given in Appendix D 1-3. Moreover, the highest value of R^2 was achieved from VV_{mean} which was 0.17 and the model was linear. In contrast, PC-2 model was exponential and R^2 value was 0.16.

Table 4-16: Regression models from Sentinel-1

Model	R^2	Equations	Relation
RM-S1$_{VH}$	0.12	$y = 0.0095x - 14.820$	Positive linear
RM-S1$_{PC-2}$	0.16	$y = 9.87e^{-5x} + 0.00867$	Exponential
RM-S1$_{GLCM-VVmean}$	0.17	$y = -0.01528x + 7.934$	Negative linear
RM-S1$_{RVI}$	0.12	$y = 0.00193x + 0.7583$	Positive linear

4.5.15 Regression Models Summary from RADAR

This summary (Table 4-17) shows that cross-polarised backscatter from ALOS-1 PALSAR is found to have the best correlation between backscatter and field$_{Biomass}$ and then ALOS-2 PALSAR seems to be the better choice. Moreover, PC-2 from ALOS-1 PALSAR seems to good choice potentially to calculate AGB. The scatterplots and regression equations for all RADAR based models are given in Appendices D 1-1, D 1-2, D 1-3.

Table 4-17: Summary of regression models from RADAR

	ALOS-1 PALSAR	R^2	ALOS-2 PALSAR	R^2	Sentinel-1	R^2
Backscatter	RM-ALOS1$_{HV}$	0.18	RM-ALOS2$_{VH}$	0.14	RM-S1$_{VH}$	0.12
PCA	RM-ALOS1$_{PC-2}$	0.27	RM-ALOS2$_{PC-2}$	0.09	RM-S1$_{PC-2}$	0.16
GLCM	RM-ALOS1$_{GLCM-HVmean}$	0.23	RM-ALOS2$_{GLCM-VHmean}$	0.15	RM-S1$_{GLCM-VVmean}$	0.17
RVI	RM-ALOS1$_{RVI}$	0.29	RM-ALOS2$_{RVI}$	0.09	RM-S1$_{RVI}$	0.12

4.5.16 Optimal Biomass Model from RADAR

The best regression model, GLCM HV$_{mean}$, derived from of ALOS-1 PALSAR with a R^2 value of 0.23. The value of R^2 was not statistically significant but seems to be higher among others RADAR variables.

$$y = 0.1375x + 26.71$$

Equation: 4-3

Equation 4-3 was used to generate biomass raster by replacing explanatory variable (x) with GLCM HV$_{mean}$ and resultant raster layer is showed in Figure 4-45b. The predicted biomass values, using RADAR, ranged from 26 to 35 t h^{-1} with a mean value of 30.32 t h^{-1}. Finally, this model yielded a total biomass of 38,034 tons. The quartile ranges from this model were (Q1=29.6, Q2=31.54, Q3=32.25) as shown in Figure 4-45a. For this quartile graph, it can be seen that the mean value is lower than the median. The detailed map is in Appendix (A 1-3).
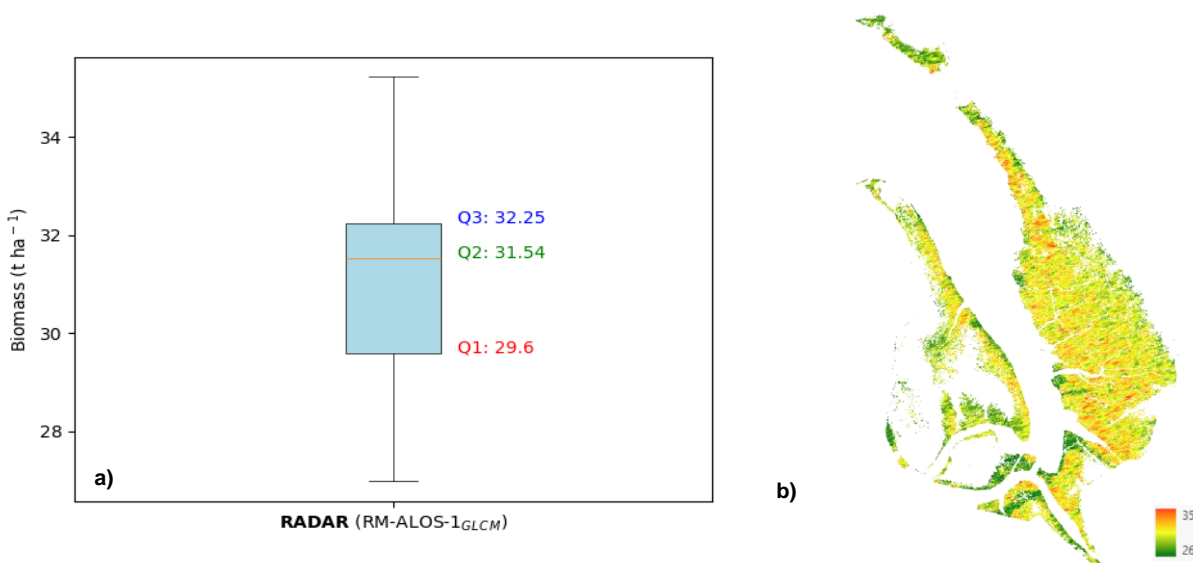
Figure 4-45: Biomass from best regression model (ALOS-1 PALSAR$_{GLCM\ HVmean}$)

4.6 Biomass Estimation from Pixel Based Fusion

In general, there were two pixel based fusion models (F1$_{4m}$ & F2$_{10m}$) were developed at two different resolutions (4m &10m).

4.6.1 Fusion Model – F1$_{4m}$

The fusion model F1$_{4m}$ was prepared using pixel-based fusion of ALOS-2 PALSAR and Pléiades Neo at 4m resolution. In the Figure 4-46 various combination of F1$_{4m}$ fusion models (Pléiades Neo & ALOS-2 PALSAR) are shown.
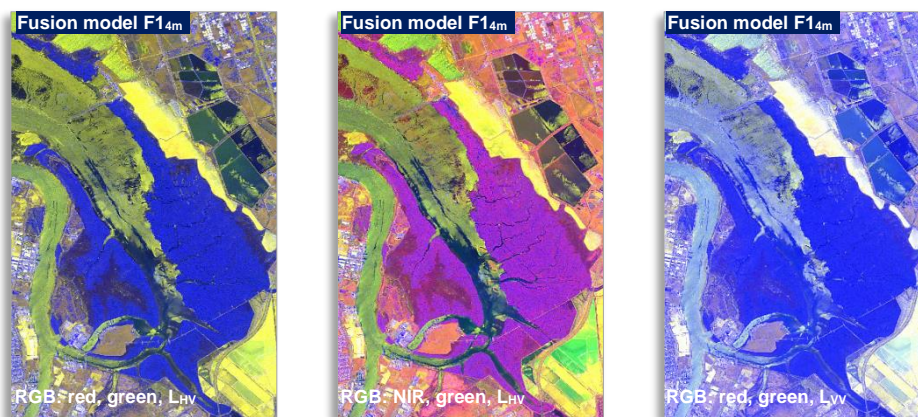
Figure 4-46: Fusion model F14m bands combinations

4.6.2 PCA for Fusion Model – F1$_{4m}$

In Figure 4-47, first three axis PC-1, PC-2 and PC-3 are shown. Originally, it was computed for 10 bands in total. From the eigenvalues percentage, it was identified that the first three PCA components captured the 94% of the variance and approximately 82% of the information was captured in first two components. Therefore, AGB regression model was run for PC-1 and PC-2 only, which computed the R^2 value of 0.001 and 0.27 respectively as shown in Table 4-18.
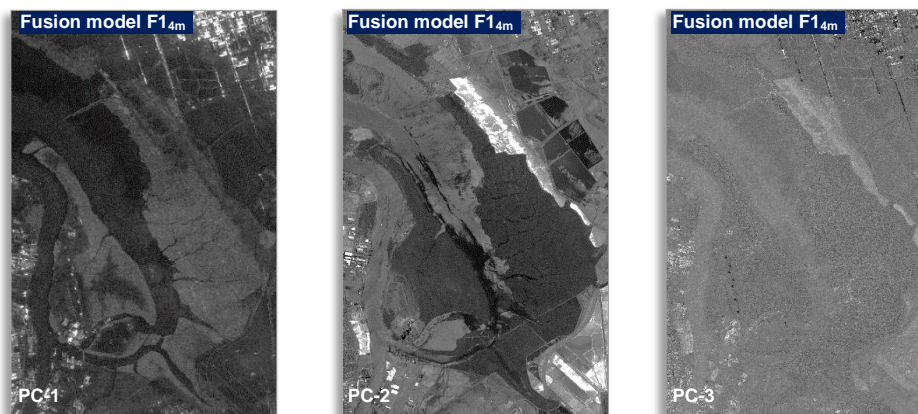
Figure 4-47: Fusion model F1$_{4m}$ PCA results

Table 4-18: Regression models from fusion F14m

Model	R^2	Equations	Relation
RM-F1$_{4m-PC-1}$	0.001	$y = 0.00114x + 50.892$	Very weak positive
RM-F2$_{4m-PC-2}$	0.27	$y = -0.1576x + 2554.15$	Negative linear

4.6.3 Fusion Model – F2$_{10m}$

The fusion model F2$_{10m}$ was prepared using pixel-based fusion of ALOS-2 PALSAR and Sentinel-2 data at 10m resolution. The output of this fusion was consisted of 8-bands. In Figure 4-48 various band combinations of fusions are shown in RGB.
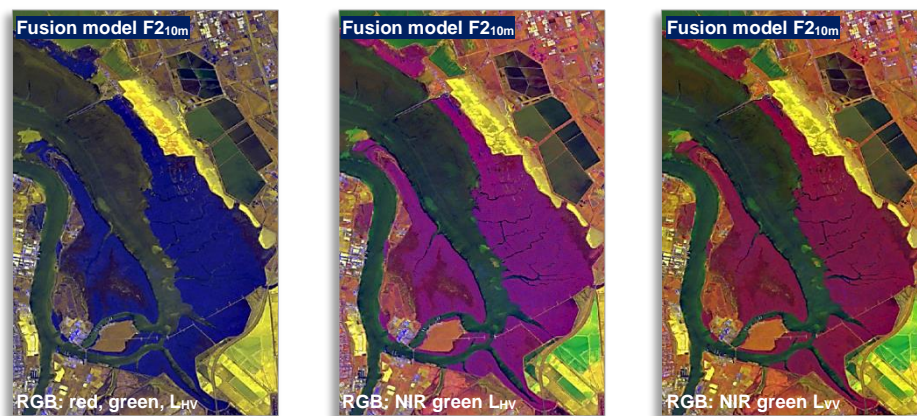
Figure 4-48: Fusion model F1$_{10m}$ bands combinations

4.6.4 PCA for Fusion Model – F2$_{10m}$

PCA was computed for 8-bands of fusion model F2$_{10m}$. In Figure 4-49, first three PCA are displayed (PC-1, PC-2 and PC-3). From the PCA analysis, it was identified that first two axes of PCA (PC-1, PC-2) captured 84% of the variance from fusion model. Therefore, AGB estimation was calculated using only two PCs. The results are shown in Table 4-19 along with their regression equations.
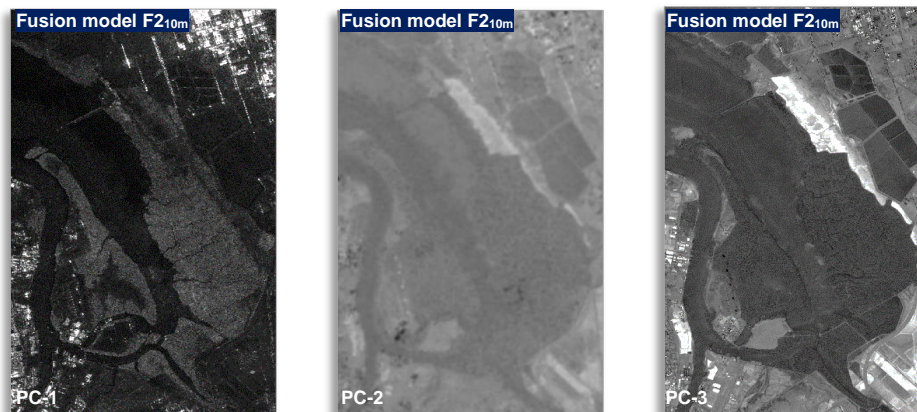
Figure 4-49: Fusion model F1$_{10m}$ PCA results

Table 4-19: Regression models from fusion model F2$_{10m}$

Model	R^2	Equations	Relation
RM-F2$_{10m-PC-1}$	0.09	$y = -0.0067x + 108.619$	Negative linear
RM-F2$_{10m-PC-2}$	0.01	$y = -0.00458x + 272.58$	Negative linear

4.6.5 Regression Models Summary from Fusion

In fusion-based approach (R^2=0.001) value was very low in PC-1 for RM-F1$_{4m-PC-1}$. However, PC-2 was little better in RM-F1$_{4m-PC-2}$, where R^2 value was 0.27. In Table 4-20 a summary of all these regression models is given obtained from two fusion approaches.

Table 4-20: Regression model results from fusion approaches

Model	R^2	Model	R^2
RM-F1$_{4m-PC-1}$	0.001	RM-F2$_{10m-PC-1}$	0.09
RM-F1$_{4m-PC-2}$	0.27	RM-F2$_{10m-PC-2}$	0.01

4.6.6 Optimal Regression Model from Fusion

The best regression model from fusion was RM-F1$_{4m-PC-2}$ with a R^2 value of 0.27 (Figure 4-50). This was negative linear model and was not statistically significant to explain more than 27% of the biomass variance. The regression equation for this model is given in Equation 4-4.

$$y = 0.1375x + 26.71$$

Equation: 4-4

However, there was no biomass calculated due to its lower R^2 value and it was pretty similar to RADAR.
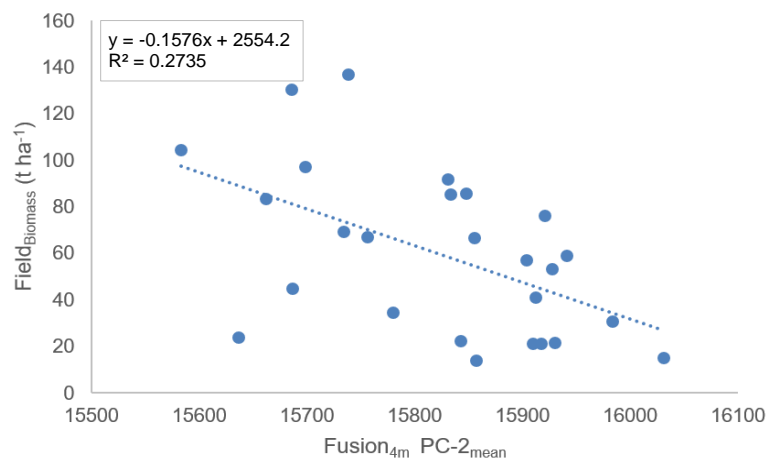
Figure 4-50: Optimal fusion regression model

4.7 Summary of Regression Models

Table 4-21 shows various regression models and their corresponding values calculated from multi-source datasets. To calculate mangrove AGB, regression models were established between

potential variables and field$_{Biomass}$. From the regression models, it can be seen that, the highest value of R^2 was 0.87, which was achieved from the field data. The second highest value of R^2 was 0.74 obtained from LIDAR. From the optical data, two highest values of R^2 were achieved; Pléiades Neo$_{NDVI}$ obtained 0.40 and Sentinel-2$_{MVI}$ achieved 0.48. In RADAR data, ALOS-1 PALSAR$_{RVI}$ computed the highest value of R^2 which was 0.28 although it is not statistically significant. From ALOS-2 PALSAR, GLCM VH$_{variance}$ gave the R^2 value of 0.15 and Sentinel-1 gave the R^2 value of 0.17 through GLCM VV$_{mean}$. Lastly, by using pixel-based fusion, model RM-F1$_{4m-PC-2}$ gave the highest value which was around 0.27. All additional regression models values are given in Table 4-21 and graphical (bar graph) representation is given in Figure 4-51.

Table 4-21: Regression model results summary

Data Domain	Regression Models	R^2	Type	Data Type
Field	RM-field$_{Biomass}$	0.87	Positive linear	*Survey data*
LiDAR	**RM-LiDAR$_{CHM}$**	**0.74**	**Positive linear**	*LiDAR*
Optical	RM-PLNeo$_{NDVI}$	0.40	Positive linear	*Pléiades Neo*
	RM-PLNeo$_{NDVI}$	0.48	Exponential	
	RM-PLNeo$_{NDVIre}$	0.06	Positive linear	
	RM-PLNeo$_{PC-2}$	0.27	Positive linear	
	RM-S2$_{NDVI}$	0.21	Positive linear	*Sentinel-2*
	RM-S2$_{NDVIre}$	0.40	Positive linear	
	RM-S2$_{MVI}$	**0.48**	**Positive linear**	
	RM-S2$_{CMRI}$	0.17	Positive linear	
	RM-S2$_{PC-2}$	0.18	Negative linear	
RADAR	RM-ALOS1$_{HV}$	0.18	Positive linear	*ALOS-1 PALSAR*
	RM-ALOS1$_{PCA}$	0.27	Exponential	
	RM-ALOS1$_{GLCM-HVmean}$	**0.23**	**Positive linear**	
	RM-ALOS1$_{RVI}$	0.29	Positive linear	
	RM-ALOS2$_{VH}$	0.14	Positive linear	*ALOS-2-PALSAR*
	RM-ALOS2$_{PC-2}$	0.09	Negative linear	
	RM-ALOS2$_{GLCM-VHvariance}$	0.15	Positive linear	
	RM-ALOS2$_{RVI}$	0.09	Positive linear	
	RM-S1$_{VH}$	0.12	Positive linear	*Sentinel-1*
	RM-S1$_{PC-2}$	0.16	Exponential	
	RM-S1$_{GLCM-VVmean}$	0.17	Negative linear	
	RM-S1$_{RVI}$	0.12	Positive linear	

	RM-F1_{4m-PC-1}	0.001	No Relation	
Fusion	**RM-F1_{4m-PC-2}**	**0.27**	**Negative linear**	*Pixel based fusion*
	RM-F2_{10m-PC-1}	0.09	Positive linear	
	RM-F2_{10m-PC-2}	0.01	No relationship	
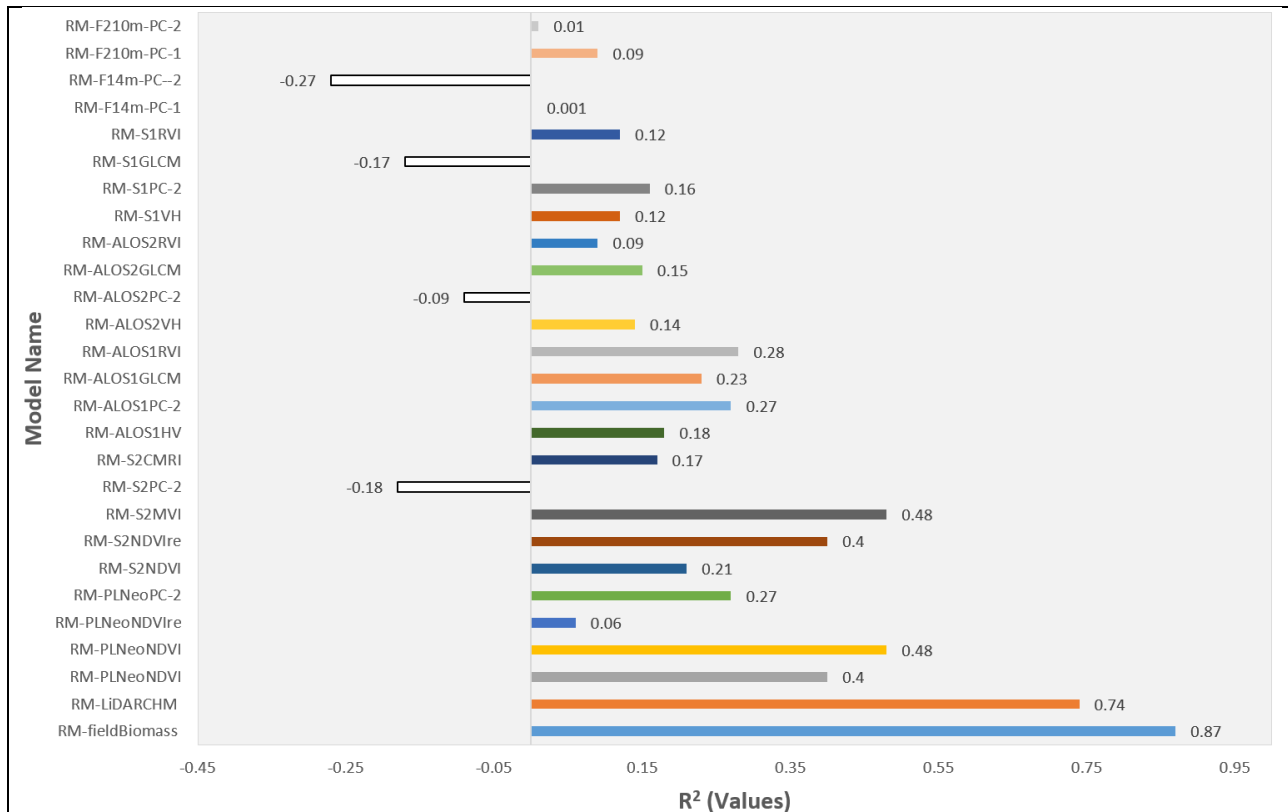
Figure 4-51: Bar graph for all regression models

4.8 Chapter Summary

This chapter summary shows the key findings and results derived to answer the research questions specified in Chapter 1. The strong value of R^2=0.87 showed that there is a strong correlation between LiDAR$_{CHM}$ and mean field$_{Biomass}$. Optical satellites Pléiades Neo and Sentinel-2, both are good to estimate mangrove extent and mangrove AGB estimation. In this study, mangrove extent was measured using machine-learning approaches (RT and ISO cluster) and results are given in Table 4-3. To measure AGB, NDVI was only able to explain almost 48% of the biomass variant based on R^2 values from both optical satellites. However, Sentinel-2$_{MVI}$ index gave the 0.40 value of R^2. Moreover, it has been seen during the spatial analysis (distance base analysis, tide analysis and NDVI analysis), *Avicenna marina* biomass distribution was higher along the salt creeks and lower away from salt creeks. Moreover, NDVI values were not consistent along the biomass distribution.

In microwave study of mangroves, three RADAR satellites (ALOS-1 PALSAR, ALOS-2 PALSAR & Sentinel-1) were taken into account. In RADAR based AGB estimations, backscatter coefficients, GLCM, PCA and RVI was used against field$_{Biomass}$. It is obvious to say that, regression models were having weak relationships overall in ALOS-2 PALSAR variables (GLCM, PCA & RVI) with field based biomass. However, ALOS-1 PALSAR more likely to have better value of R^2 using RVI based regression model, which was 0.28 as compared to other RADAR satellites. Additionally, two decomposition models (Freeman-Durden and H-α) were computed from ALOS-2 PALSAR to explore coherent and incoherent coefficients variables to calculate AGB. However, the results from scattering behaviour were not satisfactory. Last but not least, in this study, pixel based fusion approach was used to integrate optical and RADAR datasets. However, the highest value of R^2 was obtained from fusion model RM-F1$_{4m-PC-2}$ which was 0.27. The summary of all regression models is given in Table 4-21.

CHAPTER FIVE : DISCUSSIONS

This study demonstrated the advantages and limitations of AGB estimation using optical, LiDAR and RADAR datasets, supported by fieldwork. This study also highlighted the key processes of optical and RADAR processing and integration of multi-source data. Various regression algorithms proved that, it is possible to quantify mangrove above ground biomass – AGB and extent using space technologies. The following discussion addresses the results for each technology used in this study. Various regression models that were developed based on LiDAR, optical and RADAR datasets as described in Table 4-21. To calculate AGB estimation, mainly the optimum regression models were used from each technology. (Appendix B 1-1)

By using field data, mainly collected by others, biomass was estimated for 26 sample points using allometric models as implmented by many researchers (Jones *et al.* 2020; Chou *et al.* 2022; Banerjee *et al.* 2013; Rakotomavo 2018; Tran *et al.* 2017; Suwa *et al.* 2021; Vinh *et al.* 2019; Zanvo *et al.* 2023; Komiyama *et al.* 2008; Pandey *et al.* 2022) (Appendix C 1-1). Dittmann and Jones' research work was the main reference point for AGB estimation using fieldwork and allometric equations in this study. Later, this field based data (field$_{Biomass}$) was used in regression with other remote sensing variables. To validate, LiDAR$_{CHM}$ heights and to understand if there was change in canopy heights through the course of the research project a a ground truth survey was conducted on 7th March 2025. There was approximately 0.5m difference was found in heights for individual trees and other benchmarks (Appendices C 1-2, C 1-3). A correlation was established between field$_{Heights}$ and field$_{Biomass}$, which gave the R^2 value of 0.87 (Figure 4-1). This relation showed that there is strong relationship between field heights and biomass. From LiDAR data, a canopy height model (CHM) was extracted (Figure 4-2) and then correlation was established between LiDAR$_{CHM}$ and field$_{Heights}$ and, the resultant R^2 value was 0.87 (Figure 4-3a). Before moving on, it was also ensured that field$_{Heights}$ and LiDAR$_{CHM}$ heights values had a strong correlation. AGB estimations were calculated by applying regression between LiDAR$_{CHM}$ and field$_{Biomass}$. This approach was used by many researchers (Fatoyinbo *et al.* 2018; Effendi *et al.* 2023; Akay *et al.* 2009; Li *et al.* 2024; Wang *et al.* 2023; Mandal *et al.* 2024; Silva *et al.* 2018; Lagomasino *et al.* 2016; Feliciano *et al.* 2017). The best R^2 value was 0.74 (Figure 4-5a) and the relation was positive linear. AGB estimation values were ranges between 0.15 t h^{-1} to 202 t h^{-1} with an average value of 74.42 t h^{-1} (Figure 4-5b). The total AGB estimations was 96,149 tons (Figure 4-5c and Appendix A 1-1).

Even though, this study was conducted at high precision there are couple of uncertainties or systematic errors worth discussion. There were systematic differences in mean values of LiDAR and field data which was identified through field survey. The more likely cause of these errors in height values are most likely due to plant growth, as plant heights keep changing with the passage of time especially for young mangroves. Moreover, field sampling errors might be induced through

sampling measurements and uncertainty in top of trees. However, geometrical errors were also observed in LiDAR data as it appeared to be misaligned with other satellite dataset and later it was corrected through geo-referencing. Horizontal error could potentially lead to differences in vertical measurements. After adjustment, it was assumed that LiDAR based canopy heights were reliable and are useful to measure mangrove biomass. The predicted AGB from best LiDAR regression model (Fig 4-5a) ranged from 0.15 to 201 t ha^{-1}, with a mean value of 0.74 t ha^{-1}. The results (Fig 4-5b) might be over overestimating because of high point density and could be use of inappropriate allometric equation in the field biomass estimation from the field sample points. Another reason possibly, a canopy height model (CHM) itself while filtering first and last returns processing in the software. A study by (Li *et al.* 2024) claimed the LiDAR based estimations may differ due to uncertainties in structural characteristics of mangrove species. Along the same line, Fatoyinbo *et al.* 2018 also received the overestimated of biomass results by using airborne LiDAR even though it is believed that LiDAR based estimations are highly corrected and reliable (Akay *et al.* Li *et al.* 2024, Zhou *et al.* 2023;).

The optical dataset, used in this study was Pléiades Neo, and Sentinel-2. From this data, mangrove extent mapping and AGB estimation was computed. In assessing mangrove extent, two classification approaches were used for Pléiades Neo; random tree (RT) and ISO cluster. This classification work was carried out using a combination of six spectral bands, vegetation index (NDVI) and a LIDAR$_{CHM}$. RT, a variant of Random Forests, resulted in the extent of mangroves 13.09 km^2 & 15.78 km^2 for pan-sharpened (0.3m) and multispectral (1.3m) respectively. Similarly, ISO cluster computed 14.35 km^2 & 14.99 km^2 for both sets of imagery (Table 4-2). Validation process was carried out for Pléiades Neo RT classification at 0.3m and this model achieved a user accuracy of 0.98 with Kappa value of 0.86 (Table 4-3). This classification work led to preparation of a mangrove mask which was used in other datasets to mask the mangroves.

AGB estimation from optical imagery, vegetation indices and principal component analysis – PCA was used. The R^2 value from Pléiades Neo NDVI was 0.40 from linear model and 0.48 was from exponential model (Figure 4-15). Although, NDVIre was 0.16. The highest values of R^2 from Sentinel-2 vegetation indices MVI, NDVIre and NDVI were 0.48, 0.40 and 0.21 respectively (Figure 4-20). However, the optimum regression model was derived from Sentinel-2$_{MVI}$ and the value of R^2 was 0.48, which was almost similar to Pléiades Neo$_{NDVI}$ exponential model. Finally, Sentinel-2$_{MVI}$ regression model was used to quantify mangrove biomass. Moreover, many researchers (Farzanmanesh *et al.* 2024; Baloloy *et al.* 2020; Tran *et al.* 2022) used MVI in their research to calculate mangrove AGB and mangrove extent. Even, Baloloy *et al.* (2020) claimed that the probability of this index to identify mangroves from non-mangroves (other forest, built-up areas and soil) areas is very high as it involves three reflectance bands green, NIR and SWIR1. Thus, biomass values from Sentinel-2$_{MVI}$ model (Fig 4-23a) ranged between 0.15 to 202 tons ha^{-1} with an

average value of 74 tons ha^{-1}. The total biomass yielded from this model was 69,024 tones (Fig 4-23c and Appendix A 1-2).

PCA analysis was assessed from Pléiades Neo and Sentinel-2 and the best component was selected based on eigenvalue percentage. The R^2 value from Pléiades Neo PC-2 was 0.27 (Figure 4-16b) and from Sentinel-2 it was 0.18 (Figure 4-22). However, none of the R^2 value from both models was statistically significant to calculate AGB. Apart from regression models computations, few of the spatial analysis was also completed such as distance to water analysis (Figure 4-24), astronomical tide analysis (Figure 4-25), mangrove forest floor analysis(Figure 4-26) and NDVI comparisons (Figure 4-27). The main purpose of these analysis were to see mangrove distribution and reasons to identify the high and low biomass areas and water availability to them.

Given the above discussion about mangrove extent and AGB estimation, there were some potential errors were found during in this process which might include classification and geometrical errors. In some scenarios, R^2 values were very weekly positive and no relationship found at all. Henceforth, it was found that, correlation between optical variables and field$_{Biomass}$ does not seem to be strong as the highest value of R^2 value was 0.48%. It appears that, NDVI and MVI both able to explain 48% of the biomass variant. However, researchers believe that AGB estimation (Lucas *et al.* 2020; Hamdan *et al.* 2013; Neto *et al.* 2024; Nguyen *et al.* 2021; Aseran *et al.* 2021; Cao *et al.* 2023; Huong *et al.* 2023. Singh *et al.* 2023; Kamal *et al.* 2021; Rahman *et al.* 2018) and mangrove extent mapping is possible and viable technique.

The study of mangroves in microwave region (C & L bands) were taken into account using three satellites ALOS-1 PALSAR, ALOS-2 PALSAR and Sentinel-1. Previous research from (Austin *et al.* 2003; Harrell *et al.* 1995; Nandy *et al.* 2021; Stovall *et al.* 2021; Santoro *et al.* 2020; Ranson *et al.* 1997; Ningthoujam *et al.* 2017; Saatchi *et al.* 2011; Vaghela *et al.* 2021) proved that RADAR can provide AGB estimation. In this study, AGB estimations were derived from RADAR backscatter, PCA analysis, GLCM matrix and vegetation indices (RVI) and correlated with field$_{Biomass}$ and then values of R^2 were noted for each variable by applying regression (Table: 4-10, 4-12, 4-16). Initially, regression models were developed using backscatter coefficients of three satellites ALOS-1 PALSAR, ALOS-2 PALSAR and Sentinel-1. In general, these backscatter was not statistically significant and coefficient of determination (R^2) was very low. The highest value of (R^2=0.18), from the backscatter coefficient, was achieved from ALOS-1 PALSAR (Fig 4-28). In a similar study, by Hamdan *et al.* (2014) also received the low value of (R^2=0.40) using backscatter coefficients. By using PCA analysis, ALOS-1 PALSAR (Fig 4-30) computed the R^2 value of 0.27 and ALOS-2 PALSAR (Fig 4-35) computed 0.09 only. From Sentinel-1, the R^2 value was (0.16) from PC-2 (Fig 4-43). By using GLCM matrix cross-polarised perform better except Sentinel-1 (Fig 4-44) where VV performed better than the cross polarised. Through RADAR indices (RVI), ALOS-1 PALSAR

provided the highest value of coefficient of determination (R^2=0.28) as compared to other two satellites.

AGB estimations from RADAR was calculated using Equation 4-3 based on the best regression model (R^2=0.23) even though this value of R^2 was not statistically significant and appeared to have been weak relationship. This relationship shows that RADAR data might be able to 23% of the biomass variant and 77% is still unexplained. However, the resultant raster layer (Fig 4-45) computed the biomass values ranged from 2 – 62 t ha^{-1} with an average value of 30.32 t ha^{-1}. The total biomass from RADAR was 38,034 tons. (See Appendix A 1-3)

The result of this study, from RADAR, holds the view of the researchers (Cassol *et al.* 2021) that R^2 values depends on the filter selection for each polarisation while doing RADAR processing. This could be one of the potential reason for low R^2 values are observed in this study as (3x3) filter window or default filter settings was used for all polarisations. Another thought from (Lucas *et al.* 2021) reflects that, L-band RADAR can only explain AGB estimation up to 100-140 Mg ha^{-1}. In a similar study by (Hamdan *et al.* 2014) proved that, HV started to be saturated around 100 mg h^{-1}. Henceforth, it is obvious to say that, RADAR based AGB estimations are involved lot of other factors such as frequency, polarisation, incidence angle and moisture content. In a research by Lucas *et al.* (2007) also hold the same view. In another research by Cassol *et al.* 2021 suggest that AGB estimation also depends upon the better filter determination and type of forest structure. (See Appendices D 1-1, D 1-2, D 1-3 for regression models)

In addition to that, ALOS-2 PALSAR had some advantage in this study when it came to decomposition analysis of mangroves as it was quad pole and had four polarisations (HH, HV, VH, VV). To see scattering behaviour of the target objects coherency matrix (T3) was computed and then model based decomposition Freeman-Durden (Figure 4-39) was computed to see double bounce, volume and surface based scattering (Table 4-13). From H-α decomposition (Fig 4-41), entropy average value described that scattering phenomena is completely random and target objects are in complex scattering environment. The average value of α angle (α=0.46) indicated volume scattering dominance. Furthermore, anisotropy indicated the presence of other scattering phenomena based on average mean value of 0.42. Summary of H-α decomposition values are given in Table 4-12. Additionally, to see mangrove disturbances and structural behaviour two more RADAR indices (RFDI and CSI) were calculated along with RVI. RVI was directly used in AGB estimations as discussed earlier in part of discussion section. However, RFDI (Figure 4-34b) was used to see mangroves degradation and CSI identified (Figure 4-34c) horizontal and vertical structure of the canopy. Finally, these two indices helped to identify the mangrove biomass distribution along with structural characteristics.

Furthermore, in this research, RADAR data had couple of uncertainties in the datasets. Additionally, ALOS-2 PALSAR was misaligned with LiDAR$_{CHM}$ and it was georeferenced separately with optical imagery. Likewise, ALOS-1 PALSAR had geometrical errors and features were inconsistent with other optical and LiDAR datasets. Besides that, one of the advantage of RADAR on optical was that, the coastal areas most of the time remain under the influence of cloud, RADAR can observe mangroves in a day or night modes without any disturbance. Additionally, scattering base analysis and target decomposition is only possible with RADAR data and in this study, only some part is covered. However, some texture based analysis and PCA combinations are still need to explore.

Another unique aspect of this study was to develop fusion models. In this research two fusion models (F1$_{4m}$ & F2$_{10m}$) were generated using pixel based fusion of optical and RADAR data. Similar approaches were used by various researchers (Pohl & Genderen 2017; Alparone *et al.* 2015; Chang & Bai 2018). F1$_{4m}$ fusion model (Fig 4-46) was made using ALOS-2 PALSAR and Pléiades Neo data at 4m resolution and then PCA analysis was performed on it to capture the maximum information and reduce the dimensionality. The best PCA components were selected based on eigenvalues percentages (Table 4-18) and regression was performed on these two PCA components separately and field$_{Biomass}$. From F1$_{4m}$ model, PC-2 (Fig 4-47) given the R^2 value of value of 0.27 and PC-1 just only 0.001. Although, both of the values are not statistically significant and even PC-1 is not able to explain more than 27% of the biomass variant. The second fusion model F1$_{10m}$ (Fig 4-48) was generated through ALOS-2 PALSAR and Sentinel-2 at 10m resolution. Similarly, the PCA (Fig 4-49) was computed and two regression models were developed (RM-F2$_{10m-PC-1}$ with R^2 = 0.09) & (RM-F2$_{10m-PC-2}$ with R^2 0.01). The relevant regression equations and equivalents R^2 values for this model is given in (Table 4-19). Overall, no regression value was not statistically significant to explain AGB estimation. This optimum model (Fig 4-50) appeared to be similar to the RADAR and no biomass were calculations were made. However, in this study pixel-based approach was used for fusion but feature fusion can also have some potential for future work. Alternatively, few other options of fusion combinations such as (LiDAR + Optical, LiDAR + RADAR and RADAR + RADAR) might have potential to explore for AGB estimation but they were not explored due to time constraint and out of the scope of this study.

It, was also identified that, satellite datasets were varied in their temporal resolutions however, the same seasons was taken into consideration. For instance, the LiDAR data (Table 3-1) was acquired in Mar 2021 and optical data (Table 3-2) Pleaides Neo and Sentinel-2 was acquired in Nov, 2023. Moreover, ALOS-2 PALSAR and Sentinel-1 was acquired in Oct, 2023 and Nov, 2023 respectively (Table 3-6). Therefore, it can be said that LiDAR data is almost 5 years old and one of the RADAR data ALOS-1 PALSAR is almost 16 years old as this satellite service was stopped. Due to temporal uncertainties in spatial data obviously, there was information errors in decisions making process. Hence, based on the given data we do not have choice to identify them and

moving on with current datasets although it was challenging. Thus, there is a possibility; results might be varied due to systematic errors in the spatial data. Moreover, while regression it has been seen that, most of the models (Table 4-21) were more likely to have linear positive relationship but in some cases, negative relationships also found (Fig 4-51). In few scenarios models observed slightly higher values of R^2 in exponential models but due to complexity of the exponential models they were not taken into consideration and linear models were used in AGB estimations. Moreover, in some cases very low R^2 were observed which ultimately showed there are very weak relationships in the data. This study also suggested that the satellite remote sensing approach made this study non-intrusive, potentially repeatable and regular, and showed excellent capability to map mangrove extent, especially when multiple datasets were used. Despite literature (Effendi *et al.* 2024; Ranson *et al.* 1997; Blanco *et al.* 2018; Lee *et al.* 2018; Farzanmanesh *et al.* 2024) displaying good correlations, estimation of AGB using different satellites and differing approaches. However, this research was less convincing, only explaining approximately 50% of the biomass variability using satellite remote sensing. Although, LiDAR based estimation found to be a bit overestimated but regression equation (Equation 4-1) showed there is a good correlation (R2=0.74) between $LiDAR_{Heights}$ and $field_{Biomass}$. Having said that, it was challenging to determine which regression model was more consistent than others in terms of AGB accuracy and which satellite data, or combination, was most suitable. Nevertheless, it appears that, in general, statistical regression and machine learning approaches are useful to calculate AGB and excellent for mapping mangrove extent. Research on the application of the recently launched NISAR and BIOMASS RADAR satellites to mangrove mapping is a future direction worth pursuing.

CHAPTER SIX : CONCLUSION AND FUTURE RESEARCH

This study explored the usefulness of multi-source remote sensing datasets and various statistical approaches to study mangrove extent and above ground biomass (AGB) for mangroves. The high-resolution satellites are having their own spatial benefits as compared to lower-resolution satellites. However, airborne LiDAR data is also very effective, but comes at higher cost and thus lack of frequency. In this study, field data was used to establish the relationship between $LiDAR_{CHM}$ and mean $field_{Heights}$ through regression. The accuracy of the results from multi-source data also depend on the field data sampling, canopy structure and moisture conditions.

Coarse resolution of optical and RADAR imagery, at this study site does provide an estimate of AGB estimations for mangroves, but with lower confidence than from airborne systems. High correlation was found between field and LiDAR data, but role of optical, RADAR and fusion approaches cannot be denied especially in terms of extent mapping.

This research can be expanded towards all mangroves of South Australia for deeper insights of mangrove structure, ecosystems and biomass or possibly for whole Australia for the same species. In current approach, LiDAR, optical and RADAR datasets was used to calculate AGB but for future, recently launched satellites such as Biomass and NISAR are potentially good option. Biomass is the first P-band satellite to measure forests structure in more depth with a wavelength of 70cm. In contrast, NISAR (simultaneous L-band & S-band) dual polarisation capability may enable forest insights which can make difference to the forest canopy study. With regards to height estimations InSAR of forest canopies using high resolution RADAR from Capella, IceSAR, Umbra and TanDEM-X datasets can also be considered but a cost compared with the lower resolutions from Biomass and NISAR. A few more RADAR approaches can also be considered such as PolInSAR and tomography. Moreover, to improve classification work GLCM and object image based analysis can be added in machine learning and deep learning approaches. For the field based data collection, terrestrial laser scanning and close-range sampling is required.

REFERENCES

Akay, AE, Oğuz, H, Karas, IR & Aruga, K 2009, 'Using LiDAR technology in forestry activities', *Environment Monitoring Assessment,* vol. 151, pp. 117-125, doi: doi.org/10.1007/s10661-008-0254-1.

Alparone, L, Aiazzi, B, Baronti, S & Garzelli, A 2015, *Remote Sensing Image Fusion*, CRC Press, FL, USA.

Alwis, RHNS, Pawuluwage, SM, Bellanthudawa, BKA, Perera, IJJUN, Nawalage, NMSK, Amarathunga, AAD & Halwatura, D 2025, 'Small scale mangrove conservation forests enhance significant above-ground and below-ground carbon sequestration: A measure of blue carbon stock for climate change mitigation', *Regional Studies in Marine Science*, vol. 91, doi: doi.org/10.1016/j.rsma.2025.104546.

Anderson, ALF, Herndon, KE, Thapa, RB & Cherrington, E 2019, *The SAR Handbook Comprehensive Methodologies for Forest Monitoring and Biomass Estimation,* CRC Press, FL, USA.

Anees, SA, Mehmood, K, Khan, WR, Sajjad, M, Alahmadi, TA, Alharbi, SA & Luo, M 2024, 'Integration of machine learning and remote sensing for above ground biomass estimation through Landsat-9 and field data in temperate forests of the Himalayan region', *Ecological Informatics,* vol. 82, pp. 1-19, doi: doi.org/10.1016/j.ecoinf.2024.102732.

Aseran, AW, Darmawan, S & Hernawati, R 2021, 'Estimation of mangrove biomass using Landsat data on google earth engine (GEE) platform', *The 42nd Asian Conference on Remote Sensing (ACRS2021), Can Tho University, Can Tho, Vietnam*, pp. 1-6.

Aslan, A & Alijahdali, MO 2022, 'Characterizing global patterns of mangrove canopy height and aboveground biomass derived from SRTM data', *Forests*, vol. 13, pp. 1-17, doi: doi.org/10.3390/f13101545.

Attarchi, S 2020, 'Extracting impervious surfaces from full polarimetric SAR images in different urban areas', *International Journal of Remote Sensing*, vol. 51, no. 12, pp. 4644-4663, doi: doi.org/10.1080/01431161.2020.1723178.

Austin, JM, Mackey, BG & Niel, KPV 2003, 'Estimating forest biomass using satellite RADAR: An exploratory study in temperate Australian Eucalyptus forest', *Forest Ecology and Management,* vol. 176, pp. 575-583, doi: doi.org/10.1134/S1995425522050031.

Babiy, IA, Im, ST & Kharuk, VI 2022, 'Estimating aboveground forest biomass using RADAR methods', *Contemporary Problems of Ecology,* vol. 15, pp. 433-448, doi: doi.org/10.1134/S1995425522050031.

Baghdadi, N & Zribi, M 2016, *Land Surface Remote Sensing in Agriculture and Forest,* Elsevier, London, UK.

Bagot, KC, Herndon, KE, Nicolau, AP, Arias, VM, Evans, C, Parache, H, Mosely, K, Narine, Z & Zutta, B 2024, 'Integrating SAR, optical, and machine learning for enhanced coastal mangrove monitoring in Guyana', *Remote Sensing,* vol. 16, pp. 1-20, doi: doi.org/10.3390/rs16030542.

Baloly, AB, Blanco, AC, Ana, RRCS & Nadaoka, K 2020, 'Development and application of a new mangrove vegetation index (MVI) for rapid and accurate mangrove mapping', *ISPRS Journal of Photogrammetry and Remote Sensing*, vol. 166, pp. 95-117, doi: doi.org/10.1016/j.isprsjprs.2020.06.001.

Baloloy, AB, Blacno, AC, Candido, CG, Argamosa, RJL, Dumalag, JBLC, Dimapilis, LLC & Paringit, EC 2018, 'Estimation of mangrove forest aboveground biomass using multispectral bands, vegetation indices and biophysical variables derived from optical satellite imageries: Rapideye, Planetscope and Sentinel-2', *ISPRS Annals of the Photogrammetry, Remote Sensing and Spatial Information Sciences,* vol. IV-3, pp. 29-36, doi: doi.org/10.5194/isprs-annals-IV-3-29-2018.

Banerjee, K, Sengupta, K, Raha, A & Mitra, A 2013, 'Salinity based allometric equations for biomass estimation of Sundarban mangroves', *Biomass and Bioenergy,* vol. 56, pp. 382-391, doi: doi.org/10.1016/j.biombioe.2013.05.010.

Bindu, G, Rajan, P, Jishnu, ES & Joseph, KA 2020, 'Carbon stock assessment of mangroves using remote sensing and geographic information system', *The Egyptian Journal of Remote Sensing and Space Sciences,* vol. 23, pp. 1-9, doi: doi.org/10.1016/j.ejrs.2018.04.006.

Binh, NA, Hauser, LT, Hoa, PV, Thao, GTP, An, NN, Nhut, HS, Phuong, TA & Verrelst, J 2022, 'Quantifying mangrove leaf area index from Sentinel-2 imagery using hybrid models and active learning', *International Journal of Remote Sensing*, vol. 43, pp. 5636-5657, doi: doi.org/10.1080/01431161.2021.2024912.

Blanco, CMG, Gomez, VMB, Crespo, P, Ließ, M 2018, 'Spatial prediction of soil water retention in a Páramo landscape: Methodological insight into machine learning using random forest', *Geoderma*, vol. 316, pp. 100-114, doi: doi.org/10.1016/j.geoderma.2017.12.002.

Borra, S, Thanki, R & Dey, N 2019, *Satellite Image Analysis: Clustering and Classification,* Springer, Gateway East, Singapore.

Brown, DNB, Connolly, RM, Richards, DR, Adame, F, Friess, DA & Brown, CJ 2020, 'Global trends in mangrove forest fragmentation', *Scientific Reports*,

vol. 10, pp. 1-8, doi: doi.org/10.1038/s41598-020-63880-1.

Brown, I, Mwansasu, S & Westerberg, LO 2016, 'L-band polarimetric target decomposition of mangroves of the Rufiji Delta, Tanzania', *Remote Sensing,* vol. 8, pp. 1-14, doi: doi.org/10.3390/rs8020140.

Bunting, P, Rosenqvist, A, Hilarides, L, Lucas, RM, Thomas, N, Tadono, T, Worthington, TA, Spalding, M, Murray, NJ & Rebelo, LM 2022, 'Global Mangrove Extent Change 1996–2020: Global Mangrove Watch Version 3.0', *Remote Sensing*, vol. 14, pp. 1-32, doi: doi.org/10.3390/rs14153657.

Bunting, P, Rosenqvist, A, Lucas, RM, Rebelo, LM, Hilarides, L, Thomas, N, Hardy, A, Itoh, T, Shimada, M & Finlayson, CM 2018, 'The global mangrove watch—a new 2010 global baseline of mangrove extent', *Remote Sensing,* vol. 10, pp. 1-19, doi: doi.org/10.3390/rs10101669.

Campbell, AD, Fatoyinbo, T, Charles, SP, Chavez, LLB, Goes, J, Gomes, H, Halabisky, M, Holmquist, J, Lohrenz, S, Mitchell, C, Moskal, LM, Poulter, B, Qiu, H, Sousa, CHRD, Sayers, M, Simard, M, Stewart, AJ, Singh, D, Trettin, C, Wu, J, Zhang, X & Lagomasino, D 2022, 'A review of carbon monitoring in wet carbon systems using remote sensing', *Environmental Research Letters*, vol. 17, pp. 1-41, doi: doi.org/10.1088/1748-9326/ac4d4d.

Canty, MJ 2019, *Image Analysis, Classification, and Change Detection in Remote Sensing With Algorithms for Python,* 4th edn, CRC Press, FL, USA.

Cao, M, Cao, S, Sun, W & Kong, F 2023, 'A high-resolution grassland aboveground biomass estimation method based on SfM and grassland height factor', *IEEE International Conference on Electrical, Automation and Computer Engineering (ICEACE), Changchun, China,* pp. 1224-1227, doi: doi.org/10.1109/ICEACE60673.2023.10442657.

Cassol, HLG, Aragão, LEDOECD, Moraes, EC, Carreiras, JMDB & Shimabukuro, YE 2021, 'Quad-pol advanced land observing satellite/phased array L-band synthetic aperture radar-2 (ALOS/PALSAR-2) data for modelling secondary forest above-ground biomass in the central Brazilian Amazon', *International Journal of Remote Sensing,* vol. 42, pp. 4985-5009, doi: doi.org/10.1080/01431161.2021.1903615.

CDSE n.d.,*Calculate Radar Vegetation Index (RVI) using Sentinel-1 GRD collection*, Copernicus Data Space Ecosystem - CDSE, viewed 5 Oct 2025, <https://documentation.dataspace.copernicus.eu/APIs/openEO/openeo-community-examples/python/RVI/RVI.html>.

Chang, NB & Bai, K 2018, *Multisensor Data Fusion and Machine Learning for Environmental Remote Sensing*, CRC Press, FL, USA.

Chave, J, Andalo, C, Brown, S, Cairns, MA, Chambers, JQ, Eamus, D, Folster, H, Fromard, F, Higuchi, N, Kira, T, Lescure, JP, Nelson, BW, Ogawa, H, Puig, H, Riera, B & Yamakura, T 2005. 'Tree allometry and improved estimation of carbon stocks and balance in tropical forests', *Oecologia*, vol. 145, pp. 87–99, doi: doi.org/10.1007/s00442-005-0100-x.

Chen, H, White, JC & Beaudoin, A 2023, 'Derivation and assessment of forest-relevant polarimetric indices using RCM compact-pol data', *International Journal of Remote Sensing*, vol. 44, pp. 381-406, doi: doi.org/10.1080/01431161.2022.2164528.

Chen, G, Wang, L & Kamruzzaman, MM 2020, 'Spectral classification of ecological spatial polarization SAR image based on target decomposition algorithm and machine learnings', *Neural Computing and Applications ,* vol. 32, pp. 5449-5460, doi: doi.org/10.1007/s00521-019-04624-9.

Chou, MQ, Lin, WJ, Lin, CW, Wu, HH & Lin, HJ 2022, 'Allometric equations may underestimate the contribution of fine roots to mangrove carbon sequestration', *Science of The Total Environment,* vol. 833, pp. 1-10, doi: doi.org/10.1016/j.scitotenv.2022.155032.

Choudhary, B, Dhar, V & Pawase, AS 2024, 'Blue carbon and the role of mangroves in carbon sequestration: Its mechanisms, estimation, human impacts and conservation strategies for economic incentives', *Journal of Sea Research,* vol. 199, pp. 2-22, doi: doi.org/10.1016/j.seares.2024.102504.

Chuvieco, E 2016, *Fundamentals of Satellite Remote Sensing: An Environmental Approach,* 2nd edn, CRC Press, FL, USA.

Contessa, V, Dyson, K, Mulas, PPV, Kindgard, A, Liu, T, Saah, D, Tenneson, K & Pekkarinen, A 2023, 'Uncovering dynamics of global mangrove gains and losses', *Remote Sensing*, vol. 15, pp. 1-22, doi: doi.org/10.3390/rs15153872.

Conti, LA, Barcellos, RL, Oliveira, P, Neto, FCN & Lignon, MC 2025, 'Geographic object-oriented analysis of UAV multispectral images for tree distribution mapping in mangroves', *Remote Sensing,* vol. 17, pp. 1-26, doi: doi.org/10.3390/rs17091500.

DCCEEW 2017, *NVIS Fact sheet - MVG 23 –* Mangroves, Department of Climate Change, Energy, the Environment and Water - DCCEEW, viewed 30 Sep 2025, <https://www.dcceew.gov.au/sites/default/files/documents/mvg23-nvis-mangroves.pdf>.

Debastiani, AB, Sanquetta, CR, Corte, APD, Pinto, NS, Rex, FE 2019, 'Evaluating SAR-optical sensor fusion for aboveground biomass estimation in a Brazilian tropical forest', *Annals of Forest Research*, vol. 62, pp. 109-122, doi: doi.org/10.15287/afr.2018.1267.

Deodoro, SC, Moral, RDA, Fealy, R, McCarthy, T & Fealy, R 2024, 'Using the surface scattering mechanism from dual-pol SAR data to estimate topsoil particle-size fractions', *International Journal of Applied Earth Observation and Geoinformation,* vol. 128, pp. 1-19, doi: doi.org/10.1016/j.jag.2024.103742.

DEWNR 2007, *Reference Paper 2 : Key habitat features necessary to sustain the dolphin population, Department of Environment, Water and Natural Resources - DEWNR*, viewed 30 Sep 2025, <https://cdn.environment.sa.gov.au/environment/docs/ads-reference-paper-habitat-rep.pdf>.

Doughty, CL, Ambrose, RF, Okin, GS & Cavanaugh, KC 2021, 'Characterizing spatial variability in coastal wetland biomass across multiple scales using UAV and satellite imagery', *Remote Sensing in Ecology and Conservation*, vol. 7, pp. 411-429, doi: doi.org/10.1002/rse2.198.

Duke, NC 2006, *Australia's Mangroves The authoritative guide to Australia's mangrove plants,* University of Queensland, Brisbane, Australia.

Duncanson, L, Neuenschwander, A, Hancock, S, Thomas, N, Fatoyinbo, T, Simard, M, Silva, CA, Armston, J Luthcke, SB, Hofton, M, Kellner, JR & Dubayah, R 2020, 'Biomass estimation from simulated GEDI, ICESat-2 and NISAR across environmental gradients in Sonoma county California', *Remote Sensing of Environment,* vol. 242, pp. 1-16, doi: doi.org/10.1016/j.rse.2020.111779.

Effendi, NAFN, Zaki, NAM, Latif, ZA & Khanan, MFA 2024, 'Combination of hyperspectral and LiDAR for aboveground biomass estimation using machine learning', *Transactions in GIS,* vol. 28, pp. 1750-1771, doi: doi.org/10.1111/tgis.13214.

Ehlers, D, Wang, C, Coulston, J, Zhang, Y, Pavelsky, T, Frankenberg, E, Woodcock, C & Song, C 2022, 'Mapping forest aboveground biomass using multisource remotely sensed data', *Remote Sensing,* vol. 14, pp. 1-19, doi: doi.org/10.3390/rs14051115.

ESRI n.d., *SAR Indices function*, Environmental Systems Research Institute - ESRI, viewed 5 Sep 2025, <https://pro.arcgis.com/en/pro-app/latest/help/analysis/raster-functions/sar-indices-function.htm?>.

Estornell, J, Gavilá, JMM, Sebastiá, MT & Mengual, J 2013, 'Principal component analysis applied to remote sensing', *Modelling in Science Education and Learning,* vol. 6, pp. 83-89, doi: doi.org/10.4995/msel.2013.1905.

Fang, L, Mu, W, Wang, N & Liu, T 2024, 'An optimised scattering power decomposition method oriented to ship detection in polarimetric synthetic aperture radar imagery', *IET Radar, Sonar & Navigation*, vol. 18, pp. 2642-2656, doi: doi.org/10.1049/rsn2.12665.

Farzanmanesh, R, Khoshelham, K, Volkova, L, Thomas, S, Ravelonjatovo, J & Western, CJ 2024, 'Quantifying mangrove aboveground biomass changes: Analysis of conservation impact in blue forests projects using Sentinel-2 satellite imagery', *Forest Ecology and Management,* vol. 561, pp. 1-11, doi: doi.org/10.1016/j.foreco.2024.121920.

Fatnassi, S, Yahia, M, Ali, T & Mortula, M 2023, 'Polarimetric SAR characterization of mangrove forest environment in the United Arab Emirates (UAE)', *International Journal of Advanced Computer Science and Applications*, vol. 14, pp. 685-691, doi: doi.org/10.14569/IJACSA.2023.0140380.

Fatoyinbo, T, Fedliciano, EA, Lagomasino, D, Lee, SK & Tretting, C 2018, 'Estimating mangrove aboveground biomass from airborne LiDAR data: A case study from the Zambezi River delta', *Environmental Research Letters,* vol. 13, pp. 1-12, doi: doi.org/10.1088/1748-9326/aa9f03.

Fatoyinbo, TE & Simard, M 2013, 'Height and biomass of mangroves in Africa from ICESat/GLAS and SRTM', *International Journal of Remote Sensing,* vol. 34, pp. 668-681, doi: doi.org/10.1080/01431161.2012.712224.

Fatoyinbo, TE, Simard, M, Allen, RAW & Shugart, HH 2008, 'Landscape-scale extent, height, biomass, and carbon estimation of Mozambique's mangrove forests with Landsat ETM+ and shuttle RADAR topography mission elevation data', *Journal of Geophysical Research,* vol. 113, pp. 1-13, doi: doi.org/10.1029/2007JG000551.

Feliciano, EA, Wdowinski, S, Potts, MD, Lee, SK & Fatoyinbo, TE 2017, 'Estimating mangrove canopy height and above-ground biomass in the Everglades National Park with airborne LiDAR and TanDEM-X data', *Remote Sensing*, vol. 9, pp. 1-14, doi: doi.org/10.3390/rs9070702.

Friess, DA, Rogers, K, Lovelock, CE, Krauss, KW, Hamilton, SE, Lee, SY, Lucas, R, Primavera, J, Rajkaran, A & Shi, S 2019, 'The state of the world's mangrove forests: Past, present, future', *Annual Review of Environment and Resources,* vol. 44, pp. 89-115, doi: doi.org/10.1146/annurev-environ-101718-033302.

Fu, B, Liang, Y, Lao, Z, Sun, X, Li, S, He, H, Sun, W & Fan, D 2023, 'Quantifying scattering characteristics of mangrove species from optuna-based optimal machine learning classification using multi-scale feature selection and SAR image time series', *International Journal of Applied Earth Observation and Geoinformation*, vol. 122, doi: doi.org/10.1016/j.jag.2023.103446.

Fu, W & Wu, Y 2011, 'Estimation of aboveground biomass of different mangrove trees based on canopy diameter and tree height', *Procedia Environmental Sciences,* vol. 10, pp. 2189-2194, doi: doi.org/10.1016/j.proenv.2011.09.343.

Fu, Y, Yang, G, Wang, J, Song, X & Feng, H 2014, 'Winter wheat biomass estimation based on spectral

indices, band depth analysis and partial least squares regression using hyperspectral measurements', *Computers and Electronics in Agriculture,* vol. 100, pp. 51-59, doi: doi.org/10.1016/j.compag.2013.10.010.

Gao, J 2009, *Digital Analysis of Remotely Sensed Imagery,* McGraw-Hill, NY, USA.

Ghosh, SM & Behera, MD 2021, 'Aboveground biomass estimates of tropical mangrove forest using Sentinel-1 SAR coherence data - the superiority of deep learning over a semi-empirical model', *Computers and Geosciences,* vol. 150, pp. 1-12, doi: doi.org/10.1016/j.cageo.2021.104737.

Giri, C, Ochieng, E, Tieszen, LL, Zhu, Z, Singh, A, Loveland, T, Masek, J & Duke, N 2010, 'Status and distribution of mangrove forest of the world using Earth observation satellite data', *Global Ecology and Biogeography,* vol. 20, pp. 154-159, doi: doi.org/10.1111/j.1466-8238.2010.00584.x.

Gitelson, AA, Gritz, Y & Merzlyak, MN 2003, 'Relationships between leaf chlorophyll content and spectral reflectance and algorithms for non-destructive chlorophyll assessment in higher plant leaves', *Journal of Plant Physiology*, vol. 160, pp. 271-282, doi: doi.org/10.1078/0176-1617-00887.

Goldberg, L, Lagomasino, D, Thomas, N & Fatoyinbo, T 2020, 'Global declines in human driven mangrove loss', *Global Change Biology,* vol. 26, pp. 5844-5855, doi: doi.org/10.1111/gcb.15275.

Hamdan, O, Aziz, HK & Hasmadi, IM 2014, 'L-band ALOS PALSAR for biomass estimation of matang mangroves, Malaysia', *Remote Sensing of Environment,* vol. 155, pp. 69-78, doi: doi.org/10.1016/j.rse.2014.04.029.

Hamdan, O, Khairunnisa, Ammar, AA, Hasmadi, IM & Aziz, HK 2013, 'Mangrove carbon stock assessment by optical satellite imagery', *Journal of Tropical Forest Science,* vol. 25, pp. 554-565, url: http://www.jstor.org/stable/23616997.

Harrell, PA, Chavez, LLB, Kasischke, ES, French, NHF & Christensen, NL 1995, 'Sensitivity of ERS-1 and JERS-1 RADAR data to biomass and stand structure in Alaskan boreal forest', *Remote Sensing of Environment,* vol. 54, pp. 247-260, doi: doi.org/10.1016/0034-4257(95)00127-1.

Hidayatullah, MF, Kamal, M & Wicaksono, P 2023, 'Species-based aboveground mangrove carbon stock estimation using WorldView-2 image data', *Remote Sensing Applications: Society and Environment,* vol. 30, pp. 1-13, doi: doi.org/10.1016/j.rsase.2023.100959.

Hirata, Y, Tabuchi, R, Patanaponpaiboon, P, Poungparn, S, Yoneda, R & Fujioka, Y 2014, 'Estimation of aboveground biomass in mangrove forests using high-resolution satellite data', *Journal of Forest Research,* vol. 19, pp. 34-41, doi: doi.org/10.1007/s10310-013-0402-5.

Hirosawa, Y, Marsh, SE & Kliman, DH 1996, 'Application of standardized principal component analysis to land-cover characterization using multitemporal AVHRR data', *Remote Sensing of Environment,* vol. 58, pp. 267-281, doi: doi.org/10.1016/S0034-4257(96)00068-5.

Hu, T, Zhang, YY, Su, Y, Zheng, Y, Lin, G & Guo, Q 2020, 'Mapping the global mangrove forest aboveground biomass using multisource remote sensing data', *Remote Sensing,* vol. 12, pp. 1-18, doi: doi.org/10.3390/rs12101690.

Huong, KM, Hernández, DIR & Tuan, NT 2023, 'Mapping the above-ground biomass of Rhizophora Apiculata plantation forests using PlanetScope imagery in Thanh Phu Nature Reserve, Vietnam', *Biological Bulletin,* vol. 50, pp. 450-461, doi: doi.org/10.1134/S1062359023601957.

Hutchings, P, Kingsford, M & Guldberg, OH 2019, The Great Barrier Reef: Biology, Environment and Management, 2nd edn, CSIRO Publishing, Melbourne, Australia.

Islam, MA, Biilah, MM, Idris, MH, Bhuiyan, MKA & Kamal, AHM 2024, 'Mangroves of Malaysia: A comprehensive review on ecosystem functions, services, restorations, and potential threats of climate change', *Hydrobiologia,* vol. 851, pp. 1841-1871, doi: doi.org/10.1007/s10750-023-05431-z.

Jaramillo, F, Brown, I, Castellazzi, P, Espinosa, L, Guittard, A, Hong, SH & Monroy, VHR & Wdowinski, S 2018, 'Assessment of hydrologic connectivity in an ungauged wetland with InSAR observations', *Environmental Research Letters,* vol. 13, pp. 1-11, doi: doi.org/10.1088/1748-9326/aa9d23.

Jia, M, Wang, Z, Mao, D, Ren, C, Song, K, Zhao, C, Wang, C, Xiao, X & Wang, Y 2023, 'Mapping global distribution of mangroves forests at 10-m resolution', *Science Bulletin,* vol. 68, pp. 1306-1316, doi: doi.org/10.1016/j.scib.2023.05.004.

Jin, X, Li, Z, Feng, H, Ren, Z & Li, S 2020, 'Deep neural network algorithm for estimating maize biomass based on simulated Sentinel 2A vegetation indices and leaf area index', *The Crop Journal,* vol. 8, pp. 87-97, doi: doi.org/10.1016/j.cj.2019.06.005.

Joetzjer, E, Pillet, M, Ciais, P, Barbier, N, Chave, J, Schlund, M, Maignan, F, Barichivich, J, Luyssaert, S, Hérault, B, Poncet, FV & Poulter, B 2017, 'Assimilating satellite-based canopy height within an ecosystem model to estimate aboveground forest biomass', *Geophysical Research Letters,* vol. 44, pp. 6823-6832, doi: doi.org/10.1002/2017GL074150.

Jones, AR, Segaran, RR, Clarke, KD, Waycott, M, Goh, WSH & Gillanders, BM 2020, 'Estimating mangrove tree biomass and carbon content: A comparison of forest inventory techniques and drone imagery', *Frontiers in Marine Science,* vol. 6, pp. 1-13, doi: doi.org/10.3389/fmars.2019.00784.

Joshi, N, Mitchard, ETA, Woo, N, Torres, J, Rocek, JM, Ehammer, A, Collins, M, Jepsen, MR & Fesholt, R 2015, 'Mapping dynamics of deforestation and forest degradation in tropical forests using RADAR satellite data', *Environmental Research Letters*, vol. 10, pp. 1-13, doi: doi.org/10.1088/1748-9326/10/3/034014.

Kamal, M, Hidayatullah, MF, Mahyatar, P & Ridha, SM 2022, 'Estimation of aboveground mangrove carbon stocks from WorldView-2 imagery based on generic and species-specific allometric equations', *Remote Sensing Applications: Society and Environment,* vol. 26, pp. 1-9, doi: doi.org/10.1016/j.rsase.2022.100748.

Kamal, M, Sididk, F, Prananda, ARA & Mahardhika, SA 2021, 'Mapping leaf area index of restored mangroves using WorldView-2 imagery in Perancak Estuary, Bali, Indonesia', *Remote Sensing Applications: Society and Environment,* vol. 23, pp. 1-11, doi: doi.org/10.1016/j.rsase.2021.100567.

Khorram, S, Wiele, CFVD, Koch, FH, Nelson, SAC & Potts, MD 2016, *Principles of Applied Remote Sensing,* Springer, NY, USA.

Komiyama, A, Ong, JE & Poungparn, S 2008, 'Allometry, biomass, and productivity of mangrove forests: A review', *Aquatic Botany,* vol. 89, pp. 128-137, doi: doi.org/10.1016/j.aquabot.2007.12.006.

Komiyama, A, Poungparn, S & Kato, S 2005, 'Common allometric equations for estimating the tree weight of mangroves', *Journal of Tropical Ecology*, vol. 21, pp. 471–477.

Konecny, G 2014, *Geoinformation Remote Sensing, Photogrammetry, and Geographic Information Systems,* 2nd edn, CRC Press, FL, USA.

Kumar, S, Siqueira, P, Govil, H & Agrawal, S 2023, *Spaceborne Synthetic Aperture Radar Remote Sensing,* CRC Press, FL, USA.

Lagomasino, D, Fatoyinbo, T, Lee, S, Feliciano, E, Trettin, C & Simard, M 2016, 'A comparison of mangrove canopy height using multiple independent measurements from land, air, and space', *Remote Sensing,* vol. 8, pp. 1-18, doi: doi.org/10.3390/rs8040327.

Lee, SK, Fatoyinbo, TE, Lagomansino, D, Feliciano, E & Trettin, C 2018, 'Multibaseline TanDEM-X magrove height estimation: The selection of the vertical wavenumber', *IEEE Journal of Selected Topics In Applied Earth Observations And Remote Sensing,* vol. 11, pp. 3434-3442, doi: doi.org/10.1109/JSTARS.2018.2835647.

Li, M, Im, J, Quackenbush, J & Liu, T 2014, 'Forest biomass and carbon stock quantification using airborne LiDAR data: A case study over Huntington Wildlife Forest in the Adirondack Park', *IEEE Journal of Selected Topics in Applied Earth Observations and Remote Sensing,* vol. 7, pp. 3143-3156, doi: doi.org/10.1109/JSTARS.2014.2304642.

Li, S, Zhu, Z, Deng, W, Zhu, Q, Xu, Z, Peng, B, Guo, F, Zhang, Y & Yang, Z 2024, 'Estimation of aboveground biomass of different vegetation types in mangrove forests based on UAV remote sensing', *Sustainable Horizons,* vol. 11, pp. 1-8, doi: doi.org/10.1016/j.horiz.2024.100100.

Liao, H, Wdowinski, S & Li, S 2020, 'Regional-scale hydrological monitoring of wetlands with Sentinel-1 InSAR observations: Case study of the South Florida Everglades', *Remote Sensing of Environment,* vol. 251, pp. 1-14, doi: doi.org/10.1016/j.rse.2020.112051.

Liu, JG & Mason, PJ 2016, *Image processing and GIS for remote Sensing Techniques and applications,* 2nd edn, John Wiley & Sons, Inc, West Sussex, UK.

Liu, T, Yang, T, Zhu, S, Mou, N, Zhang, W, Wu, W, Zhao, Y, Yao, Z, Sun, J, Chen, C, Sun, C & Zhang, Z 2024, 'Estimation of wheat biomass based on phenological identification and spectral response', *Computers and Electronics in Agriculture,* vol. 222, pp. 1-15, doi: doi.org/10.1016/j.compag.2024.109076.

Liu, Y & Zhu, X 2024, 'Tracking mangrove light use efficiency using normalized difference red edge index', *Ecological Indicators*, vol. 168, pp. 1-11, doi: doi.org/10.1016/j.ecolind.2024.112774.

Lu, D, Chen, Q, Wang, G, Moran, E, Batistella, M, Zhang, M, Laurin, GV & Saah, D 2012, 'Aboveground forest biomass estimation with Landsat and LiDAR data and uncertainty analysis of the estimates', *International Journal of Forestry Research,* vol. 2012, pp. 1-16, doi: doi.org/10.1155/2012/436537.

Lucas RM, Mitchell, AL, Rosenqvist, A, Proisy, C, Melius, A & Ticehurst, C 2007, 'The potential of L-band SAR for quantifying mangrove characteristics and change: Case studies from the tropics', *Aquatic Conservation: Marine And Freshwater Ecosystems,* vol. 17, pp. 245-264, doi: doi.org/10.1002/aqc.833.

Lucas, RM, Cronin, N, Lee, A, Moghaddam, M, Witte, C & Tickle, P 2006, 'Empirical relationships between AIRSAR backscatter and LiDAR-derived forest biomass, Queensland, Australia', *Remote Sensing of Environment,* vol. 100, pp. 407-425, doi: doi.org/10.1016/j.rse.2005.10.019.

Lucas, RM, Kerchove, RVD, Otero, V, Lagomasino, D, Fatoyinbo, L, Omar, H, Satyanarayana, B & Guebas, FD 2020, 'Structural characterisation of mangrove forests achieved through combining multiple sources of remote sensing data', *Remote Sensing of Environment,* vol. 237, pp. 1-14, doi: doi.org/10.1016/j.rse.2019.111543.

Luckman, A, Baker, J, Kuplich, TM, Tanasse, CDCF & Frery, AC 1997, 'A study of the backscatter and biomass for relationship regenerating spaceborne SAR between RADAR tropical forest instruments', *Remote Sensing of Environment,* vol. 60, pp. 1-13, doi: doi.org/10.1016/S0034-4257(96)00121-6.

Mahasani, I, Osawa, T & Adnyana, IW 2021, 'Estimation and mapping of above ground biomass of mangrove forest using ALOS-2 PALSAR-2 in Benoa Bay, Bali, Indonesia', *Journal of Environmental Science,* vol. 15, pp. 75-89, doi: doi.org/10.24843/EJES.2021.v15.i01.p07.

Mai, X, Li, Q, Xu, W, Deng, S, Wang, W, Wu, W, Zhang, W & Wang, Y 2025, 'Estimation of Mangrove Aboveground carbon using integrated UAV-LiDAR and satellite data', *Sustainability*, vol. 17, pp. 1-29, doi: doi.org/10.3390/su17188211.

Malik, A, Rahim, A, Jalil, AR, Amir, MF, Arif, DS, Rizal, M, Husain, J, William, DR & Jihad, N 2023, 'Mangrove blue carbon stocks estimation in South Sulawesi Indonesia', *Continental Shelf Research,* vol. 269, pp. 1-9, doi: doi.org/10.1016/j.csr.2023.105139.

Mandal, D, Bhattacharya, A & Rao, YS 2021, *Radar Remote Sensing for Crop Biophysical Parameter Estimation,* Springer, Gateway East, Singapore.

Mandal, D, Kumar, V, Ratha, D, Dey, S, Battacharya, A, Sanchez, JML, McNairn, H & Rao, YS 2020, 'Dual polarimetric RADAR vegetation index for crop growth monitoring using Sentinel-1 SAR data', *Remote Sensing of Environment*, vol. 147, doi: doi.org/10.1016/j.rse.2020.111954.

Mandal, MSH, Suwa, R, Rollon, R, Albano, GMG, Cruz, GAA, Ono, K, Tirol, YHP, Blanco, AC & Nadaoka, K 2024, 'Aboveground biomass estimation of an old-growth mangrove forest using airborne LiDAR in the Philippines', *Ecological Research,* vol. 40, pp. 1-13, doi: doi.org/10.1111/1440-1703.12503.

Marcone, A, Impollonia, G, Croci, M, Henri, Blandinières, H & Amaducci, S 2024, 'Estimation of above ground biomass, biophysical and quality parameters of spinach (Spinacia Oleracea L.) using Sentinel-2 to support the supply chain', *Scientia Horticulturae,* vol. 325, pp. 1-8, doi: doi.org/10.1016/j.scienta.2023.112641.

Mather, PM & Koch, M 2011, *Computer Processing of Remotely-Sensed Images,* 4th edn, John Wiley & Sons, Inc, West Sussex, UK.

Maurya, K, Mahajan, S & Chaube, N 2021, 'Remote sensing techniques: mapping and monitoring of mangrove ecosystem: A review', *Complex & Intelligent Systems,* vol. 7, pp. 2797-2818, doi: doi.org/10.1007/s40747-021-00457-z.

McFeeters, SK 2013, 'The use of the normalized difference water index (NDWI) in the delineation of open water features', *International Journal of Remote Sensing*, vol. 17, pp. 1425-1432, doi: doi.org/10.1080/01431169608948714.

Naidoo, L, Mathieu, R, Main, R, Kleynhans, W, Wessels, K, Anser, G & Leblon, B 2015, 'Savannah woody structure modelling and mapping using multi-frequency (X-, C- and L-band) synthetic aperture RADAR data', *ISPRS Journal of Photogrammetry and Remote Sensing,* vol. 105, pp. 234-250, doi: doi.org/10.1016/j.isprsjprs.2015.04.007.

Nandy, S, Srinet, R & Padalia, H 2021, 'Mapping forest height and aboveground biomass by integrating ICESat-2, Sentinel-1 and Sentinel-2 data using random forest algorithm in Northwest Himalayan Foothills of India', *Geophysical Research Letters,* vol. 48, pp. 1-10, doi: doi.org/10.1029/2021GL093799.

Nesha, MK, Hussin, YA Leeuwen, LMV, L & Sulistioadi, YB 2020, 'Modeling and mapping aboveground biomass of the restored mangroves using ALOS-2 PALSAR-2 in East Kalimantan, Indonesia', *International Journal of Applied Earth Observation and Geoinformation,* vol. 91, pp. 1-9, doi: doi.org/10.1016/j.jag.2020.102158.

Neto, MM, Silva, JBD & Brito, HCD 2024, 'Carbon stock estimation in a Brazilian mangrove using optical satellite data', *Environmental Monitoring and Assessment,* vol. 196, pp. 1-16, doi: doi.org/10.1007/s10661-023-12151-3.

Nguyen, HH & Nguyen, TTH 2021, 'Above-ground biomass estimation models of mangrove forests based on remote sensing and field-surveyed data: Implications for C-PFES implementation in Quang Ninh Province, Vietnam', *Regional Studies in Marine Science,* vol. 48, pp. 1-17, doi: doi.org/10.1016/j.rsma.2021.101985.

Ningthoujam, RK, Balzter, H, Tansey, K, Feldpausch, TR Mitchard, ETA, Wani, AA, Joshi, PK 2017, 'Relationships of S-band RADAR backscatter and forest aboveground biomass in different forest types', *Remote Sensing*, vol. 9, pp. 1-17, doi: doi.org/10.3390/rs9111116.

Oehmcke, S, Li, L, Trepekli, K, Revenga, JC, Larsen, TN, Gieseke, F & Igel, C 2024, 'Deep point cloud regression for above-ground forest biomass estimation from airborne LiDAR', *Remote Sensing of Environment,* vol. 302, pp. 1-21, doi: doi.org/10.1016/j.rse.2023.113968.

Ovejero, RJ, Elghout, A, Navarro, CJ, Martín MPR, Jiménez, MN, Navarro, FB, Segura, DA & Castro, J 2023, 'Estimation of aboveground biomass and carbon stocks of Quercus ilex L. saplings using UAV-derived RGB imagery', *Annals of Forest Science,* vol. 80, pp. 1-14, doi: doi.org/10.1186/s13595-023-01210-x.

Pan, T, Ye, H, Zhang, X, Liao, X, Wang, D, Bayin, D, Safarov, M, Okhonniyozov, M & Majid, G 2024, 'Estimating aboveground biomass of grassland in central Asia mountainous areas using unmanned aerial vehicle vegetation indices and image textures– a case study of typical grassland in Tajikistan', *Environmental and Sustainability Indicators,* vol. 22, pp. 1-10, doi: doi.org/10.1016/j.indic.2024.100345.

Pandey, HP, Bhandari, SK & Harrison, S 2022, 'Comparison among allometric models for tree biomass estimation using non-destructive trees'

data', *International Society for Tropical Ecology,* vol. 63, pp. 263-272, doi: doi.org/10.1007/s42965-021-00210-0.

Patnaik, S, Yang, XS & Sethi, IK 2021, *Advances in Machine Learning and Computational Intelligence Proceedings of ICMLCI 2019*, Springer, Singapore.

Peng, C, Song, Y, Huang, Q, Niu, Z, Zeng, G, Kang, H & Ying, M 2025, 'Estimating coastal mangrove aboveground biomass of Zhejiang province based on Sentinel-2 images and multiple machine learning algorithms', *Frontiers in Forests and Global Change,* vol. 8, pp. 1-16, doi: doi.org/10.3389/ffgc.2025.1662546.

Pham, TD, Le, NN, Ha, NT, Nguyen, LV, Xia, J, Yokoya, N, To, TT, Trinh, HX, Kieu, LQ & Takeuchi, W 2020a, 'Estimating mangrove above-ground biomass using extreme gradient boosting decision trees algorithm with fused Sentinel-2 and ALOS-2 PALSAR-2 data in Can Gio Biosphere Reserve, Vietnam', *Remote Sensing,* vol. 12, pp. 1-20, doi: doi.org/10.3390/rs12050777.

Pham, TD, Yokoya, N, Bui, DT, Yoshino, K & Friess, DA 2019, 'Remote sensing approaches for monitoring mangrove species, structure, and biomass: Opportunities and challenges', *Remote Sensing,* vol. 11, pp. 1-24, doi: doi.org/10.3390/rs11030230.

Pham, TD, Yokoya, N, Xia, J, Ha, NT, Le, NN, Nguyen, TTT, Dao, TH, Vu, TTP, Pham, TD & Takeuchi, W 2020b, 'Comparison of machine learning methods for estimating mangrove above-ground biomass using multiple source remote sensing data in the Red River Delta Biosphere Reserve, Vietnam', *Remote Sensing,* vol. 12, pp. 1-17, doi: doi.org/10.3390/rs12081334.

Pham, TD, Yoshino, K & Bui, DT 2017, 'Biomass estimation of Sonneratia caseolaris (l.) Engler at a coastal area of Hai Phong city (Vietnam) using ALOS-2 PALSAR imagery and GIS-based multi-layer perceptron neural networks', *GIScience & Remote Sensing,* vol. 54, pp. 329-353, doi: doi.org/10.1080/15481603.2016.1269869.

Pham, TD, Yoshino, K, Le, NN & Bui, DT 2018, 'Estimating aboveground biomass of a mangrove plantation on the Northern coast of Vietnam using machine learning techniques with an integration of ALOS-2 PALSAR-2 and Sentinel-2A data', *International Journal of Remote Sensing,* vol. 39, pp. 7761-7788, doi: doi.org/10.1080/01431161.2018.1471544.

Pohl, C & Genderen, JV 2017, *Remote Sensing Image Fusion: A Practical Guide*, CRC Press, FL, USA.

Pour, AB, Parsa, M & Eldosouky, AM 2023, *Geospatial Analysis Applied to Mineral Exploration Remote Sensing, GIS, Geochemical and Geophysical Applications to Mineral Resources*, Elsevier, Amsterdam, Netherlands.

Purwanto, AD, Wikantika, K, Darmawan, S & Deliar A 2023, 'Predicting the Distribution of Mangrove Forests through Random Forest Algorithm by Combining Spectral Features and DEM Data', *IOP Conf. Series: Earth and Environmental Science*, vol. 1276, pp. 1-12, doi: doi.org 10.1088/1755-1315/1276/1/012002.

Quang, NH, Quinn, CH, Carrie, R, Stringer, LC, Hue, LTV, Hackney, CR & Tan, DV 2022, 'Comparisons of regression and machine learning methods for estimating mangrove above-ground biomass using multiple remote sensing data in the Red River Estuaries of Vietnam', *Remote Sensing Applications: Society and Environment,* vol. 26, pp. 1-17, doi: doi.org/10.1016/j.rsase.2022.100725.

Rahman, MM, Lagomasino, D, Lee, SK, Fatoyinbo, T, Ahmed, I & Kanzaki, M 2019, 'Improved assessment of mangrove forests in Sundarbans east wildlife sanctuary using WorldView 2 and TanDEM-X high resolution imagery', *Remote Sensing in Ecology and Conversation,* vol. 5, pp. 136-149, doi: doi.org/10.1002/rse2.105.

Raja, AR 2016, 'Principal component analysis based assessment of trees outside forests in satellite images', *Indian Journal of Science and Technology,* vol. 91, pp. 1-6, doi: doi.org/10.17485/ijst/2016/v9iS1/107824.

Rakotomavo, A 2018, 'Aboveground biomass estimation of Avicennia Marina (Forssk) Vierh and Rhizophora Mucronata Lam in the Mangoky Delta, SW Madagascar', *American Journal of Plant Sciences,* vol. 9, pp. 1894-1910, doi: doi.org/10.4236/ajps.2018.99137.

Raney, RK, Cahill, JTS, Patterson, GW, & Bussey, DBJ 2012, 'The m-chi decomposition of hybrid dual-polarimetric radar data with application to lunar craters', *Journal of Geophysical Research*, vol. 117, pp. 1-8, doi: doi.org/10.1029/2011JE003986.

Ranson, KJ, Sun, G, Weishampel, JF & Knox, RG 1997, 'Forest biomass from combined ecosystem and RADAR backscatter modeling', *Remote Sensing of Environment,* vol. 59, pp. 118-133, doi: doi.org/10.1016/S0034-4257(96)00114-9.

Ren, H & Zhou, G 2014, 'Estimating aboveground green biomass in desert steppe using band depth indices', *Biosystems Engineering,* vol. 127, pp. 67-78, doi: doi.org/10.1016/j.biosystemseng.2014.08.014.

Richards, JA 2022, *Remote Sensing Digital Image Analysis,* 6th edn, Springer, Cham, Switzerland.

Richards, JA 2009, *Remote Sensing with Imaging Radar,* Springer, Heidelberg, Germany.

Richards, JA 2013, *Remote Sensing with Imaging Radar,* Springer, Heidelberg, Germany.

Riquelme, L, Rumpff, L, Duncan, DH & Vesk, PA 2024, 'Comparing grass biomass estimation methods for management decisions in a semi-arid landscape',

Applied Vegetation Science, vol. 27, pp. 1-12, doi: doi.org/10.1111/avsc.12792.

Roy, AD, Arachchige, PSP, Watt, MS, Kale, A, Davies, M, Heng, JE, Daneil, R, Galgamuwa, GAB, Moussa, LG, Timsina, K, Ewane, EB, Rogers, K, Hendy, I, Jones, AE, Miguel, SD, Burt, JA, Ali, T, Sidik, F, Abdullah, M, Selvam, PP, Jaafar, WSWM, Alawatte, I, Doaemo, W, Cardil, A & Mohan, M 2024, 'Remote sensing-based mangrove blue carbon assessment in the Asia-Pacific: A systematic review', *Science of the Total Environment,* vol. 938, pp. 1-17, doi: doi.org/10.1016/j.scitotenv.2024.173270.

Ruan, L, Yan, M, Zhang, L, Fan, X & Yang, H 2022, 'Spatial-temporal NDVI pattern of global mangroves: A growing trend during 2000–2018', *Science of The Total Environment*, vol. 844, pp. 1-10, doi: doi.org/10.1016/j.scitotenv.2022.157075.

Saatchi, S, Marlier, M, Chazdon, RL, Clark, DB & Russel, AE 2011, 'Impact of spatial variability of tropical forest structure on radar estimation of aboveground biomass', *Remote Sensing of Environment*, vol. 115, pp. 2836-2849, doi: doi.org/10.1016/j.rse.2010.07.015.

Saim, AA & Aly, MH 2025, 'Machine learning and multisensor data fusion for forest above ground biomass estimation in Arkansas', *Earth Systems and Environment*, pp. 1-18, doi: doi.org/10.1007/s41748-025-00713-z.

Sainuddin, FV, Chirakkal, S, Asok, SV, Das, AK & Putrevu, D 2023, 'Evaluation of multifrequency SAR data for estimating tropical above-ground biomass by employing radiative transfer modeling', *Environmental Monitoring and Assessment,* vol. 1952, pp. 1-21, doi: doi.org/10.1007/s10661-023-11715-7.

Samra, RMA, Almazroui, M, Li, W & Askary, HE 2025, 'Monitoring mangrove dynamics and evaluating future afforestation potential in the Egyptian Red Sea', *Environmental and Sustainability Indicators*, vol. 26, pp. 1-14, doi: doi.org/10.1016/j.indic.2025.100705.

Sanam, H, Thomas, AA, Kumar, AP & Lakshmanan, G 2024, 'Multi-sensor approach for the estimation of above-ground biomass of mangroves', *Journal of the Indian Society of Remote Sensing,* vol. 52, pp. 903-916, doi: doi.org/10.1007/s12524-024-01811-7.

Santoro, M, Cartus, O & Wegmüller, U 2020, 'Estimation of forest above-ground biomass with C-band scatterometer backscatter observations', *IEEE International Geoscience and Remote Sensing Symposium, (IGARSS), Waikoloa, HI, USA,* pp. 4987-4990, doi: doi.org/10.1109/IGARSS39084.2020.9323600.

Santoro, M, Cartus, O, Wegmüller, Besnard, S, Carvalhais, N, Araza, A, Herold, M, Liang, J, Cavlovic & Engdahl, ME 2022, 'Global estimation of above-ground biomass from spaceborne C-band scatterometer observations aided by LiDAR metrics of vegetation structure', *Remote Sensing of Environment,* vol. 279, pp. 1-23, doi: doi.org/10.1016/j.rse.2022.113114.

Selvaraj, JJ & Pérez, BEG 2023a, 'An enhanced approach to mangrove forest analysis in the Colombian Pacific coast using optical and SAR data in Google Earth Engine', *Remote Sensing Applications: Society and Environment,* vol. 30, pp. 1-15, doi: doi.org/10.1016/j.rsase.2023.100938.

Selvaraj, JJ & Pérez, BEG 2023b, 'Estimating mangrove aboveground biomass in the Colombian Pacific coast: A multisensor and learning approach', *Heliyon,* vol. 9, pp. 1-17, doi: doi.org/10.1016/j.heliyon.2023.e20745.

Silva, CA, Saatchi, S, Garcia, M, Labriere, N, Klauberg, C, Ferraz, A, Meyer, V, Jeffery, KJ, Abernethy, White, L, Zhao, K, Lewis, SL & Hudak, AT 2018, 'Comparison of small- and large-footprint lidar characterization of tropical forest aboveground structure and biomass: A case study from Central Gabon', *IEEE Journal of Selected Topics in Applied Earth Observations and Remote Sensing*, vol. 11, pp. 3512-3526, doi: doi.org/10.1109/JSTARS.2018.2816962.

Simard, M, Zhang, K, Monroy, R, Victor, H, Ross, MS, Ruiz, PL, Castañeda, ME, Twilley, RR & Rodriguez, E 2006, 'Mapping height and biomass of mangrove forests in Everglades National Park with SRTM Elevation data', *Photogrammetric Engineering and Remote Sensing,* vol. 72, pp. 299-311, doi: doi.org/10.14358/PERS.72.3.299.

Singh, SG, Vennila, A, Singh, R, Bharti, VS, Shukla, SP & Purushothaman, CS 2023, 'Standing carbon stock of Thane Creek mangrove ecosystem: An integrated approach using allometry and remote sensing techniques', *Regional Studies in Marine Science,* vol. 67, pp. 1-11, doi: doi.org/10.1016/j.rsma.2023.103207.

Small, D 2011, 'Flattening Gamma: Radiometric Terrain Correction for SAR Imagery', *IEEE Transactions on Geoscience and Remote Sensing*, vol. 49. no. 8, pp. 3081- 3093, doi: doi.org/10.1109/TGRS.2011.2120616.

Srivastava, PK, Gupta, DK, Islam, T, Han, D & Prasad R 2022, *Radar Remote Sensing Applications and Challenges,* Elsevier, Oxford, UK.

Stankovic, M, Mishra, AK, Rahayu, YP, Lefcheck, J, Murdiyarso, D, Friess, DA, Corkalo, M, Vukovic, T, Vanderklift, MA, Farooq, SH, Espitia, JDG & Prathep, A 2023, 'Blue carbon assessments of seagrass and mangrove ecosystems in South and Southeast Asia: Current progress and knowledge gaps', *Science of the Total Environment,* vol. 904, pp. 1-16, doi: doi.org/10.1016/j.scitotenv.2023.166618.

Stovall, AEL & Shugart, HH 2018a, 'Improved biomass calibration and validation with terrestrial LiDAR: Implications for future LiDAR and SAR missions', *IEEE Journal of Selected Topics in Applied Earth Observations and Remote Sensing,* vol. 11, pp.

3527-3537, doi: doi.org/10.1109/JSTARS.2018.2803110.

Stovall, AEL, Fatoyinbo, T, Thomas, NM, Armoston, J, Ebanega, MO, Simard, M, Trettin, C, Zogo, RVO, Aken, IA, Debina, M, Kemoe, AMM, Assoumou, EO, Kim, JS, Lagomasino, D, Lee, SK, Obame, JCN, Voubou, GD & Essono, CZ 2021, 'Comprehensive comparison of airborne and spaceborne SAR and LiDAR estimates of forest structure in the tallest mangrove forest on Earth', *Science of Remote Sensing,* vol. 4, pp. 1-18, doi: doi.org/10.1016/j.srs.2021.100034.

Stovall, AEL, Teixeira, KJA & Shugart, HH 2018b, 'Assessing terrestrial laser scanning for developing non-destructive biomass allometry', *Forest Ecology and Management,* vol. 427, pp. 217-229, doi: doi.org/10.1016/j.foreco.2018.06.004.

Su, Y, Mura, M, Zheng, X, Chen, Q, Wei, X, Qiu, X, Li, M & Ren, Y 2024, 'More accurately estimating aboveground biomass in tropical forests with complex forest structures and regions of high-aboveground biomass', *JGR Biogeosciences,* vol. 129, pp. 1-19, doi: doi.org/10.1029/2023JG007864.

Suardana, AP, Anggraini, N, Aziz, K, Nandika, MR, Ulfa, A, Wijaya, AD, As-syakur, AR, Winarso, G, Prasetio, W, Dimyati, RD 2022, 'Biomass estimation model and carbon dioxide sequestration for mangrove forest using Sentinel-2 In Benoa Bay, Bali', *International Journal of Remote Sensing and Earth Sciences,* vol. 19, pp. 91-100, doi: doi.org/10.30536/j.ijreses.2022.v19.a3797.

Sudiana, D, Nisa, J, Rizkinia, M, Dimyati, RD, Anggraini, N, Riyanto, I, Prabuwono, AS & Sumantyo, JTS 2024, 'Monitoring the distribution of mangrove area using synthetic aperture radar (SAR) and optic remote sensing data fusion based on deep Learning in Kotabaru Regency, Indonesia', *Evergreen,* vol. 11, pp. 536-546, doi: doi.org/10.5109/7172320.

Sullivan, M 2017, *Statistics: Informed Decisions Using Data,* 5th edn, Pearson Education Limited, Essex, UK.

Suwa, R, Rollon, R, Sharma, S, Yoshikai, M, Albano, GMG, Ono, K, Adi, NS, Ati, RNA, Kusumaningtyas, MA, Kepel, TL, Maliao, RJ, Tirol, YHP, Blanco, AC & Nadaoka, K 2021, 'Mangrove biomass estimation using canop height and wood density in the South East and East Asian Regions, Estuarine', *Estuarine, Coastal and Shelf Science,* vol. 248, pp. 1-9, doi: doi.org/10.1016/j.ecss.2020.106937.

Szigarski, C, Jagdhuber, T, Baur, M, Thiel, C, Parrens, M, Wigneron, JP, Piles, M & Entekhabi, D 2018, 'Analysis of the RADAR vegetation index and potential improvements', *Remote Sensing*, vol. 10, pp. 1-15, doi: doi.org/10.3390/rs10111776.

Taloor, AK, Manhas, DS & Kothyari, GC 2021, 'Retrieval of land surface temperature, normalized difference moisture index, normalized difference water index of the Ravi basin using Landsat data',

Applied Computing and Geosciences, vol. 9, pp. 1-11, doi: doi.org/10.1016/j.acags.2020.100051.

Tanase, MA, Panciera, R, Lowell, K, Hacker, J & Walker, JP 2013, 'Estimation of forest biomass from L-band polarimetric decomposition components', *IEEE International Geoscience and Remote Sensing Symposium, (IGARSS), Melbourne, VIC, Australia,* pp. 949-952, doi: doi.org/10.1109/IGARSS.2013.6721318.

TERN 2025, *New maps reveal mangrove change since 80s*, Terrestrial Ecosystem Research Network - TERN, viewed 10 Oct 2025, <https://www.tern.org.au/news/new-maps-reveal-mangrove-change-since-80s/>.

Thinley, J, Pickiering, C & Ndehedehe, C 2024, 'Using vegetation and chlorophyll indices to model above ground biomass over time in an urban arboretum in subtropical queensland', *Remote Sensing Applications: Society and Environment,* vol. 34, pp. 1-12, doi: doi.org/10.1016/j.rsase.2024.101202.

Tian, S, Zhang, X, Jie, Tian, J & Sun, Q 2016, 'Random forest classification of wetland landcovers from multi-sensor data in the arid region of Xinjiang, China', *Remote Sensing* vol. 8, no. 11, pp. 1-14, doi: doi.org/10.3390/rs8110954.

Thomas, N, Bunting, P, Lucas, R, Hardy, A, Rosenqvist, A & Fatyinbo, T 2018, 'Mapping mangrove extent and change: A globally applicable approach', *Remote Sensing,* vol. 10, pp. 1-20, doi: doi.org/10.3390/rs10091466.

Thomas, N, Lucas, R, Bunting, P, Hardy, A, Rosenqvist, A & Simard, M 2017, 'Distribution and drivers of global mangrove forest change 1996-2010', *PLOS ONE,* vol. 6, pp. 1-14, doi: doi.org/10.1371/journal.pone.0179302.

Thomas, N, Lucas, R, Itoh, T, Simard, M, Fatoyinbo, L, Bunting, P & Rosenqvist, A 2015, 'An approach to monitoring mangrove extents through timeseries comparison of JERS-1 SAR and ALOS PALSAR data', *Wetlands Ecology and Management,* vol. 23, pp. 3-17, doi: doi.org/10.1007/s11273-014-9370-6.

Tran P, Gritcan, I, Cusens, J, Alfaro, AC & Leuzinger, S 2017, 'Biomass and nutrient composition of temperate mangroves (Avicennia Marina var. Australasic) in New Zealand', *New Zealand Journal of Marine and Freshwater Research,* vol. 51, pp. 427-442, doi: doi.org/10.1080/00288330.2016.1260604.

Tran, TV, Reef, R & Zhu, X 2022, 'A review of spectral indices for mangrove remote sensing', *Remote Sensing,* vol. 14, pp. 1-29, doi: doi.org/10.3390/rs14194868 .

Vaghela, B, Chirakkal, S, Putrevu, D & Solanki, H 2021, 'Modelling above ground biomass of Indian mangrove forest using dual-pol SAR data', *Remote Sensing Applications: Society and Environment,* vol. 21, pp. 1-12, doi: doi.org/10.1016/j.rsase.2020.100457.

Veiga, PR, Wheeler, J, Louis V, Tansey, K & Balzter, H 2017, 'Quantifying Forest Biomass Carbon Stocks From Space', *Current Forestry Reports*, vol. 3, pp. 1-18, doi: doi.org/10.1007/s40725-017-0052-5.

Vinh, TV, Marchand, C, Linh, TVK, Vinh, DD & Allenbash, M 2019, 'Allometric models to estimate above-ground biomass and carbon stocks in Rhizophora Apiculata tropical managed mangrove forests (Southern Vietnam)', *Forest Ecology and Management,* vol. 434, pp. 131-141, doi: doi.org/10.1016/j.foreco.2018.12.017.

Wang, C, Zhang, W, Ji, Y, Marino, A, Li, C, Wang, L, Zhao, H & Wang, M 2024, 'Estimation of aboveground biomass for different forest types using data from Sentinel-1, Sentinel-2, ALOS PALSAR-2, and GEDI', *Forests,* vol. 15, pp. 1-8, doi: doi.org/10.3390/f15010215.

Wang, M, Cao, W, Guan, Q, Wu, G & Wang, F 2018, 'Assessing changes of mangrove forest in a coastal region of Southeast China using multi-temporal satellite images', *Estuarine Coastal and Shelf Science,* vol. 207, pp. 283-292, doi: doi.org/10.1016/j.ecss.2018.04.021.

Wang, S, Liu, C, Li, W, Jia, S & Yue, H 2023, 'Hybrid model for estimating forest canopy heights using fused multimodal space borne LiDAR data and optical imagery', *International Journal of Applied Earth Observation and Geoinformation,* vol. 122, pp. 1-20, doi: doi.org/10.1016/j.jag.2023.103431.

Wei, X 2010, 'Biomass estimation: A remote sensing approach', *Geography Compass,* vol. 4, pp. 1635-1647, doi: doi.org/10.1111/j.1749-8198.2010.00352.x.

Wicaksono, P, Danoedoro, P, Hartono, & Nehren, U. 2015, 'Mangrove biomass carbon stock mapping of the Karimunjawa Islands using multispectral remote sensing', *International Journal of Remote Sensing*, vol. 37, pp. 26–52. doi: doi.org/10.1080/01431161.2015.1117679.

Wong, CJ, James, D, Besar, NA, Kamlun, KU, Tangah, J, Tsuyuki, S & Phua, MH 2020, 'Estimating mangrove above-ground biomass loss due to deforestation in Malaysian Northern Borneo between 2000 and 2015 using SRTM and Landsat images', *Forests,* vol. 11, pp. 1-15, doi: doi.org/10.3390/f11091018.

Wu, C, Shen, P, Tebaldini, S, Liao, M & Zhang, L 2025, 'InSAR-based estimation of forest above-ground biomass using phase histogram technique', *International Journal of Applied Earth Observation and Geoinformation,* vol. 136, pp. 1-14, doi: doi.org/10.1016/j.jag.2024.104350.

Ximenes, AC, Cavanaugh, KC, Arvor, D, Murdiyarso, D, Thomas, N, Arcoverde, GFB, Bispo, PDC & Stocken, TVD 2023, 'A comparison of global mangrove maps: Assessing spatial and bioclimatic discrepancies at poleward range limits', *Science of the Total Environment,* vol. 860, pp. 1-11, doi: doi.org/10.1016/j.scitotenv.2022.160380.

Xu, Z, Du, W, Zhou, G, Qin, L, Meng, S, Yu, J, Sun, Z, SiQing, B & Liu, Q 2022, 'Aboveground biomass allocation and additive allometric models of fifteen tree species in northeast China based on improved investigation methods', *Forest Ecology and Management*, vol. 505, pp.1-19, doi: doi.org/10.1016/j.foreco.2021.119918.

Yamaguchi, Y 2020, *Polarimetric SAR Imaging: Theory and Applications*, CRC Press, FL, USA.

Yin, H, Udelhoven, T, Fensholt, R, Pflugmacher, D & Hostert, P 2012, 'How normalized difference vegetation index (NDVI) trendsfrom advanced very high resolution radiometer (AVHRR) and système probatoire d'observation de la terre vegetation (SPOT VGT) time series differ in agricultural areas: An inner Mongolian case study, *Remote Sensing*, vol. 4, pp. 3364-3389, doi: doi.org/10.3390/rs4113364.

Yonezawa, C, Watanabe, M & Saito, G 2012, 'Polarimetric decomposition analysis of ALOS PALSAR observation data before and after a landslide event', *Remote Sensing,* vol. 4, pp. 2314-2328, doi: doi.org/10.3390/rs4082314.

Younes, K, Amine, S, El Sawda, CE, Zahab, SE, Arayro, J, Mezher, R, Halwani, J, Ouddane, B & Hanna, EG 2025, 'Principal component analysis of biomass-derived carbon aerogels: Unveiling key performance factors for supercapacitor applications', *Sustainability,* vol. 17, pp. 1-13, doi: doi.org/10.3390/su17104530.

Zanvo, SMG, Menash, S, Salako, KV & Kakaï, RG 2023, 'Tree height-diameter, aboveground and belowground biomass allometries for two west African mangrove species', *Biomass and Bioenergy,* vol. 176, pp. 1-11, doi: doi.org/10.1016/j.biombioe.2023.106917.

Zhang, H, Wang, C, Zhu, J, Fu, H, Han, W & Xie, H 2023, 'Forest aboveground biomass estimation in subtropical mountain areas based on improved water cloud model and PolSAR decomposition using L-band PolSAR data', *Forests,* vol. 14, pp. 1-17, doi: doi.org/10.3390/f14122303.

Zhang, Y, Xia, C, Zhang, X, Cheng, X, Feng, G, Wang, Y & Gao, Q 2021, 'Estimating the maize biomass by crop height and narrowband vegetation indices derived from UAV-based hyperspectral images', *Ecological Indicators,* vol. 129, pp. 1-12, doi: doi.org/10.1016/j.ecolind.2021.107985.

Zhou, X & Li, C 2023, 'Mapping the vertical forest structure in a large subtropical region using airborne LiDAR data', *Ecological Indicators,* vol. 154, pp. 1-15, doi: doi.org/10.1016/j.ecolind.2023.110731.

Zhu, X, Xue, Z, Qian, S & Sun, C 2025, 'Estimating aboveground biomass of mangrove forests in Indonesia using spatial attention coupled bayesian aggregator', *Forests,* vol. 16, pp. 1-6, doi: doi.org/10.3390/f16081296.

Zhu, Y, Liu, K, Liu, L, Myint, SW, Wang, S, Cao, J & Wu, Z 2020, 'Estimating and mapping mangrove biomass dynamic change using WorldView-2 images and digital surface models', *IEEE Journal of Selected Topics in Applied Earth Observations and Remote Sensing,* vol. 13, pp. 2123-2134, doi: doi.org/10.1109/JSTARS.2020.2989500.

APPENDICES

Appendix A 1-1: AGB Estimation from LIDAR

Appendix A 1-2: AGB Estimation from Sentinel-2

Appendix A 1-3: AGB Estimation from ALOS-1 PALSAR

Fusion Approaches

Fusion 4m
ALOS-2 PLASAR + Pléiades Neo

RGB : 4 2 8
NIR Green L HV

Fusion 4m
ALOS-2 PLASAR + Pléiades Neo

RGB : 5 2 8
RedEdge Green L HV

Mangrove Biomass from Space

Spatial Reference
Projection : WGS 1984 UTM Zone 54S
WKID : 32754
Linear Unit : Meters

N

Description

The main aim of this research was to assess the capacity of satellite data to study mangrove aboveground biomass – AGB in South Australia. Mapping and quantitative assessment of above ground biomass (AGB) of mangroves may be possible using multiple remote sensing datasets such as optical, RADAR and LiDAR data supported by fieldwork. This study assessed South Australian (SA) mangroves (Avicennia marina) in the St Kilda area near Salisbury.

Author : Bassam Waheed
Date :   10 October 2025
Credits : ESRI, University of Flinders.

1 0.5 0   1   2   3
KM

Esri, TomTom, FAO, NOAA, USGS,
Esri, USGS

Appendix A 1-4: Fusion Approaches

Mangrove Extent (RT Classification)

Pléiades Neo
RGB : 1 2 3
Resolution : 1.3m

Pléiades Neo
Random Trees - RT Classification

Date : 02-11-2023

Mangroves

Mangrove Biomass from Space

Spatial Reference
Projection : WGS 1984 UTM Zone 54S
WKID : 32754
Linear Unit : Meters

N

Description

The main aim of this research was to assess the capacity of satellite data to study mangrove aboveground biomass – AGB in South Australia. Mapping and quantitative assessment of above ground biomass (AGB) of mangroves may be possible using multiple remote sensing datasets such as optical, RADAR and LiDAR data supported by fieldwork. This study assessed South Australian (SA) mangroves (Avicennia marina) in the St Kilda area near Salisbury.

Author : Bassam Waheed
Date : 10 October 2025
Credits : ESRI, University of Flinders.

1   0.5   0   1   2   3 KM

Appendix A 1-5: Mangrove Extent (RT Classification)

Appendix B 1-1: Detailed Workflow chart
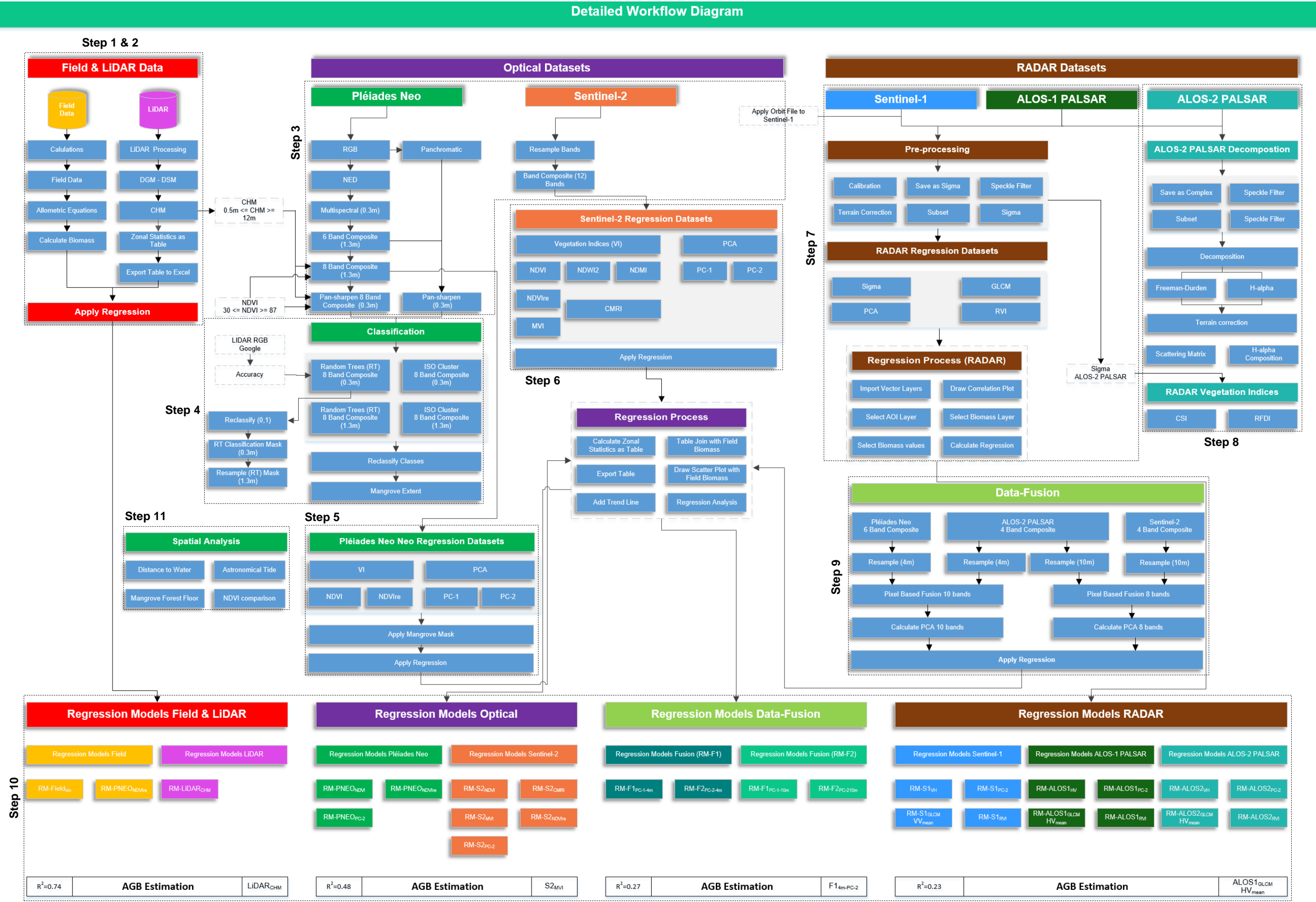
Appendix C 1-1: Mangrove Survey Points for St Kilda

Table 1: Field data heights and biomass values

Plot	x	y	Height mean (cm)	Biomass (t_c_ha)
1935a	276682	6148139	571	91.89
1949a	276929	6148376	471	76.11
1959a	277004	6148491	388	67.02
1969a	277030	6148580	343	58.78
1979a	277156	6148934	303	44.59
1987a	277305	6148943	235	30.53
1997a	276853	6149815	144	21.03
2005a	276856	6149859	150	13.94
Pre1930a	276271	6148039	564	85.41
1936c	275988	6148986	457	83.17
1949c	276446	6149050	527	85.73
1969c	276650	6149292	270	53.30
1979c	276645	6149437	215	41.06
1987c	276797	6149524	84	21.04
1997c	276776	6149918	106	22.23
Pre1930c	275861	6148960	627	136.82
1936d	277216	6147701	424	104.32
1949d	277377	6147769	396	97.14
1959d	277368	6148002	324	66.67
1969d	277488	6148124	178	23.67
1979d	277401	6148612	226	56.98
1997d	277087	6149380	109	34.47
2005d	277225	6149421	102	21.47
Pre1930d	276883	6147339	653	130.46
1959e	277546	6147955	425	69.25
1987e	277517	6148525	161	15.07

Appendix C 1-2: Ground Truth Survey Report for LiDAR$_{CHM}$

Introduction

A field survey was conducted on 07-March 2025 in St Kilda area to verify LiDAR$_{CHM}$ heights in the field. In Table-1 various features (mangroves, building and tree) are given along with their LiDAR$_{Heights}$ and staff height measurements. In Figure 1, photographs and LiDAR data are displayed for each sample point.

Table 1: Field points and features heights

Point Id	Feature type	Staff height	CHM height
1000	mangroves	5.5	5.36
1002	mangroves	3.8	3.73
1012	tree	5.99	5.61
2003	mangroves	5.40	5.48
2004	building	3.05	2.49

Imagery	LiDAR$_{CHM}$	Photograph
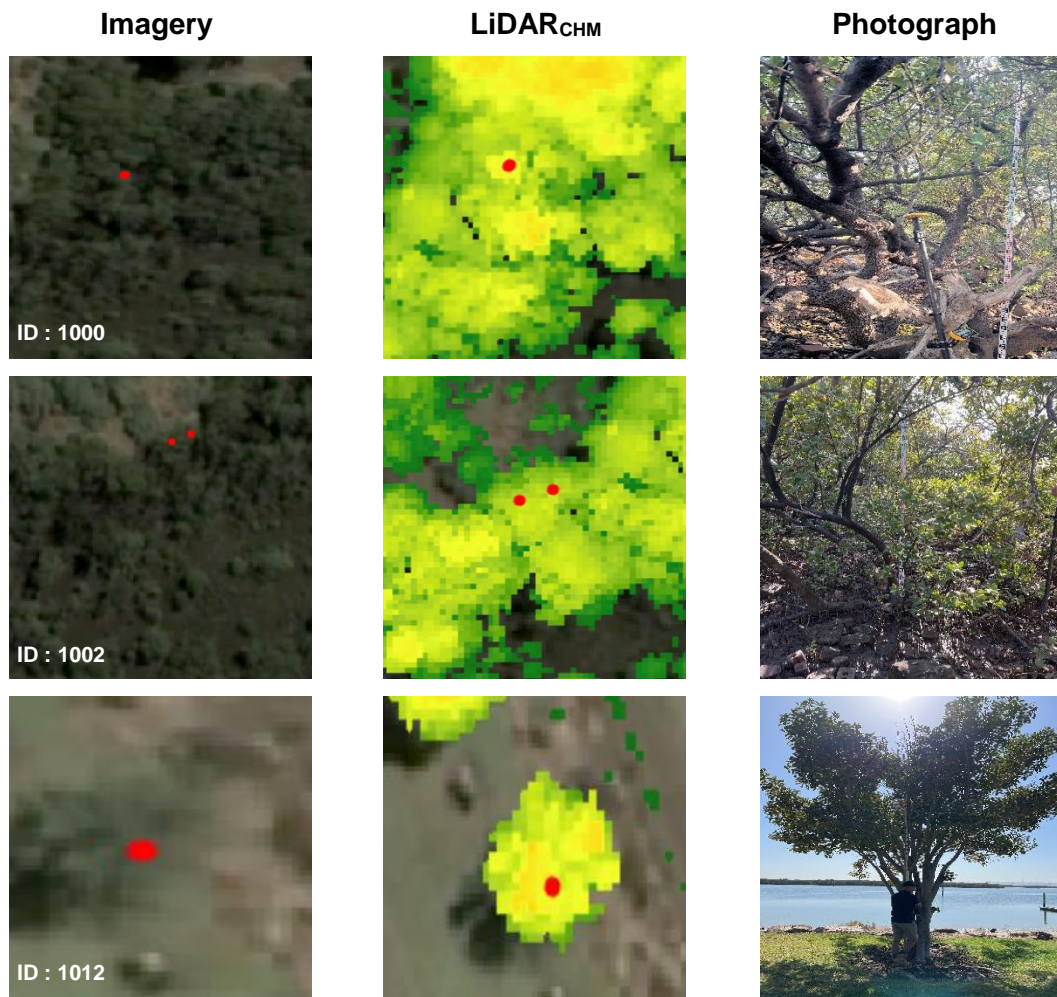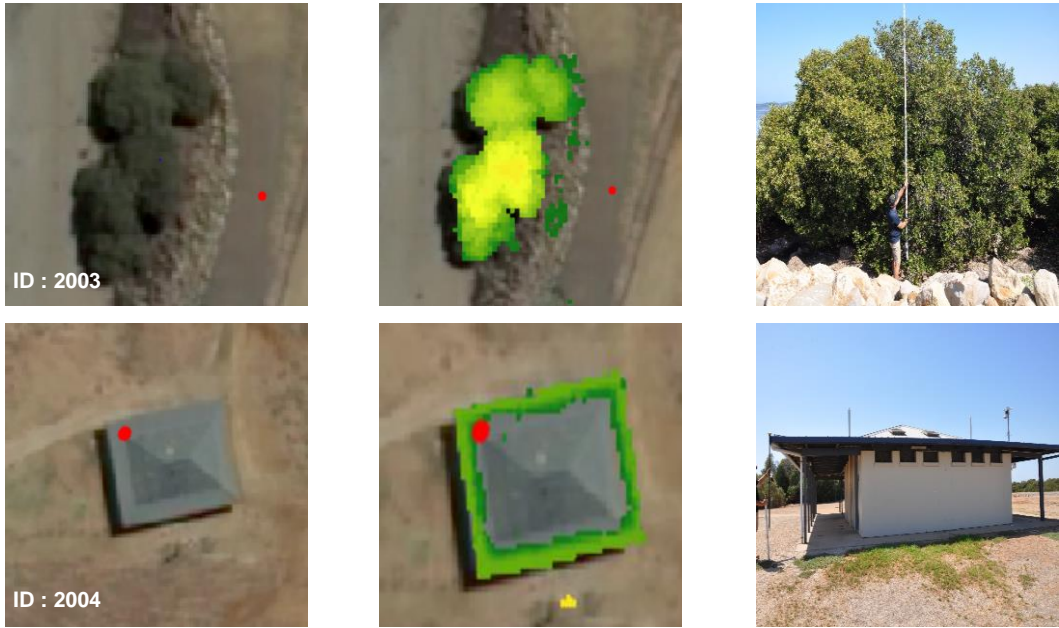
Figure-1: Field smple points for LiDAR hieghts with each photographs

Appendix C 1-3: Mangrove Field Photographs

Appendix D 1-1: ALOS-1 PALSAR Regression Plots
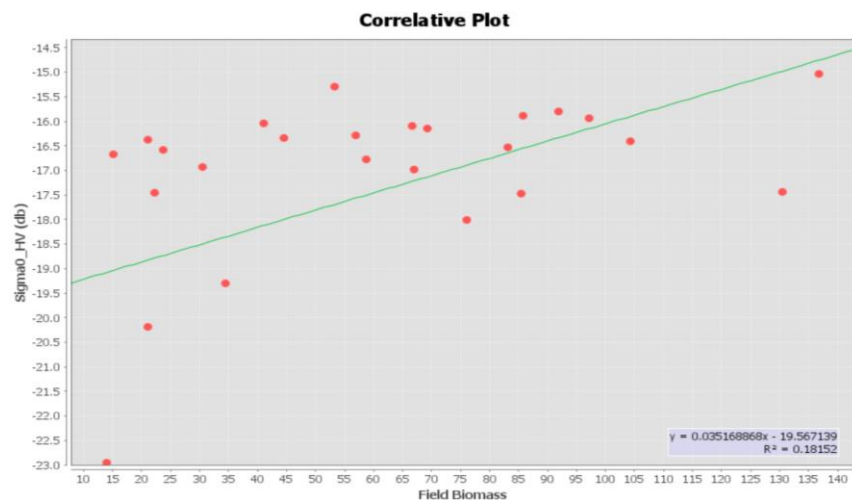
Figure 1: Scatterplot between ALOS-1 PALSAR$_{HV}$ and field$_{Biomass}$
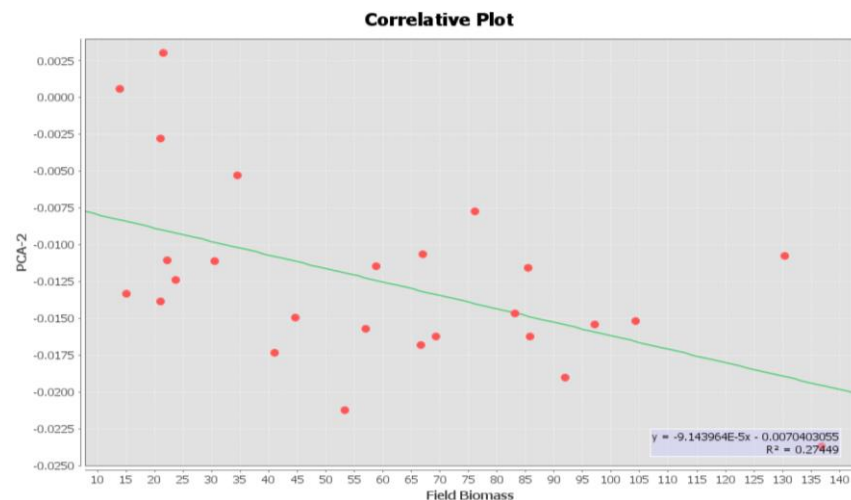
Figure 2: Scatterplot between ALOS-1 PALSAR$_{PCA-2}$ and field$_{Biomass}$
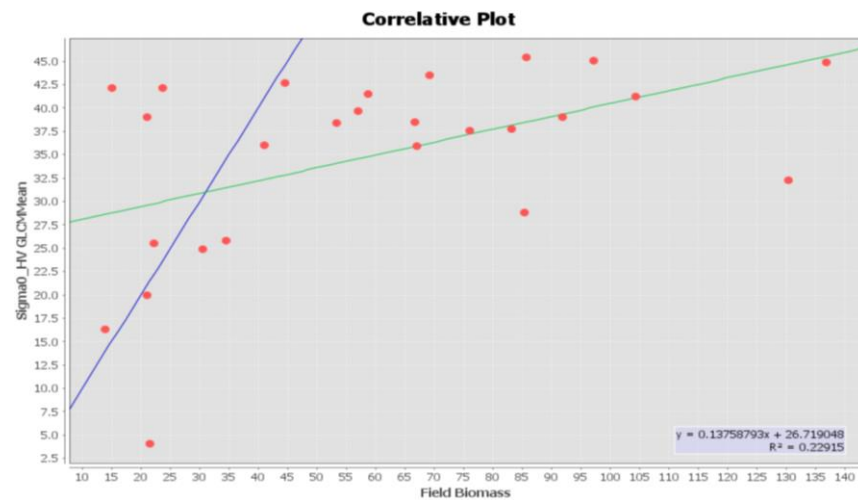
Figure 3: Scatterplot between ALOS-1 PALSAR$_{GLCM-mean}$ and field$_{Biomass}$
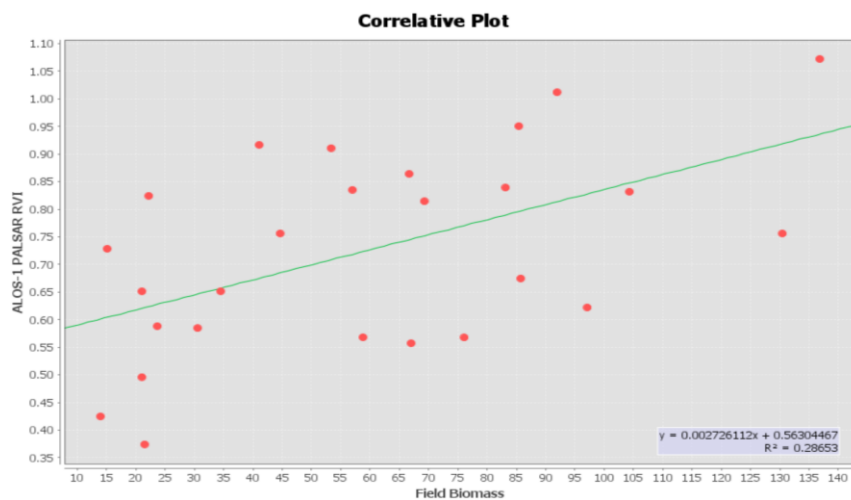
Figure 4: Scatterplot between ALOS-1 PALSAR$_{RVI}$ and field$_{Biomass}$

Appendix D 1-2: ALOS-2 PALSAR Regression Plots
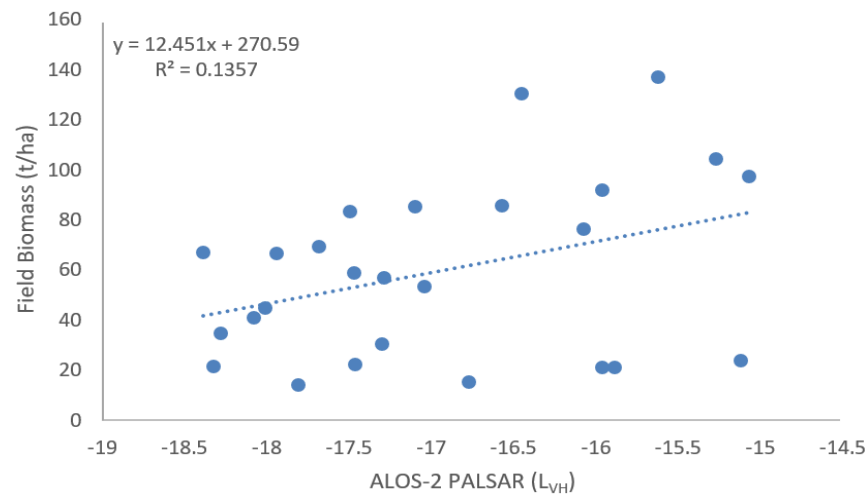
Figure 5: Scatterplot between ALOS-2 PALSAR$_{VH}$ and field$_{Biomass}$
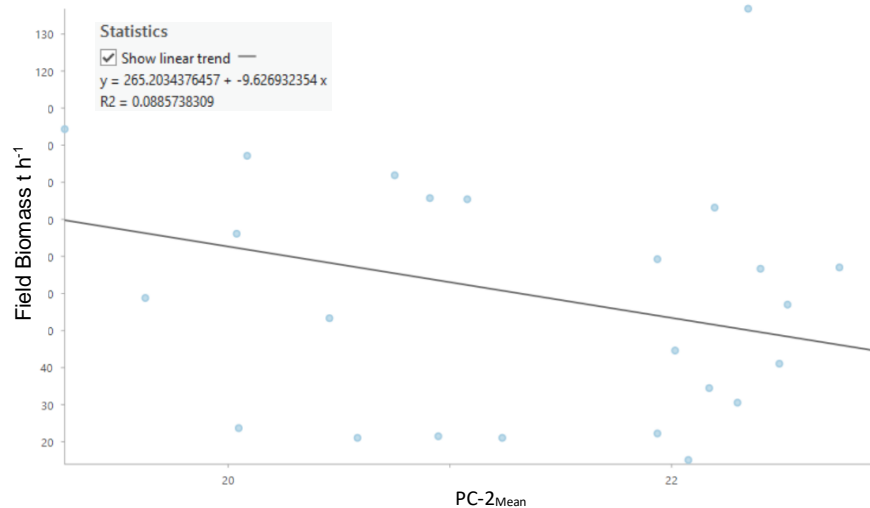
Figure 6: Scatterplot between ALOS-2 PALSAR$_{PC-2}$ and field$_{Biomass}$
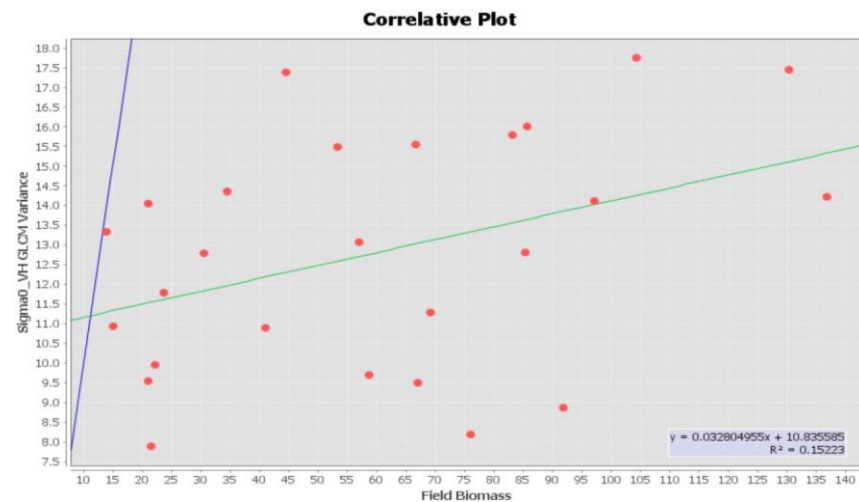
Figure 7: Scatterplot between ALOS-2 PALSAR$_{GLCM-VH-variance}$ and field$_{Biomass}$
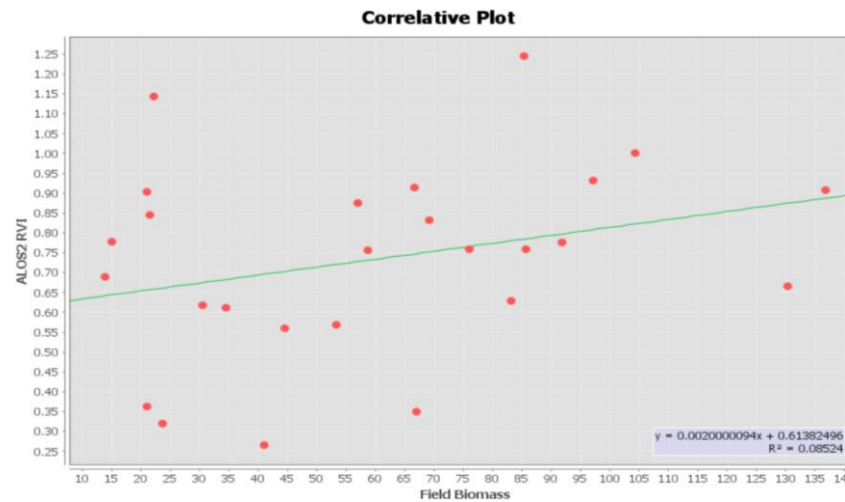
Figure 8: Scatterplot between ALOS-2 PALSAR$_{RVI}$ and field$_{Biomass}$

Appendix D 1-3: Sentinel-1 Regression Plots
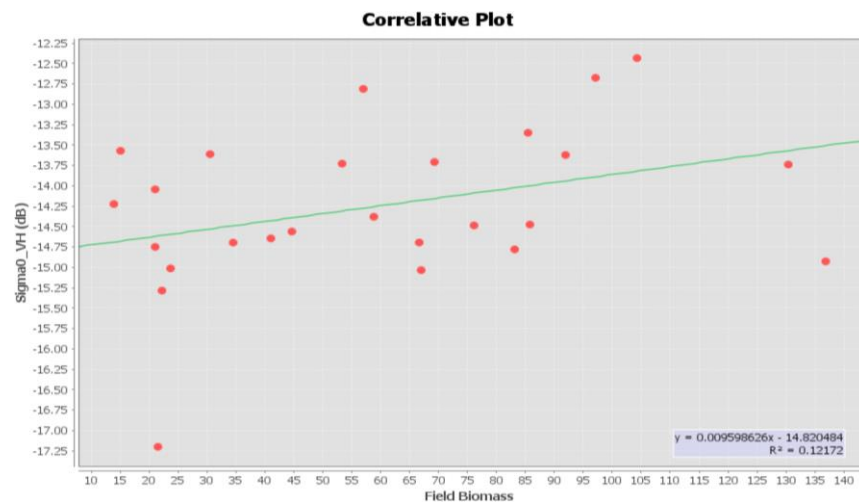
Figure 9: Scatterplot between Sentinel-1$_{VH}$ and field$_{Biomass}$
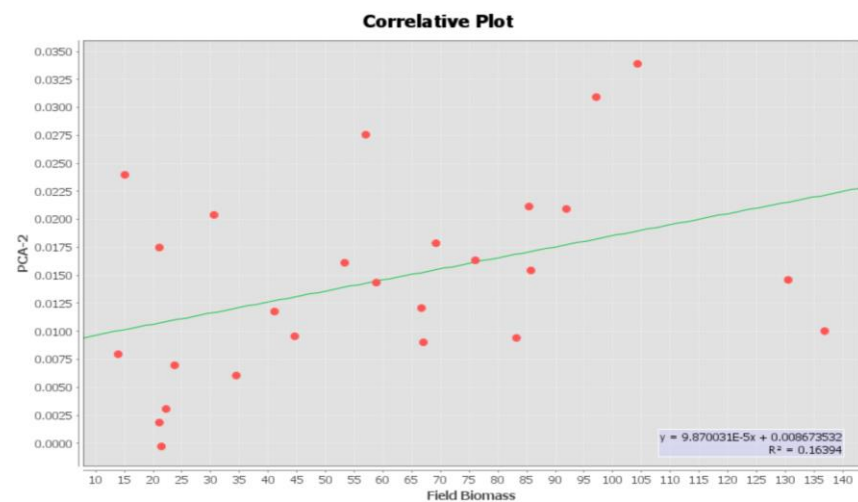
Figure 10: Scatterplot between Sentinel-1$_{PCA-2}$ and field$_{Biomass}$
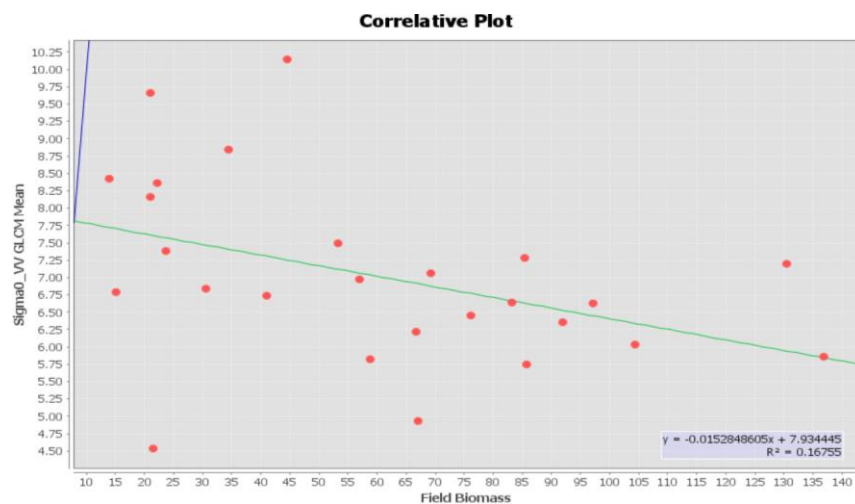
Figure 11: Scatterplot between Sentinel-1$_{GLCM-mean}$ and field$_{Biomass}$
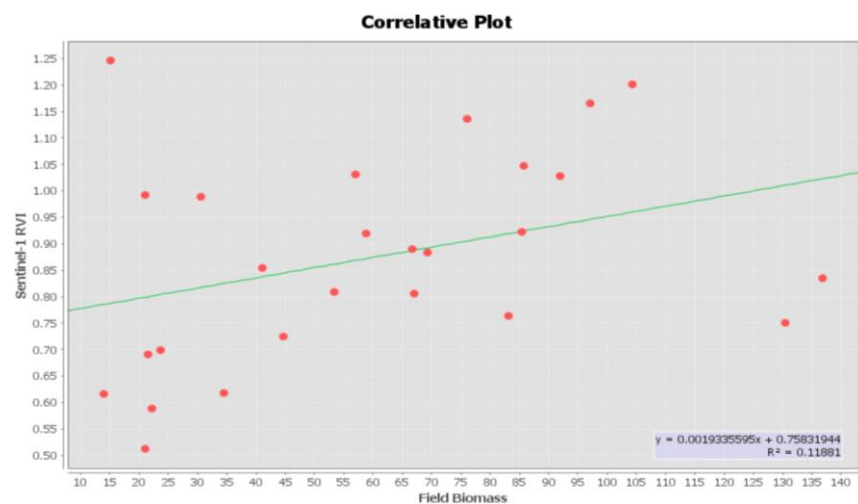
Figure 12: Scatterplot between Sentinel-1$_{RVI}$ and field$_{Biomass}$

Appendix – E

Appendix E 1-1: Pléiades Neo PCA Results

```
# Data file produced by Principal Components
#       Input raster(s):
#               E:\2__St__Kilda\st_kilda\mang_st_kilda.gdb\PLNeo__Composite__6b
#       The number of components = 6
#       Output raster(s):
#               E:\2__St__Kilda\st_kilda_optical\st_kilda_optical.gdb\PLNeo__PCA


#                   COVARIANCE MATRIX

#     Layer         1            2            3            4            5            6
#     ----------------------------------------------------------------------
        1       1.103638e+06  9.340620e+05  7.866856e+05  9.463455e+05  1.112541e+06  6.847665e+05
        2       9.340620e+05  8.371730e+05  7.148781e+05  7.486363e+05  9.181798e+05  6.259333e+05
        3       7.866856e+05  7.148781e+05  6.297332e+05  6.032060e+05  7.578016e+05  5.529977e+05
        4       9.463455e+05  7.486363e+05  6.032060e+05  1.382146e+06  1.259601e+06  5.195818e+05
        5       1.112541e+06  9.181798e+05  7.578016e+05  1.259601e+06  1.300072e+06  6.616305e+05
        6       6.847665e+05  6.259333e+05  5.529977e+05  5.195818e+05  6.616305e+05  4.996301e+05
# ======================================================================


#                   CORRELATION MATRIX

#     Layer         1            2            3            4            5            6
#     ----------------------------------------------------------------------
        1         1.00000      0.97175      0.94365      0.76623      0.92879      0.92216
        2         0.97175      1.00000      0.98457      0.69596      0.88011      0.96782
        3         0.94365      0.98457      1.00000      0.64656      0.83752      0.98587
        4         0.76623      0.69596      0.64656      1.00000      0.93966      0.62525
        5         0.92879      0.88011      0.83752      0.93966      1.00000      0.82093
        6         0.92216      0.96782      0.98587      0.62525      0.82093      1.00000
# ======================================================================


#                   EIGENVALUES AND EIGENVECTORS

# Number of Input Layers    Number of Principal Component Layers
         6                            6
# PC Layer        1            2            3            4            5            6
#     ----------------------------------------------------------------------
# Eigenvalues
            5066531.34291  607595.07831   52339.58385   12959.28674    8794.66216    4172.70509
# Eigenvectors
# Input Layer
        1         0.45400     -0.22839     -0.69746     -0.00037     -0.49225      0.11386
        2         0.38653     -0.34701      0.02504     -0.53352      0.56457      0.35520
        3         0.32552     -0.36771      0.37701     -0.22636     -0.22886     -0.71629
        4         0.45857      0.71478      0.28905     -0.29570     -0.27740      0.17568
        5         0.49719      0.25503     -0.18419      0.51822      0.52379     -0.33305
        6         0.28467     -0.34096      0.50330      0.55509     -0.18779      0.45389
# ======================================================================


#                   PERCENT AND ACCUMULATIVE EIGENVALUES

# PC Layer   EigenValue    Percent of EigenValues    Accumulative of EigenValues
        1  5066531.34291          88.0769                    88.0769
        2   607595.07831          10.5625                    98.6394
        3    52339.58385           0.9099                    99.5493
        4    12959.28674           0.2253                    99.7746
        5     8794.66216           0.1529                    99.9275
        6     4172.70509           0.0725                   100.0000
# ======================================================================
```

Appendix – E

Appendix E 1-2: Sentinel-2 PCA Results

```
# Data file produced by Principal Components
#     Input raster(s):
#             E:\2__St__Kilda\2_st_kilda_optical\st_kilda_optical.gdb\sentinel2_12bands
#     The number of components = 12
#     Output raster(s):
#             E:\2__St__Kilda\2_st_kilda_optical\st_kilda_optical.gdb\sentinal2_PCA_20250814


#                 COVARIANCE MATRIX

#   Layer       1            2            3            4            5            6            7            8            9           10           11           12
# --------------------------------------------------------------------------------------------------------------------------------------------------------------
     1     5.649191e+04 6.707550e+04 7.669377e+04 9.789742e+04 9.212247e+04 5.988649e+04 5.236886e+04 5.118652e+04 4.880615e+04 4.687499e+04 9.705515e+04 9.274126e+04
     2     6.707550e+04 1.168413e+05 1.524492e+05 2.161146e+05 2.169855e+05 1.898391e+05 1.912318e+05 2.118197e+05 2.055335e+05 1.969407e+05 2.731018e+05 2.170383e+05
     3     7.669377e+04 1.524492e+05 2.488527e+05 3.934510e+05 4.398330e+05 4.577573e+05 4.876585e+05 5.443931e+05 5.447246e+05 5.398234e+05 6.204544e+05 4.491194e+05
     4     9.789742e+04 2.161146e+05 3.934510e+05 7.013175e+05 8.042209e+05 8.499724e+05 9.151370e+05 1.025776e+06 1.040306e+06 1.044297e+06 1.189481e+06 8.351085e+05
     5     9.212247e+04 2.169855e+05 4.398330e+05 8.042209e+05 9.729153e+05 1.092686e+06 1.191822e+06 1.328953e+06 1.359834e+06 1.366719e+06 1.469558e+06 1.007091e+06
     6     5.988649e+04 1.898391e+05 4.577573e+05 8.499724e+05 1.092686e+06 1.376530e+06 1.527485e+06 1.706370e+06 1.747477e+06 1.754962e+06 1.721576e+06 1.141832e+06
     7     5.236886e+04 1.912318e+05 4.876585e+05 9.151370e+05 1.191822e+06 1.527485e+06 1.704929e+06 1.904764e+06 1.951735e+06 1.961596e+06 1.894405e+06 1.245118e+06
     8     5.118652e+04 2.118197e+05 5.443931e+05 1.025776e+06 1.328953e+06 1.706370e+06 1.904764e+06 2.150614e+06 2.186606e+06 2.196136e+06 2.121923e+06 1.388503e+06
     9     4.880615e+04 2.055335e+05 5.447246e+05 1.040306e+06 1.359834e+06 1.747477e+06 1.951735e+06 2.186606e+06 2.245853e+06 2.259048e+06 2.182347e+06 1.424887e+06
    10     4.687499e+04 1.969407e+05 5.398234e+05 1.044297e+06 1.366719e+06 1.754962e+06 1.961596e+06 2.196136e+06 2.259048e+06 2.309832e+06 2.210697e+06 1.442452e+06
    11     9.705515e+04 2.731018e+05 6.204544e+05 1.189481e+06 1.469558e+06 1.721576e+06 1.894405e+06 2.121923e+06 2.182347e+06 2.210697e+06 2.451727e+06 1.680478e+06
    12     9.274126e+04 2.170383e+05 4.491194e+05 8.351085e+05 1.007091e+06 1.141832e+06 1.245118e+06 1.388503e+06 1.424887e+06 1.442452e+06 1.680478e+06 1.196355e+06
# ============================================================================================================


#                 CORRELATION MATRIX

#   Layer       1            2            3            4            5            6            7            8            9           10           11           12
# --------------------------------------------------------------------------------------------------------------------------------------------------------------
     1      1.00000      0.82561      0.64684      0.49184      0.39295      0.21475      0.16874      0.14685      0.13702      0.12977      0.26079      0.35674
     2      0.82561      1.00000      0.89404      0.75497      0.64357      0.47336      0.42846      0.42256      0.40123      0.37909      0.51026      0.58051
     3      0.64684      0.89404      1.00000      0.94181      0.89388      0.78212      0.74867      0.74415      0.72864      0.71202      0.79433      0.82312
     4      0.49184      0.75497      0.94181      1.00000      0.97360      0.86508      0.83690      0.83524      0.82892      0.82050      0.90712      0.91171
     5      0.39295      0.64357      0.89388      0.97360      1.00000      0.94420      0.92538      0.91874      0.91994      0.91170      0.95151      0.93347
     6      0.21475      0.47336      0.78212      0.86508      0.94420      1.00000      0.99708      0.99174      0.99387      0.98420      0.93712      0.88977
     7      0.16874      0.42846      0.74867      0.83690      0.92538      0.99708      1.00000      0.99473      0.99742      0.98848      0.92658      0.87182
     8      0.14685      0.42256      0.74415      0.83524      0.91874      0.99174      0.99473      1.00000      0.99494      0.98534      0.92409      0.86564
     9      0.13702      0.40123      0.72864      0.82892      0.91994      0.99387      0.99742      0.99494      1.00000      0.99185      0.93003      0.86928
    10      0.12977      0.37909      0.71202      0.82050      0.91170      0.98420      0.98848      0.98534      0.99185      1.00000      0.92897      0.86772
    11      0.26079      0.51026      0.79433      0.90712      0.95151      0.93712      0.92658      0.92409      0.93003      0.92897      1.00000      0.98122
    12      0.35674      0.58051      0.82312      0.91171      0.93347      0.88977      0.87182      0.86564      0.86928      0.86772      0.98122      1.00000
# ============================================================================================================


#                 EIGENVALUES AND EIGENVECTORS

# Number of Input Layers     Number of Principal Component Layers
#        12                        12
# PC Layer       1            2            3            4            5            6            7            8            9           10           11           12
# --------------------------------------------------------------------------------------------------------------------------------------------------------------
# Eigenvalues
           14527043.74722  647826.96901  228504.26456   46812.72591   31868.95970   19094.61656   11109.54118    8998.91357    4032.14972    2684.57975    2492.87236    1790.00769
# Eigenvectors
# Input Layer
     1      0.01447      0.19426      0.22523      0.34403      0.41739      0.27842      0.43740      0.53095      0.03997     -0.15603      0.20507     -0.00224
     2      0.04443      0.27446      0.36039      0.34206      0.11271     -0.27916      0.15944     -0.26979      0.30180      0.35740     -0.51074      0.08538
     3      0.10480      0.27744      0.37897      0.21258      0.03019     -0.28167     -0.13106     -0.34517     -0.52818     -0.13362      0.45162     -0.07654
     4      0.19681      0.40036      0.30884     -0.46602     -0.11691     -0.16193     -0.16508      0.14116      0.50056     -0.37041      0.11471      0.02061
     5      0.24897      0.26207      0.23708     -0.46488     -0.03919      0.43195      0.04515      0.08952     -0.38749      0.47076     -0.14653      0.07491
     6      0.30552     -0.11847      0.16016      0.15822     -0.06426      0.36214     -0.12087     -0.14012     -0.01963     -0.34148     -0.35413     -0.65575
     7      0.33848     -0.22047      0.12899      0.18863     -0.08486      0.30334     -0.08076     -0.18774     -0.00663     -0.32713     -0.09363      0.72650
     8      0.37912     -0.26102      0.14094      0.16364     -0.44606     -0.41884      0.00597      0.56413     -0.16835      0.11140     -0.08822     -0.01687
     9      0.38833     -0.28008      0.04947      0.02494     -0.10060      0.12941      0.25338     -0.27104      0.39952      0.36921      0.53354     -0.15018
    10      0.39190     -0.29235     -0.05179     -0.22939      0.75582     -0.28921     -0.19884      0.03147     -0.05408      0.02779     -0.08049     -0.00584
    11      0.39855      0.33557     -0.53994     -0.07269     -0.06870     -0.17470      0.53838     -0.16393     -0.14184     -0.21575     -0.11445      0.00011
    12      0.26692      0.41677     -0.40665      0.37449      0.02346      0.15136     -0.56748      0.15415      0.12727      0.22711      0.11089      0.01109
# ============================================================================================================


#                 PERCENT AND ACCUMULATIVE EIGENVALUES

# PC Layer    EigenValue    Percent of EigenValues   Accumulative of EigenValues
      1   14527043.74722         93.5282                     93.5282
      2     647826.96901          4.1708                     97.6991
      3     228504.26456          1.4712                     99.1702
      4      46812.72591          0.3014                     99.4716
      5      31868.95970          0.2052                     99.6768
      6      19094.61656          0.1229                     99.7997
      7      11109.54118          0.0715                     99.8712
      8       8998.91357          0.0579                     99.9292
      9       4032.14972          0.0260                     99.9551
     10       2684.57975          0.0173                     99.9724
     11       2492.87236          0.0160                     99.9885
     12       1790.00769          0.0115                    100.0000
# ============================================================================================================
```

Appendix E 1-3: ALOS-2 PALSAR PCA Results

```
# Data file produced by Principal Components
#       Input raster(s):
#               E:\2__St__Kilda\6_st_kilda_Alos-2\st_kilda_Alos-2.gdb\alos2_composite_rec3_sub
#       The number of components = 4
#       Output raster(s):
#               E:\2__St__Kilda\6_st_kilda_Alos-2\st_kilda_Alos-2.gdb\Princip_1


#                   COVARIANCE MATRIX

#     Layer           1             2             3             4
#     --------------------------------------------------------------
      1             15.95039      12.49641      12.37621      11.91670
      2             12.49641      18.60093      17.67704      11.49155
      3             12.37621      17.67704      18.37992      11.31071
      4             11.91670      11.49155      11.31071      12.57199
#     ==============================================================


#                   CORRELATION MATRIX

#     Layer           1             2             3             4
#     --------------------------------------------------------------
      1             1.00000       0.72549       0.72282       0.84153
      2             0.72549       1.00000       0.95603       0.75147
      3             0.72282       0.95603       1.00000       0.74407
      4             0.84153       0.75147       0.74407       1.00000
#     ==============================================================


#                   EIGENVALUES AND EIGENVECTORS

# Number of Input Layers      Number of Principal Component Layers
          4                                 4
# PC Layer           1             2             3             4
#     --------------------------------------------------------------|
# Eigenvalues
                  55.59395       6.91136       2.18674       0.81118
# Eigenvectors
# Input Layer
      1             -0.47058      0.64035       0.60691       0.01305
      2             -0.55065      -0.43952      0.02154       0.70933
      3             -0.54601      -0.44914      0.06567       -0.70416
      4             -0.42098      0.44164       -0.79176      -0.02910
#     ==============================================================

#                   PERCENT AND ACCUMULATIVE EIGENVALUES

# PC Layer   EigenValue   Percent of EigenValues   Accumulative of EigenValues
      1       55.59395          84.8721                    84.8721
      2        6.91136          10.5512                    95.4232
      3        2.18674           3.3384                    98.7616
      4        0.81118           1.2384                   100.0000
#     ==============================================================
```

Appendix – E

Appendix E 1-4: Fusion Model 4m PCA Results

```
# Data file produced by Principal Components
#      Input raster(s):
#            E:\2__St__Kilda\7_st_kilda_fusion\st_kilda_fusion.gdb\f1_fusion_4m_clip
#      The number of components = 10
#      Output raster(s):
#            E:\2__St__Kilda\7_st_kilda_fusion\st_kilda_fusion.gdb\f1_fusion_4m_clip_pca


#                  COVARIANCE MATRIX

#   Layer          1            2            3            4            5            6            7            8            9           10
# -----------------------------------------------------------
      1     9.450059e+05 7.878529e+05 6.640464e+05 7.058659e+05 8.933531e+05 5.688746e+05 2.227270e+05 -9.626990e+04 -9.653491e+04 1.511294e+05
      2     7.878529e+05 7.024173e+05 6.018422e+05 5.270214e+05 7.161903e+05 5.191152e+05 1.393760e+05 -8.820577e+04 -8.817457e+04 1.265861e+05
      3     6.640464e+05 6.018422e+05 5.348986e+05 4.173738e+05 5.884006e+05 4.633972e+05 1.497469e+05 -6.948969e+04 -6.940812e+04 1.363603e+05
      4     7.058659e+05 5.270214e+05 4.173738e+05 1.016943e+06 9.269708e+05 3.438796e+05 8.000708e+05 6.912204e+04 6.637903e+04 3.864500e+05
      5     8.933531e+05 7.161903e+05 5.884006e+05 9.269708e+05 9.970162e+05 5.015076e+05 5.016459e+05 -2.512858e+04 -2.659131e+04 2.599761e+05
      6     5.688746e+05 5.191152e+05 4.633972e+05 3.438796e+05 5.015076e+05 4.149881e+05 1.370113e+05 -5.734378e+04 -5.718274e+04 1.254493e+05
      7     2.227270e+05 1.393760e+05 1.497469e+05 8.000708e+05 5.016459e+05 1.370113e+05 1.700417e+07 1.835101e+06 1.800453e+06 8.488743e+06
      8    -9.626990e+04 -8.820577e+04 -6.948969e+04 6.912204e+04 -2.512858e+04 -5.734378e+04 1.835101e+06 9.099985e+05 7.551551e+05 1.433336e+06
      9    -9.653491e+04 -8.817457e+04 -6.940812e+04 6.637903e+04 -2.659131e+04 -5.718274e+04 1.800453e+06 7.551551e+05 8.789197e+05 1.388520e+06
     10     1.511294e+05 1.265861e+05 1.363603e+05 3.864500e+05 2.599761e+05 1.254493e+05 8.488743e+06 1.433336e+06 1.388520e+06 8.884783e+06
# =================================================================


#                  CORRELATION MATRIX

#   Layer          1            2            3            4            5            6            7            8            9           10
# -----------------------------------------------------------
      1      1.00000      0.96701      0.93400      0.72004      0.92035      0.90841      0.05556     -0.10381     -0.10592      0.05216
      2      0.96701      1.00000      0.98186      0.62357      0.85581      0.96150      0.04033     -0.11033     -0.11222      0.05067
      3      0.93400      0.98186      1.00000      0.56590      0.80572      0.98356      0.04965     -0.09960     -0.10123      0.06255
      4      0.72004      0.62357      0.56590      1.00000      0.92059      0.52935      0.19240      0.07185      0.07021      0.12856
      5      0.92035      0.85581      0.80572      0.92059      1.00000      0.77967      0.12183     -0.02638     -0.02841      0.08735
      6      0.90841      0.96150      0.98356      0.52935      0.77967      1.00000      0.05158     -0.09331     -0.09468      0.06533
      7      0.05556      0.04033      0.04965      0.19240      0.12183      0.05158      1.00000      0.46651      0.46572      0.69062
      8     -0.10381     -0.11033     -0.09960      0.07185     -0.02638     -0.09331      0.46651      1.00000      0.84439      0.50409
      9     -0.10592     -0.11222     -0.10123      0.07021     -0.02841     -0.09468      0.46572      0.84439      1.00000      0.49688
     10      0.05216      0.05067      0.06255      0.12856      0.08735      0.06533      0.69062      0.50409      0.49688      1.00000
# =================================================================


#                  EIGENVALUES AND EIGENVECTORS

# Number of Input Layers     Number of Principal Component Layers
#          10                        10
# PC Layer        1            2            3            4            5            6            7            8            9           10
# -----------------------------------------------------------
# Eigenvalues
            2.291148e+07 3.952984e+06 3.568543e+06 1.109897e+06 5.372838e+05 1.391076e+05 4.431942e+04 1.295061e+04 8.583091e+03 3.996076e+03
# Eigenvectors
# Input Layer
      1      1.462168e-02  4.697133e-01  8.658526e-02 -3.996094e-03 -1.804813e-01 -1.683474e-01 -6.973590e-01  4.357036e-03 -4.947522e-01  8.920775e-02
      2      1.035735e-02  3.932620e-01  8.049769e-02 -2.740203e-02 -3.277082e-01 -1.995050e-04  1.088694e-02 -5.416809e-01  5.527899e-01  3.626306e-01
      3      1.059262e-02  3.311576e-01  7.049173e-02 -3.199037e-02 -3.614322e-01  1.040259e-03  3.889320e-01 -2.205458e-01 -2.192099e-01 -7.110796e-01
      4      4.272420e-02  4.069545e-01  4.307257e-02  2.002844e-01  6.994223e-01  1.721142e-01  3.208668e-01 -2.908849e-01 -2.834359e-01  1.830126e-01
      5      2.834839e-02  4.774293e-01  7.104433e-02  1.016678e-01  2.751622e-01 -1.449469e-04 -1.593320e-01  5.116250e-01  5.357169e-01 -3.256075e-01
      6      9.594601e-03  2.837609e-01  6.139738e-02 -3.007040e-02 -3.467448e-01  1.736963e-01  4.830100e-01  5.581631e-01 -1.850570e-01  4.640993e-01
      7      8.338491e-01  5.826108e-02 -5.435378e-01 -7.116518e-02 -2.780125e-02 -1.436866e-03 -4.813730e-03 -8.567883e-05  2.282688e-03 -3.080007e-04
      8      1.075010e-01 -9.000209e-02  7.552994e-02  6.801935e-01 -1.415765e-01 -7.009082e-01 -1.581213e-02  1.123484e-03  2.044643e-03 -1.400847e-03
      9      1.050408e-01 -8.856130e-02  6.964535e-02  6.686720e-01 -1.415765e-01  7.132370e-01 -1.974109e-02  7.283887e-04  2.562910e-03 -1.666286e-03
     10      5.281584e-01 -1.471070e-01  8.151032e-01 -1.789006e-01  5.477628e-02  2.948013e-03 -1.418184e-04  6.166856e-04  2.587352e-04  2.446514e-05
# =================================================================


#                  PERCENT AND ACCUMULATIVE EIGENVALUES

# PC Layer   EigenValue    Percent of EigenValues   Accumulative of EigenValues
     1   2.291148e+07          70.9572                   70.9572
     2   3.952984e+06          12.2425                   83.1997
     3   3.568543e+06          11.0518                   94.2515
     4   1.109897e+06           3.4374                   97.6889
     5   5.372838e+05           1.6640                   99.3529
     6   1.391076e+05           0.4308                   99.7837
     7   4.431942e+04           0.1373                   99.9209
     8   1.295061e+04           0.0401                   99.9610
     9   8.583091e+03           0.0266                   99.9876
    10   3.996076e+03           0.0124                  100.0000
# =================================================================
```

Appendix – E

Appendix E 1-5: Fusion Model 10m PCA Results

```
# Data file produced by Principal Components
#       Input raster(s):
#               E:\2__St__Kilda\7_st_kilda_fusion\st_kilda_fusion.gdb\f2_composite_10m_clip
#       The number of components = 8
#       Output raster(s):
#               E:\2__St__Kilda\7_st_kilda_fusion\st_kilda_fusion.gdb\f2_composite_10m_PCA


#               COVARIANCE MATRIX

#   Layer          1             2             3             4             5             6             7             8
#  -------------------------------------------------------------------------
       1      6.188556e+05  6.786962e+05  7.864015e+05  6.043541e+05  4.331641e+05 -3.447297e+03 -4.455716e+03  2.793678e+05
       2      6.786962e+05  7.655725e+05  9.009957e+05  7.110782e+05  4.169402e+05 -1.852820e+04 -1.968126e+04  2.643202e+05
       3      7.864015e+05  9.009957e+05  1.133195e+06  1.006707e+06  5.548551e+05 -2.063186e+04 -2.217899e+04  3.066060e+05
       4      6.043541e+05  7.110782e+05  1.006707e+06  1.501422e+06  1.228133e+06  1.862861e+05  1.814993e+05  6.021666e+05
       5      4.331641e+05  4.169402e+05  5.548551e+05  1.228133e+06  1.696333e+07  1.833877e+06  1.798029e+06  8.473878e+06
       6     -3.447297e+03 -1.852820e+04 -2.063186e+04  1.862861e+05  1.833877e+06  9.007983e+05  7.527037e+05  1.442579e+06
       7     -4.455716e+03 -1.968126e+04 -2.217899e+04  1.814993e+05  1.798029e+06  7.527037e+05  8.825156e+05  1.401998e+06
       8      2.793678e+05  2.643202e+05  3.066060e+05  6.021666e+05  8.473878e+06  1.442579e+06  1.401998e+06  8.878386e+06
#  =========================================================================


#               CORRELATION MATRIX

#   Layer          1             2             3             4             5             6             7             8
#  -------------------------------------------------------------------------
       1      1.00000       0.98602       0.93907       0.62697       0.13369      -0.00462      -0.00603       0.11918
       2      0.98602       1.00000       0.96734       0.66324       0.11570      -0.02231      -0.02394       0.10138
       3      0.93907       0.96734       1.00000       0.77179       0.12655      -0.02042      -0.02218       0.09666
       4      0.62697       0.66324       0.77179       1.00000       0.24335       0.16018       0.15767       0.16493
       5      0.13369       0.11570       0.12655       0.24335       1.00000       0.46914       0.46471       0.69049
       6     -0.00462      -0.02231      -0.02042       0.16018       0.46914       1.00000       0.84421       0.51010
       7     -0.00603      -0.02394      -0.02218       0.15767       0.46471       0.84421       1.00000       0.50086
       8      0.11918       0.10138       0.09666       0.16493       0.69049       0.51010       0.50086       1.00000
#  =========================================================================


#               EIGENVALUES AND EIGENVECTORS

# Number of Input Layers      Number of Principal Component Layers
#           8                          8
# PC Layer         1             2             3             4             5             6             7             8
#  -------------------------------------------------------------------------
# Eigenvalues
              2.294814e+07  3.624251e+06  3.263681e+06  1.138066e+06  4.935194e+05  1.388485e+05  3.183872e+04  5.731267e+03
# Eigenvectors
# Input Layer
       1      2.649690e-02  1.268439e-01  3.713418e-01 -6.170639e-02  3.940081e-01 -3.330263e-04  6.034159e-01 -5.675851e-01
       2      2.607099e-02  1.470990e-01  4.251065e-01 -6.798578e-02  3.816503e-01 -1.217802e-03  1.860589e-01  7.823479e-01
       3      3.350756e-02  1.965655e-01  5.322343e-01 -4.999655e-02  2.094850e-01 -2.691397e-04 -7.520485e-01 -2.549613e-01
       4      6.745980e-02  2.213169e-01  5.148910e-01  2.307573e-01 -7.698821e-01  2.116304e-03  1.860479e-01  2.774081e-02
       5      8.319730e-01  4.884801e-01 -2.528593e-01 -6.882255e-02  2.270619e-02 -5.795812e-04 -3.880475e-03  1.691509e-03
       6      1.078160e-01 -1.012753e-01 -6.505070e-03  6.716516e-01  1.697578e-01 -7.054163e-01 -2.301497e-02 -1.086864e-03
       7      1.054659e-01 -9.711466e-02 -8.300154e-03  6.683792e-01  1.724545e-01  7.087814e-01 -2.314642e-02 -1.828215e-04
       8      5.272744e-01 -7.850813e-01  2.625923e-01 -1.823178e-01 -5.851765e-02  3.208780e-03 -7.556993e-05  8.264583e-05
#  =========================================================================


#               PERCENT AND ACCUMULATIVE EIGENVALUES

# PC Layer   EigenValue    Percent of EigenValues   Accumulative of EigenValues
       1  2.294814e+07          72.5195                    72.5195
       2  3.624251e+06          11.4532                    83.9727
       3  3.263681e+06          10.3137                    94.2864
       4  1.138066e+06           3.5965                    97.8829
       5  4.935194e+05           1.5596                    99.4425
       6  1.388485e+05           0.4388                    99.8813
       7  3.183872e+04           0.1006                    99.9819
       8  5.731267e+03           0.0181                   100.0000
#  =========================================================================
```

Appendix – F

Appendix F 1-1: RADAR Characteristics and Decomposition

1.1 RADAR Characteristics

The SAR geometry characteristics mainly include incidence angle, slant range, swath width, and near & far ranges. The main SAR reflectivity is measured in parameters such as sigma-naught (σ^o), beta-naught (β^o), and gamma-naught (γ^o). Among those while calibrating, the output can be saved in a complex format if partial and fully polarised data is used. Moreover, RADAR backscatter sigma-naught (σ_o) is most commonly used when calibrating, it is the ratio of the backscatter per unit area on the ground as shown in Figure 1. Conversion into decibels (dB) using Equation 1 is also undertaken to generate more normally distributed data.

$$\sigma^o[dB] = 10\log_{10}(DN)^2 + CF \quad \textit{(Attarchi 2020)} \qquad \textbf{Equation: 1}$$

σ^o is RADAR backscatter coefficient, DN is a digital number and CF is the calibration factor (CF = -83 dB). A number of studies suggest that RADAR interaction with canopy is very much dependent of frequency, polarisation, incidence angle and look direction.
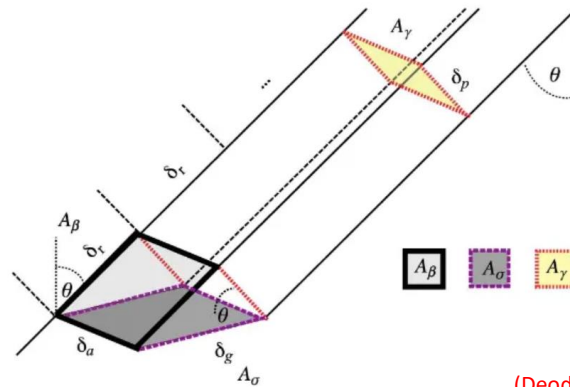
(Deodoro et al. 2024)

Figure 1: RADAR backscatter coefficients $(\sigma^o, \beta^o, \gamma^o)$

In general, mangrove AGB estimation are calculated using RADAR backscatter, RVI, PCA analysis and GLCM matrix of backscatter. However, in some scenarios decomposition is also effective by calculating covariance (C3) and coherence matrix (T3).

1.2 SAR Polarimetry

SAR polarisation considers the study of polarisation state of electromagnetic energy. The polarisation of SAR might be single polarised (H or V), dual polarized (H and V), and fully polarised (HH, HV, VH, VV). The polarisations states of electromagnetic waves could be linear, circular and elliptical. Interestingly, in this research ALOS-2 PALSAR imagery is acquired in full-polarised mode to understand the polarisation sates of the electromagnetic wave. SAR polarimetric concepts can be

explained by polarisation vectors. The polarisation state of EM wave can be best described using Jones and Stokes vector. *Jones vector* is used to express full polarised wave and can be written in a matrix form as described in Equation 2.

$$E_{HV} = \begin{bmatrix} E_H \\ E_V \end{bmatrix} = \begin{bmatrix} |E_H|\, e^{j\phi_H} \\ |E_V|\, e^{j\phi_V} \end{bmatrix}$$

(Yamaguchi 2020)

Equation: Error! No text of specified style in document.

Here E is the amplitude and ϕ is the phase information of the electric field. Next import parameters to represent partially or fully polarisation state of electromagnetic wave is called *Stokes vector*. There are four parameters in *Stokes vector* and mainly represents wave intensity and geometry as described in Equation 3.

$$S = \begin{bmatrix} S_0 \\ S_1 \\ S_2 \\ S_3 \end{bmatrix} = \begin{bmatrix} |E_H|^2 + |E_V|^2 \\ |E_H|^2 - |E_V|^2 \\ 2|E_H||E_V|\cos\delta \\ 2|E_H||E_V|\sin\delta \end{bmatrix}$$

(Raney et al. 2012)

Equation: 3

Here $|E_H|$ and $|E_V|$ are amplitudes, and δ is the phase difference $\phi_V - \phi_H$ between H and V polarizations. Stoke parameters can also be described as mathematically as described in Equation: 4.

$$S_0^2 = S_1^2 + S_2^2 + S_3^2$$

(Richards 2009)

Equation: 4

1.3 Polarimetric Decomposition

It is one of the important parameters to study object properties. In general, scattering might be of two types; coherent and incoherent. In coherent decomposition, the scattering matrix is used to describe the polarisation behaviour of the object. The mathematical form of scattering matrix can be defined as.

$$S = \begin{bmatrix} S_{HH} & S_{HV} \\ S_{VH} & S_{VV} \end{bmatrix}$$

(Yonezawa et al. 2012)

Equation: 5

It is known that, scattering matrix cannot explain fully the very incoherent nature of scatter, so in this regard the covariance (C3) and the coherent matrix (T3) can be used to study object behaviour. Therefore, scattering vector for covariance matrix can be written as below in Equation: 6.

$$k_{3L} = \begin{bmatrix} S_{HH} \\ \sqrt{2}\, S_{HV} \\ S_{VV} \end{bmatrix}$$

(Chen et al. 2020)

(Mullissa et al. 2017)

Equation: 6

Mainly covariance matrix can be obtained by multiplying k_{3L} by its conjugate. The final outcome might be written as Equation 7.

Appendix – F

$$C_3 = \begin{bmatrix} C_{11} & C_{12} & C_{13} \\ C_{21} & C_{22} & C_{23} \\ C_{31} & C_{32} & C_{33} \end{bmatrix}$$

$$= \begin{bmatrix} |S_{HH}|^2 & \sqrt{2}S_{HH}S_{HV}^* & S_{HH}S_{VV}^* \\ \sqrt{2}S_{HV}S_{HH}^* & 2|S_{HV}|^2 & \sqrt{2}S_{HV}S_{VV}^* \\ S_{VV}S_{HH}^* & \sqrt{2}S_{VV}S_{HV}^* & |S_{VV}|^2 \end{bmatrix}$$

(Srivastava et al. 2022)

(Richards 2009)

Equation: 7

Moreover, the coherent matrix (T3) can be defined with the help of Pauli scattering vector as given in Equation 8

$$k_{3P} = 1/\sqrt{2} \begin{bmatrix} S_{HH} + S_{VV} \\ S_{HH} - S_{VV} \\ 2S_{HV} \end{bmatrix}$$

(Fang et al. 2024)

Equation: 8

With the help of the vector in Equation: 8, the final outcome could be derived from coherency matrix as described in Equation: 9.

$$T_3 = \begin{bmatrix} T_{11} & T_{12} & T_{13} \\ T_{21} & T_{22} & T_{23} \\ T_{31} & T_{32} & T_{33} \end{bmatrix} =$$

(Srivastava et al. 2022)

Equation: 9

$$\begin{bmatrix} |S_{HH} + S_{VV}|^2 & (S_{HH} + S_{VV})(S_{HH} - S_{VV}) & 2((S_{HH} + S_{VV})S_{XX}^* \\ (S_{HH} + S_{VV})(S_{HH} - S_{VV}) & |S_{HH} - S_{VV}|^2 & 2((S_{HH} - S_{VV})S_{XX}^* \\ 2(S_{HH} + S_{VV})S_{XX}^* & 2(S_{HH} - S_{VV})S_{XX} & 4|S_{XX}|^2 \end{bmatrix}$$

Interestingly, backscatter in current study area seems to be incoherent so covariance (C3) and coherent(T3) decompositions are in focused. There are many incoherent decomposition are available; models based and eigenvectors (S.R Cloude, WA Holm, E pottier). In this study, model based Freeman-Durden and eigen-based (H-α) decomposition will be used for analysis.

Appendix F 1-2: Principal Component Analysis – PCA

Principal Component Analysis - PCA

Principal component analysis - PCA is a very well known method to convert larger number of variables (bands) into smaller components without losing their details (Chuvieco 2016). This technique will be used to study textural variability for optical and RADAR (Pham et al. 2018) and fusion imageries. Researchers believe that, it is very useful technique to remove similar radiance in the bands and it decomposes the image into eigenvectors associated with eigenvalues. As a result, the most suitable axis can obtained for analysis. Moreover, it is very helpful to identify the relationship between two spectral bands and dimensionality reduction of the data. Normally, PC-1 considered being the best informative band in terms of keeping maximum information. Mathematically, PC-1 can be written using Equation 10.

$$PC_1 = a_{1i}DL_i + a_{1k}DL_k$$ (Chuvieco 2016)   **Equation: 10**

Where, PC_1 is first principal component, a_{1i} is the coefficient of band *i* and *k*.

Appendix F 1-3: Gray Level Co-occurrence Matrix - GLCM

GLCM is most common method to explore the image dimensionality based on texture. Texture is the pattern of variation and transformed images are very helpful to identify spatial distribution of gray levels for better classification. People have divided into various different categories. Haralick, (1973) has divided the processes into groups. Contrast group (contrast, dissimilarity, homogeneity), orderliness group (angular second moment - ASM, maximum probability-MAX, entropy), statistics group (mean, variance, correlation) and energy. This study will use this technique to identify textural variations in ALOS-1 PALSAR, ALOS-2 PALSAR and Sentinel-1 data. The GLCM based explanatory variables considered to be helpful to calculate AGB. But this approach will be restricted to RADAR to identify best regression model.